NASA Contractor Report 2933

The Practical Application of a Finite Difference Method for Analyzing Transonic Flow Over Oscillating Airfoils and Wings

Warren H. Weatherill, James D. Sebastian,
and F. Edward Ehlers

CONTRACT NAS1-14204
FEBRUARY 1978

NASA

NASA Contractor Report 2933

The Practical Application of a Finite Difference Method for Analyzing Transonic Flow Over Oscillating Airfoils and Wings

Warren H. Weatherill, James D. Sebastian, and F. Edward Ehlers

Boeing Commercial Airplane Company
Seattle, Washington

Prepared for
Langley Research Center
under Contract NAS1-14204

NASA
National Aeronautics
and Space Administration

Scientific and Technical Information Office

1978

6. Three-dimensional results are presented for a clipped delta wing with leading-edge sweep of 50.5° with a circular-arc airfoil section and for an aspect ratio 5 rectangular wing with a NACA 64A006 airfoil section.

7. A conservative shock point operator was derived for use at a mesh point where the steady flow is supersonic while the flow at the next point downstream is subsonic.

2.0 INTRODUCTION

The purpose of the work described in this report was to develop a means for calculating air forces for use in flutter analyses of three-dimensional lifting surfaces in the transonic flight regime. Flutter is not only a significant problem at transonic speeds, but it has also proved difficult to predict analytically. These difficulties result not only from the mathematical complexities of the equations but also from computer resources required by the repetitive nature of flutter analyses performed during vehicle design.

Various methods are currently under study for predicting unsteady transonic air forces, ranging from the relatively expensive finite difference models including time integrations to economical approximate procedures based on linear theory. The procedure of this report is intended to be intermediate in terms of computer machine resource usage and is based on a finite difference method developed by Ehlers in reference 1. The assumption of small perturbations from a uniform stream near the speed of sound retains the necessary complexity for describing flows with local supersonic regions. The application of the perturbation velocity potential restricts the solution to weak shocks which, for thin wings of reasonably good design, is not too limiting an assumption. When the flow is steady, the resulting nonlinear differential equation reduces to the well-known transonic small perturbation equation studied by Murman, Cole, and Krupp (refs. 2, 3, and 4). The unsteady differential equation is simplified by considering the flow to consist of the sum of two separate potentials representing the steady and unsteady effects. The assumption of small amplitudes of harmonic oscillation leads to a linear differential equation for the unsteady potential with variable coefficients depending on the steady flow. The resulting air forces are thus superposable and may be directly used in conventional flutter analysis formulations.

The effect of thickness is included in the steady flow analysis. The unsteady analysis is carried out for a wing of vanishing thickness but submerged in a velocity potential distribution resulting from the steady analysis. As formulated, the shock is assumed to be fixed by the steady flow. It is noted that shock motion could be included in a linear fashion by introducing the perturbations of the unsteady motion into the Rankine-Hugoniot relations.

Generally, the results of applying this procedure, as reported in references 5 through 9, have been encouraging. First, correlation of finite difference solutions for flat plate configurations with corresponding results from linear theory has been good for both two- and three-dimensional configurations. For mixed flow, where the solutions for a NACA 64A006 airfoil were compared with experimental data from Tijdeman and Schippers (ref. 10), the pattern of the pressure distribution closely followed that observed experimentally; however, the analytical pressure levels were generally higher than the measured levels. The reason for the discrepancy between theory and experiment is not known, but the discrepancy may be due to boundary layer or separation effects, or both, or to unknown problems associated with the theory or with the pressure measurements. Thus, the correlation studies for the two-dimensional case have been inconclusive because of the lack of knowledge of viscous effects and, for the three-dimensional case, because of a lack of experimental pressure data.

A significant cause for concern in the practical application of this procedure has been stability problems with the relaxation procedures used to solve the sets of finite difference equations. These stability problems – which are a function of reduced frequency, Mach number, and the size of the finite difference region – severely limit the use of this method in flow regimes of most interest. Solution stability is thus a major topic of this report.

Section 6.0 is devoted to a discussion of the accuracy of solutions from the finite difference model in comparison with subsonic solutions for the flat plate. In addition, results are presented for a low-aspect-ratio delta wing and a moderate-aspect-ratio rectangular wing.

A parallel study using finite difference methods on the unsteady transonic flow problem has been conducted by Traci, Albano, and Farr (refs. 7, 8, and 9). The resulting procedure concentrates in a consistent manner on the low-frequency regime. Their derived equations do not include the cross product term consisting of the derivative of the unsteady velocity potential φ_1 with respect to time and of the second derivative of the steady velocity potential φ_0 with respect to the flow-wise coordinate. In most of their applications, the second derivative with respect to time is left out. However, the formulation of the finite difference equations, the handling of the boundary conditions, and the use of a column line relaxation solution procedure appear very similar to the procedure used here.

3.0 SYMBOLS AND ABBREVIATIONS

a	Streamwise dimension of mesh region, also value of x at left hand side of one-dimensional interval
b	Root semichord of wing, also vertical dimension of mesh region, also value of x at right hand side of one-dimensional interval.
E	Maximum error quantity
f(x,y,t)	Instantaneous wing shape defined by $z_0 = \delta f(x,y,t)$
f(y)	Function defining wing trailing edge
f_0	Undisturbed wing or airfoil shape
f_1	Unsteady contribution to wing or airfoil shape
h	Distance between mesh points in one-dimensional problem
i, j,k	x,y,z subscripts for points in the mesh
i	$\sqrt{-1}$
K	Transonic parameter, $(1-M^2)/(M^2\epsilon)$
l_x, l_y,	Dimensions of element used in residual discussion
M	Freestream Mach number
ORF	Overrelaxation factor
q	$\omega^2/\epsilon - i\omega(\gamma-1)\varphi_{0xx}$
R	Wall porosity parameter, also vector length used in Appendix B
U_0	Freestream velocity
x_0, y_0, z_0	Physical coordinates, made dimensionless with the root semichord.
x,y,z	Scaled coordinates $(x_0, \mu y_0, \mu z_0)$ for the three-dimensional problem; the scaled coordinates for the two-dimensional problem are x and y, with x again being the direction of fluid flow.
x'_1, y'_1, z'_1	Variables of integration
x_l, x_{te}	Coordinates of leading and trailing edges

y_t	Coordinate of wing tip
α	Angle-of-attack
β	$\sqrt{1-M^2}$
γ	Ratio of specific heats for air
ΔC_p	Jump in pressure coefficient
$\Delta\phi_1$	Jump in ϕ_1 at plane of wing or vortex wake
$\Delta\varphi_{1_{te}}$	Jump in φ_1 , at wing trailing edge
δ	Thickness ratio or measure of camber and angle of attack
ϵ	$(\delta/M)^{2/3}$
λ_1	$\omega M/(1-M^2)$
μ	Scale factor on y_0 and z_0, $\mu = \delta^{1/3}M^{2/3}$
ξ,ζ	Dummy scaled coordinates for two-dimensional problem
ζ	Air Density
ϕ	Unscaled perturbation velocity potential
φ_0	Steady scaled perturbation velocity potential
φ_1	Unsteady scaled perturbation velocity potential
φ_{1_W}	Wake integral defined in equation (B-1)
ω	Angular reduced frequency (semichord times frequency in radians per second divided by the freestream velocity, $\omega b/U$)

4.0 FORMULATION AND SOLUTION

A detailed mathematical derivation of the method for the solution of the unsteady velocity potential for the flow about a harmonically oscillating wing is presented in reference 1. The discussion here will be limited to a brief outline of the procedure for the two-dimensional flow.

The complete nonlinear differential equation was simplified by assuming the flow to be a small perturbation from a uniform stream near the speed of sound. The resulting equation for unsteady flow is

$$[K - (\gamma - 1)\,\varphi_t - (\gamma + 1)\,\varphi_x]\,\varphi_{xx} + \varphi_{yy} - (2\,\varphi_{xt} + \varphi_{tt})/\epsilon = 0 \tag{1}$$

where $K = (1 - M^2)/M^2\epsilon$, M is the freestream Mach number of velocity U_0 in the x-direction, x and y are made dimensionless to the semichord b of the airfoil and the time t to the ratio b/U_0. With the airfoil shape as a function of time defined by the relation

$$y_0 = \delta f(x,t)$$

the linearized boundary condition becomes

$$\varphi_y = f_x(x,t) + f_t(x,t) \tag{2}$$

The quantity δ is associated with properties of the airfoil (such as maximum thickness ratio, camber, or maximum angle of attack) and is assumed small. The coordinate y is scaled to the dimensionless physical coordinate y_0 according to

$$y = \delta^{1/3} M^{2/3} y_0$$

and ϵ is given in terms of δ by

$$\epsilon = (\delta/M)^{2/3}$$

The pressure coefficient is found from the relation

$$C_p = -2\epsilon\,(\varphi_x + \varphi_t)$$

The preceding differential equation is simplified by assuming harmonic motion and by assuming the velocity potential to be separable into a steady-state potential and a potential representing the unsteady effects. We write for a perturbation velocity potential

$$\varphi = \varphi_0\,(x,y) + \varphi_1\,(x,y)e^{i\omega t} \tag{3}$$

and for the body shape

$$y_0 = \delta f(x,t) = \delta\left[f_0(x) + f_1(x)e^{i\omega t}\right]$$

Since the steady-state terms must satisfy the boundary conditions and the differential equation in the absence of oscillations, we obtain

$$[K - (\gamma + 1)\varphi_{0_x}]\,\varphi_{0_{xx}} + \varphi_{0_{yy}} = 0 \tag{4}$$

with

$$\varphi_{0_y} = f_{0_x}(x), \quad y = 0, \quad -1 \leqslant x \leqslant 1 \tag{5}$$

On the assumption that the oscillations are small and products of φ_1 may be neglected, equations (1) and (2) with the aid of equations (4) and (5) yield

$$\left\{\left[K - (\gamma + 1)\varphi_{0_x}\right]\varphi_{1_x}\right\}_x + \varphi_{1_{yy}} - (2i\omega/\epsilon)\,\varphi_{1_x} + q\,\varphi_1 = 0 \tag{6}$$

where

$$q = \omega^2/\epsilon - i\omega(\gamma - 1)\varphi_{0_{xx}}$$

subject to the wing boundary conditions

$$\varphi_{1_y} = f_{1_x}(x) + i\omega f_1(x), \quad y = 0, \quad -1 \leqslant x \leqslant 1 \tag{7}$$

A computer program for solving the steady-state transonic flow about lifting airfoils based on equations (4) and (5) was developed by Krupp and Murman (refs. 3 and 4). The output of this program or a similar program can be used in computing the coefficients for the differential equation of the unsteady potential. The similarity of the unsteady differential equation to the steady-state equation suggests that the method of column relaxation used by Krupp for the nonlinear steady-state problem should be an effective way to solve equation (6) for the unsteady potential φ_1. Note that equation (6) is of mixed type; being elliptic or hyperbolic whenever equation (4) is elliptic or hyperbolic. Central differencing was used at all points for the y derivative and all subsonic or elliptic points for the x derivatives. Backward (or upstream) differences were used for the x derivatives at all hyperbolic points.

The boundary condition that the pressure be continuous across the wake from the trailing edge was found in terms of the jump in potential $\Delta\varphi_1$ to be

$$\Delta\varphi_1 = \Delta\varphi_{1_t} e^{-i\omega(x - x_{te})} \tag{9}$$

where $\Delta\varphi_{1te}$ is the jump in the potential at $x = x_{te}$ just downstream of the trailing edge and is determined to satisfy the Kutta condition that the jump in pressure vanish at the trailing edge. The quantity $\Delta\varphi_1$ is also used in the difference formulation for the derivative φ_{1yy} to satisfy continuity of normal flow across the trailing-edge wake.

For the set of difference equations to be determinate, the value of φ_1 or its derivative must be prescribed on the mesh boundary. Following Klunker (ref. 11), we found an asymptotic integral representation for the far-field φ_1 potential, and for the related pressure potential $\varphi_{1_x} + i\omega\varphi_1$. Because of the difficulty with convergence of the integral over the wake for the integral equation of the velocity potential, upstream and downstream boundary conditions for the mesh were given in terms of the pressure potential $\varphi_{1_x} + i\omega\varphi_1$, for which the wake integral can be integrated in closed form. The value of φ_1 was computed at one point on the upper boundary and at one point on the lower boundary; the points were conveniently chosen to facilitate rapid convergence of the wake integral. The values of φ_1 at other points on the upper and lower boundaries were found by numerically integrating the quantity $\varphi_{1_x} + i\omega\varphi_1$ with respect to x.

The numerical solution to the resulting large order set of difference equations may be obtained by using a relaxation procedure. The initial solutions were obtained by using a line relaxation procedure. Convergence is determined by monitoring ERROR, the maximum change in the velocity potential between iteration steps. ERROR is defined as the maximum value over all i and j of

$$\left[\frac{\varphi_{1_{ij}}^{(n)} - \varphi_{1_{ij}}^{(n-1)}}{r}\right]$$

where $\varphi_{1_{ij}}^{(n)}$ is the unsteady velocity potential for the nth iteration, $\varphi_{1_{ij}}^{(n-1)}$ corresponding potential for the preceding iteration, and r is the relaxation factor. The solution was considered converged when ERROR $\leq 10^{-5}$. In some cases, particularly for finer meshes and for the pitch mode, convergence was considered complete when ERROR $\leq 10^{-4}$.

5.0 RELAXATION SOLUTION STABILITY

As discussed in a preceding NASA report by the authors (ref. 5), significant stability problems were encountered with the relaxation procedures used to solve the finite difference equations. Generally, these procedures paralleled those successfully used for the steady-state problem. In essence, this meant sweeping through the mesh with a line relaxation procedure. When the line of points was parallel to the freestream, it was called row relaxation; when the line was perpendicular to the flow, it was called column relaxation.

The characteristics of the solution instability are as follows:

1. It occurs with the flow is purely subsonic as well as mixed with locally supersonic regions. Thus, the instability is not dependent on the presence or absence of transonic shock flow.

2. It appears to be a function of $\lambda_1 = \omega M/(1 - M^2)$ and the size of the finite difference area for the two-dimensional problem or volume for the three-dimensional problem. An analysis of the flat plate with a uniform mesh yields for the critical value of λ_1, the value of λ_1 above which the relaxation solution is unstable,

$$\lambda_{1_{critical}} = \pi \left[\frac{1}{a^2} + \frac{1}{Kb^2} \right]^{1/2} \tag{10}$$

   where a is the streamwise dimension of the mesh region, b is the height, and K is the transonic parameter.

3. For a given condition (say a fixed Mach number and finite difference point setup), as λ_1 was increased the rate of convergence decreased until the solution started to diverge. Thus, the actual value of λ_1 for which the solution first diverges is ill-defined, although it is generally in the neighborhood of the value given by equation (10).

Some insight into the causes of the instability may be obtained by considering the Helmholtz equation into which the difference equation for the oscillating flow over a flat plate may be transformed, namely,

$$\chi_{xx} + \chi_{yy} + \lambda_1{}^2 \chi = 0 \tag{11}$$

It is well known that solutions to the Helmholtz equation may not be unique for given types of boundary conditions on a closed region since eigenfunctions with real eigenvalues can occur; i.e., functions representing standing waves for which homogeneous boundary conditions occur on the boundary. For the rectangular mesh area of width b and length a, the first eigenvalue associated with solutions of the Helmholtz equation with Dirichlet boundary conditions is the critical value of λ_1 just

presented. In terms of the relaxation procedure, it was shown in reference 5 that solution of a relaxation problem of the form

$$[A(\lambda_1)]\{\varphi_1\} = \{R\} \tag{12}$$

converges only when $[A]$ is positive definite, and this holds for the unsteady problem when λ_1 is less than $\lambda_{1\text{critical}}$.

Integral equation solutions currently in use for the linearized subsonic unsteady solutions employ only the outgoing wave solution for the kernel function. Similarly the outgoing wave solution is used to define Klunker-type (ref. 11) boundary conditions on the outer boundary of the mesh region. Apparently the incoming wave solution is picked up during the numerical solution.

Investigations to remove or moderate the relaxation solution stability problem may take any of several paths. The approaches discussed here include (1) modifying the boundary conditions with the hope that the numerical solution would pick up only the outgoing wave solution, (2) using a coordinate transformation so that boundary conditions in the physical plane at infinity could be applied to the outer boundaries of a finite mesh region, (3) replacing the iterative relaxation solution with a full direct solution and thus solving for all the unknown velocity potentials at one time, and (4) using an overlapping subregion concept.

Approaches that have also been considered to some degree and have not proved successful include the following:

- Artificial manipulation of elements in $[A]$ in order to provide a better conditioned matrix. In particular, an attempt was made to shift the eigenvalues of $[A]$ by addition of a large diagonal matrix to $[A]$. (Such an addition must, of course, be compensated for by appropriate modification of the right-hand side of the system.) This modification did not improve the stability or convergence properties of the solution method. Subsequent theoretical investigations revealed that such a modification is essentially equivalent to doing underrelaxation on the original system.

- A sequential mesh refinement system based on the procedures discussed by Brandt in reference 12.

- A mathematical technique for making $[A]$ positive definite for values of λ_1 above $\lambda_{1\text{critical}}$ by premultiplication by the conjugate transpose of $[A]$. This procedure and some results are presented by Hafez, Rizk, and Murman in reference 13. Our experience has been essentially the same as they describe; (i.e., that the convergence rate in the relaxation solution of the $[A * A]$ system is very slow and that a small value for the maximum difference between iterations does not imply that the last iteration is correspondingly close to the true solution.

5.1 VARIATIONS IN OUTER BOUNDARY CONDITIONS

The Klunker-type boundary conditions defined φ_1 on the upper and lower boundaries and set $\varphi_{1x} + i\omega\varphi_1$ on the upstream and downstream boundaries of the finite difference region. Since these boundary conditions apparently did not effectively sort out the incoming waves from the outgoing waves, alternative conditions were explored. These included using an outgoing radiation-type condition on all four boundaries and also a porous wall boundary condition on the upper and lower boundaries. The mathematical forms for these boundary conditions are summarized in table 1. The porous wall conditions could be varied to form either a "free jet" by making the porosity parameter, R, very large or a "solid wall" condition by making R small. In practice, the parameter is usually fixed by some empirical method for specific wind tunnel conditions but, for the current work, the interest is on how the stability of the relaxation solution may be dependent on its value.

Table 1.–Equations for Boundary Conditions

Boundary conditions	Boundary	Equation
1. Outgoing wave	Upstream	$\phi_{1x} - i\omega \frac{M}{1-M}\phi_1 = 0$
	Downstream	$\phi_{1x} + i\omega \frac{M}{1+M}\phi_1 = 0$
	Upper	$\phi_{1y} + \frac{i\omega\sqrt{K}}{1-M^2}\phi_1 = 0$
	Lower	$\phi_{1y} - \frac{i\omega\sqrt{K}}{1-M^2}\phi_1 = 0$
2. Porous wall	Upper	$\phi_{1x} + i\omega\phi_1 + \frac{1}{R}\phi_{1y} = 0$
	Lower	$\phi_{1x} + i\omega\phi_1 - \frac{1}{R}\phi_{1y} = 0$

The pilot program was modified so that all six combinations of outer boundary conditions shown in table 2 could be run; that is, either of the two conditions on the upstream and downstream boundaries could be run with any one of the three boundary conditions specified for the upper and lower boundaries. The free-jet and solid wall boundary conditions also were programmed explicitly and thus could be applied without the need for fixing a value for R. The test example consisted of a two-dimensional airfoil of vanishing thickness oscillating in harmonic pitch at a Mach number of 0.9. For this case and for the mesh dimensions that are used, the reduced frequency above which relaxation solutions are expected to be unstable according to equation (10) is about 0.1. The examples were run for a very coarse mesh (17 x 10), and the overrelaxation factor (ORF) was varied to make sure the solution instabilities were not due to too large an ORF.

Table 2.—Types of Boundary Conditions

Upstream and downstream boundaries	Upper and lower boundaries
1. Klunker	1. Klunker
2. Outgoing wave	2. Porous wall Free jet (large R) Intermediate Solid wall (small R)
	3. Outgoing wave

In summary, the results of the calculations showed that the alternate boundary conditions used did not significantly improve the convergence of the solution. In some cases, a slight increase in the value of reduced frequency was observed for which convergent solutions could be obtained. No combination of boundary conditions would provide solution convergence above a reduced frequency of 0.18. Since the exact values of ω at which a relaxation solution stops converging and starts diverging cannot be exactly determined anyway, the results of this investigation were not considered promising.

5.2 COORDINATE TRANSFORMATION

A second concept explored in hopes of removing the relaxation solution stability problem was a coordinate transformation that permits the boundary conditions at infinity to be used on the boundaries of the finite difference region; that is, the physical region to infinity is mapped into the limited area of the finite difference mesh in the calculation plane. The particular form of transformation that was used is that suggested by Carlson (ref. 14) which, as he points out, allows for a physically realistic behavior of the solution at infinity. The physical plane is divided into three regions by perpendicular lines through the leading and trailing edges of the airfoil. (See fig.1.) The physical plane coordinates (x,y) are related to the calculation plane coordinates (ξ,η) by the following relations:

In region I where $\xi \leq -1$

$$x = -1 + \tan\left[\frac{\pi}{2}(\xi + 1)\right] + \tan\left[\frac{\pi}{2}(\xi + 1)^3\right]$$

In region II, where $-1 < \xi < 1$

$$x = \xi \left\{\left(\frac{6 - \pi}{4}\right) + \left(\frac{\pi - 2}{4}\right)\xi^2\right\}$$

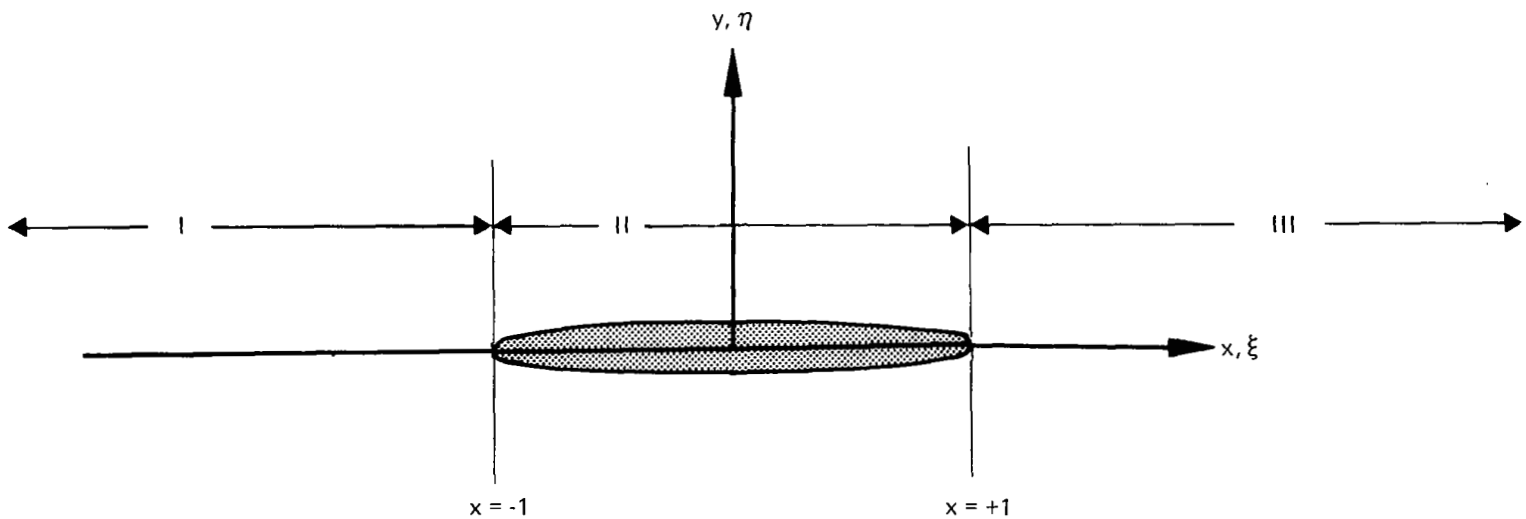

Figure 1.—Subdivision of Flow Field for Coordinate Transformation

In region III, where $1 \leq \xi$

$$x = 1 + \tan\left[\frac{\pi}{2}(\xi - 1)\right] + \tan\left[\frac{\pi}{2}(\xi - 1)^3\right]$$

and

$$y = \tan\frac{\pi}{2}\eta$$

Two different boundary conditions were used. The first consisted simply of making $\varphi = 0$ on all four boundaries; the second, of using the outgoing wave conditions discussed in the preceding section. Here, the outgoing wave condition was applied at the midpoint between the boundary and the point adjacent to the boundary.

These changes did not solve the relaxation solution stability problem. For a given Mach number, for example, relatively little (if any) change was noted in values of reduced frequency at which the solution became unstable.

It is of interest to note that the combination of the coordinate transformation and the outgoing wave boundary condition provided results for the flat plate which very closely matched corresponding data from the NASA subsonic air force program (refs. 15 and 16). A comparison of results from using outgoing wave conditions together with the coordinate transformation is shown in figure 2. It should be noted that the former results are for a 42 x 30 mesh while the latter results are for a significantly coarser 28 x 20 mesh.

5.3 COMPLETE DIRECT SOLUTION

A "semidirect" solution procedure was examined by the authors in reference 5. The form of the equation solved at that time was

$$[A(\lambda_1)]\left\{\varphi_1^{(n)}\right\} = \left\{R\left(\varphi_1^{(n-1)}\right)\right\}$$

where $\{\varphi_1^{(n)}\}$ contained an element for each interior mesh point. In other words, there was still an iteration required to update the vector $\{R(\varphi_1^{(n-1)})\}$ on the right-hand side. Although very efficient for the small meshes for which it was used (i.e., permitted by the in-core solution capability), it was subject to the same type of solution instability as the relaxation solutions. However, it is possible to rewrite the equation so that all unknowns are on the left-hand side and the solution may be calculated without iteration.Consider, for example, the two-dimensional problem for purely subsonic flow. The mesh is set up to have IMAX points in x-direction and KMAX in the cross-flow direction. The points are sequenced by column, upstream to downstream. The unknowns consist of the φ_1's interior to the outer boundaries. Thus, the indice N of the point I,K is

$$N = (KMAX-2) * (I-2) + K$$

for $2 \leq I \leq IMAX-1$ and $2 \leq K \leq KMAX-1$

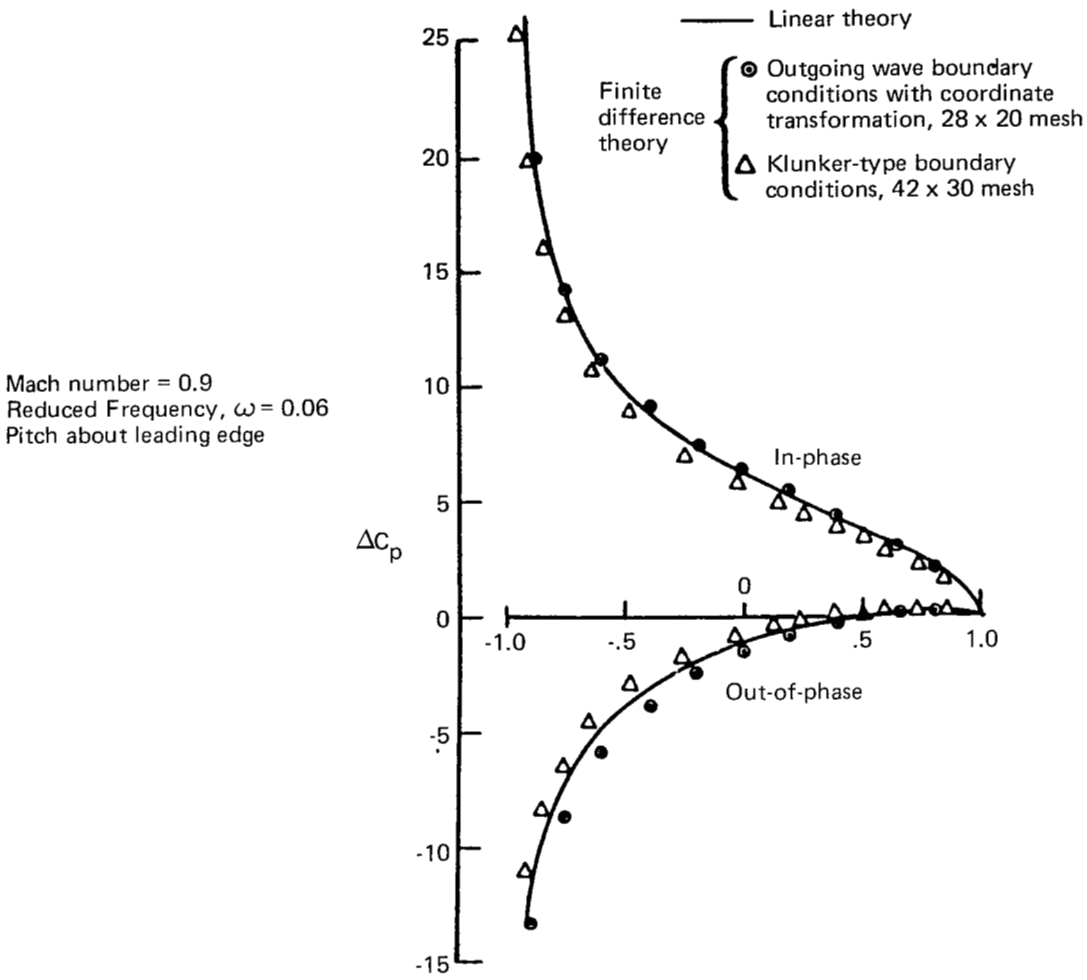

Figure 2.—Jump in Pressure Coefficient Across a Flat Plate Oscillating in Pitch, M = 0.9, ω = 0.06

The general form of the equation following eq. (24) of reference 1 (with all terms moved to the left-hand side) for points adjacent to the boundaries is of the form

$$D\varphi_{i-1k} + A\varphi_{ik-1} + B\varphi_{ik} + C\varphi_{ik-1} + E\varphi_{i+1k} = 0$$

With the sequencing as indicated above, the five terms in the coefficient matrix are in the following column locations:

n_D = KMAX* (I-3) + K
n_A = KMAX* (I-2) + K - 1
n_B = KMAX* (I-2) + K
n_C = KMAX* (I-2) + K + 1
n_E = KMAX* (I-1) + K

The bandwidth of the matrix is equal to $n_E - n_D + 1$ or $2^*(JMAX-2) + 1$. The boundaries present special problems. For example, the φ_1's adjacent to the wake, in addition to the usual dependency, are also functions of eight values of φ_1 at mesh points in the vicinity of the wing trailing edge (see eq. (41), (42), (85), and (86) of ref. 1). This significantly increases the bandwidth of the coefficient matrix. The φ_1's for points on the outer boundaries are, using Klunker-type boundary conditions, functions of the φ_1's at all other interior points in the mesh if the volume integrals are retained (see eq (110) and (114) of ref. 1). If the volume integrals are not retained (and this is the usual procedure), the boundary φ_1's remain functions of the $\Delta\varphi_1$'s across the wing and wake. Use of the outgoing wave boundary condition limits the dependency of the φ_1 for any point on the outer boundary to the immediate vicinity of that point. The bandwidth of the coefficient matrix is thus determined by the number of points in the wake. This complete or full direct procedure should provide answers over the full range of values except for the specific values of λ_1 for which the matrix $[A(\lambda_1)]$ is singular.

This procedure was first tested with a one-dimensional problem. There was no difficulty in obtaining solutions near the singular points. Accuracy, however, as measured against the analytic answers, did present difficulties, which are discussed in detail in section 5.

The full direct solution was also investigated for the two-dimensional problems. One formulation included the coordinate transformation and the outgoing wave boundary conditions discussed previously. Use of the latter significantly reduced the bandwidth of the $[A]$ matrix over what it would have been had Klunker-type outer boundary conditions been used, thus increasing the number of mesh points that could be handled by the in-core solution routines.

The resulting program was used on the sample problem of the airfoil of vanishing thickness oscillating in pitch. As with the one-dimensional program, no trouble was encountered in obtaining solutions at frequencies well above values that had proved critical for the relaxation solution. However, once the neighborhood of the critical value had been reached or exceeded, very poor correlation with corresponding solutions from the NASA subsonic unsteady flow program was obtained; that is, as the value λ_1 was increased from subcritical values to supercritical values, correlation with the NASA program went from very good to very poor. The characteristics of this lack of correlation are discussed in detail in section 6.

The original direct solution package did not contain a pivoting capability. Since concern was expressed about numerical accuracy of the solution in the neighborhood of the matrix singularities, a solution routine including partial pivoting with equilibration was inserted in the program. Although it could be determined that pivoting was used during the solution, the results remained exactly the same to the number of significant digits retained.

In summary, the full direct solution provides solutions at values of λ_1 above the critical value. The solutions do not correlate well with corresponding solutions from the NASA subsonic unsteady flow program and are thus not considered reliable. Although these solutions have been obtained using routines that include partial pivoting, the lack of correlation does not appear to be due to numerical problems inverting the matrices. The

problem may be due to the restriction to a relatively coarse grid because of a limitation of the in-core solution routine and/or to the type of boundary conditions. This seems to be borne out by the results from the study of the one-dimensional problem for which an error analysis is easy to obtain. This is discussed in detail in section 6.

5.4 OVERLAPPING REGIONS

As noted in the general description of the relaxation solution stability problem at the beginning of this section, the critical value of λ_1 is inversely proportional to the size of the finite difference region over which the solution is being calculated. This fact suggested the possibility of solving a sequence of small overlapping regions. The critical value of λ_1 for each subregion would be large, and perhaps continuity between subregions could be achieved by iteration. In a sense, the basic line relaxation procedure (whether accomplished by rows or columns) is the extreme limit of this concept with each column or row acting as a separate subregion. Experience has already shown us that this does not work.

However, some examples have been run using column relaxation with the finite difference solution region divided into two and three subregions vertically and with several variations in the amount of overlapping of the subregions. All results have been discouraging and there appears to be little point in extending this investigation further. A typical example using three subregions will be discussed next.

This example is for a flat plate (no mixed flow) and a relatively coarse mesh (17 x 10), but it should provide a good indication of how the concept of overlapping regions will work. The solution region was divided into three subregions in the streamwise direction. The location of the mesh points in the x-direction and the corresponding indices are shown in figure 3a. Figure 3b presents a sequence of convergence histories with the range of x-indices over which the column relaxation solutions were performed indicated below each pass. First, the solution for the complete region was calculated to check solution stability. As shown in figure 3b, with an ORF of 1.0, the solution at first converges slowly but after some 90 iterations has started to diverge. Using an ORF of 1.7, the solution is quite unstable and shows a general divergence trend. Included in the same figure are the convergence histories for the subregions. The calculation is started off by converging the middle section, which converges very rapidly. an ORF of 1.7 was used for this and all succeeding calculations. Then, as shown, the other sections were converged in succession. The φ_1 distribution was saved after each subregion solution and used as a starting point for the next solution. The overall convergence of the system, as noted from the starting error for each subregion solution, is marginal at best and would require many more solution sequences to determine whether the overall trend is convergent or divergent.

Finally, the pressure plots for three different stops along the solution path are shown in figure 3c. These distributions do not appear to be converging either. This example is not considered to be completely conclusive as to the worth of the overlapping subregions concept. It is typical of what we have experienced with other similar examples. We have found no evidence that this concept would provide a practical means to avoid problems arising from relaxation solution instabilities.

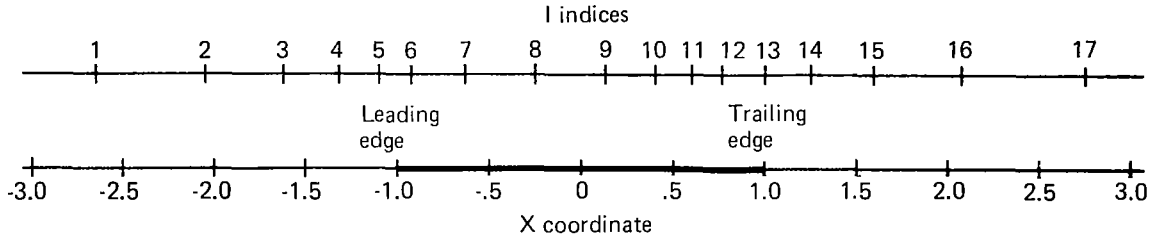

a. Distributions of Finite Difference Points, Flow Direction

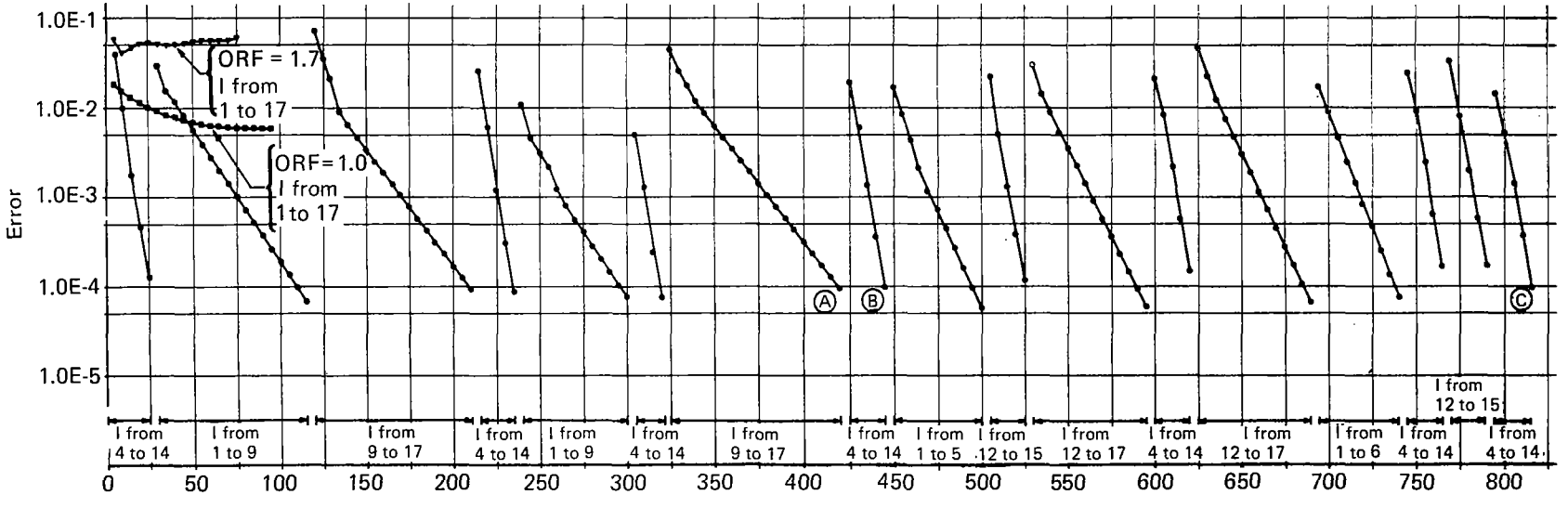

b. Error Versus Iteration History

Figure 3.—Example for Overlapping Regions Concept

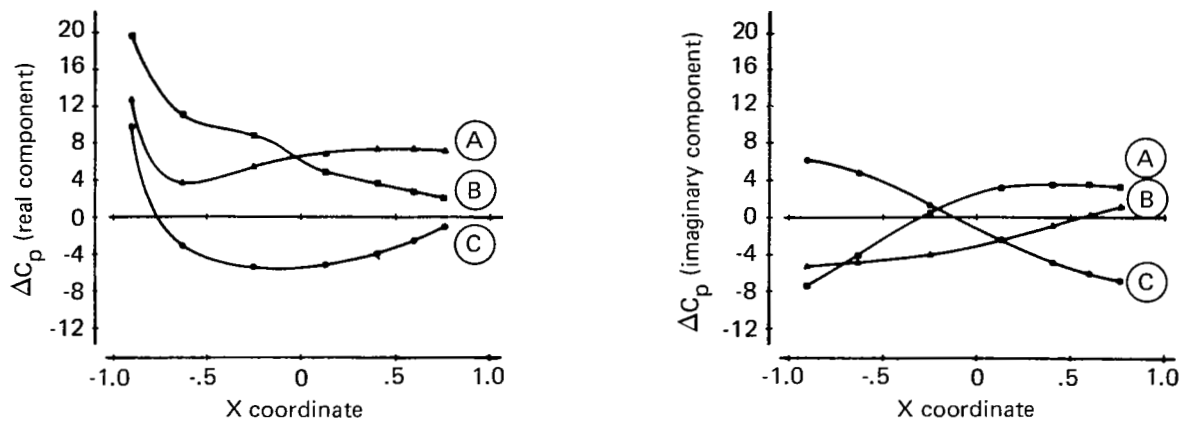

c. Variation in Pressure Distributions During Iterations

Figure 3.—(Concluded)

6.0 NUMERICAL ACCURACY FOR LARGER VALUES OF λ_1

The accuracy of the finite difference procedure of this report may be discussed in several different contexts. Previous reports (by the authors in refs. 1, 5, and 6 and Traci et al., in refs. 7, 8, and 9) have included numerical examples, the results of which are compared either with the experimental data of Tijdeman and Schippers (ref. 10) or with other analytical data. These analytical data may be for strictly subsonic flow (flow at high Mach number over a flat plate) or for more detailed transonic calculations including full shock effects such as those by Magnus and Yoshihara (ref. 17). The discussion here concentrates on the relationship between the critical value of λ_1 (critical in terms of relaxation solution stability) and the accuracy of the finite difference solutions relative to more exact linear solutions. The examples to be discussed do not include shock effects.

6.1 THE ONE-DIMENSIONAL PROBLEM

In order to gain insight into the unsteady transonic problem as formulated in this report, a one-dimensional version of the flat plate problem was investigated. The one-dimensional analog of the two-dimensional equation (6) for a flat plate may be obtained by dropping the $\varphi_{1_{yy}}$ term. Dividing the resulting equation by K, we have

$$\varphi_{1_{xx}} - 2i\lambda_1 M \varphi_{1_x} + \lambda_1{}^2 (1 - M^2) \varphi_1 = 0 \tag{13}$$

where $\lambda_1 = \omega M/(1 - M^2)$.

The exact general solution to equation (13) is

$$\varphi_1(x) = C_1 e^{i\lambda_1 (1+M)x} + C_2 e^{-i\lambda_1 (1-M)x} \tag{14}$$

where C_1 and C_2 may be determined once the boundary conditions (end conditions) are specified. The derivation of equations (13) and (14) along with a detailed discussion of the exact general solution is presented in appendix A. An approximate solution over an interval [a,b] may also be found by transforming equation (13) to a finite difference equation with the solution being obtained by either a full direct solution (similar to that discussed in sec. 5.3) or by a point relaxation procedure.

The interest here is in comparing answers obtained from the finite difference solution with corresponding answers from the exact solution. For this, the maximum error quantity E for a given reduced frequency ω_K, is defined as

$$E(\omega_K) = \max_{I=1,\,IMAX} \left| \varphi_{1_{I_{exact}}} - \varphi_{1_{I_{finite\ difference}}} \right| \tag{15}$$

The investigation is aimed at determining the effect of the kind of boundary conditions used on $E(\omega_K)$. First, it is clear from the exact solution that the solution for a given reduced frequency ω or λ_1 is made up of components with two substantially different wavelengths. For a given finite difference mesh (a given number of mesh points and specified mesh spacing), it would be expected that the short wavelength component would be less accurately represented than the long wavelength component; that is, a solution made up predominately of the short wavelength component would be less accurately determined using a finite difference calculation than a solution made up predominately of the long wavelength component. This has indeed proved to be the case as shown by examples presented in figure 4. Here two combinations of Dirichlet and Cauchy boundary conditions were used to obtain solutions. The first was set up so that the solution would consist solely of the short wavelength component and is denoted by the Δ-symbols in figure 4; and the second, set up so that the solution would consist solely of the long wavelength component, is denoted by the O symbols. The error level for the long wavelength component is significantly lower than that for the short wavelength component.

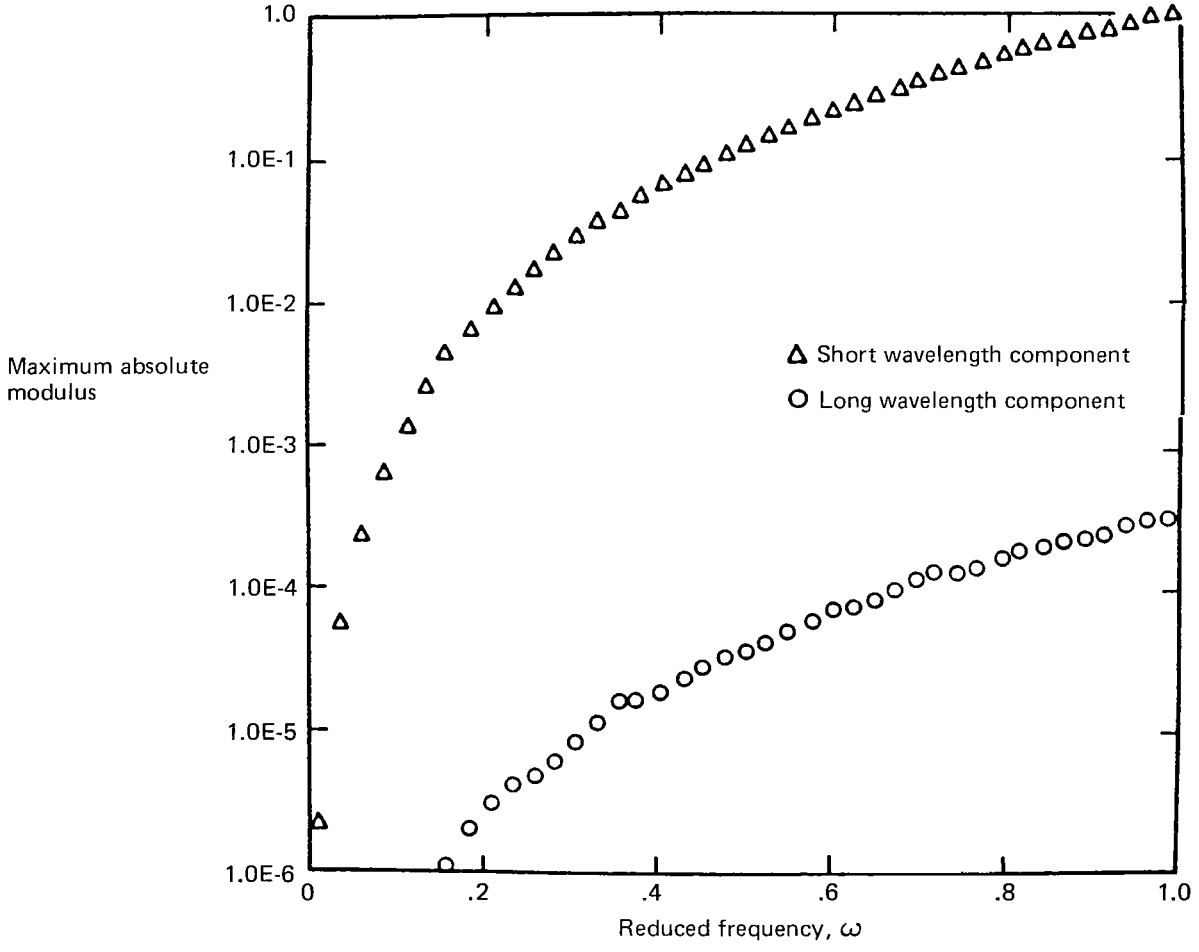

Figure 4.—Comparison of Error Curve for Long and Short Wavelength Solutions

Second, it is of interest to know how the error varies with frequency. An analysis of a similar equation was made by Fischer and Usmani in reference 18. The equation studied was of the form

$$\psi_{xx} + \lambda_1{}^2 \psi = 0 \tag{16}$$

and is simply related to our one-dimensional φ_1 equation by the transformation

$$\varphi_1 = \psi e^{i\lambda_1 Mx} \tag{17}$$

Application of their analysis, based on equally spaced mesh points, to equation (16) shows that for small values of $h\lambda_1$, where h is the distance between adjacent mesh points and Dirichlet end conditions

$$E(\omega_K) < E_1 \sim \frac{E\, h^2 \lambda_1{}^3}{\sin[\lambda_1 (b-a)]} \tag{18}$$

for some constant E independent of the reduced frequency and mesh spacing. In view of the close relation between the φ_1 and ψ equations, we would expect the error behavior in the finite difference solution to be similar in both cases. Equation (18) displays several interesting characteristics. For example, the predicted error is directly proportional to the square of the mesh point spacing h and the third power of λ_1 or, for fixed Mach number, the third power of the reduced frequency ω. Also, the presence of the sin $[\lambda_1(b - a)]$ in the denominator of the equation introduces singularities in the error curve at values of ω (or λ_1) for which $\lambda_1(b - a) = n\pi$, n = 1,2,... These values of λ_1 correspond to eigenvalues of the analytical solution (eq. (14)): i.e., are values of λ_1 for which there is no unique analytical solution. Except near these singularities, the error curve as a function of λ_1 behaves like $\lambda_1{}^3$ times a slowly varying modulation factor. Thus over much of the range of λ_1 the error is essentially proportional to $\lambda_1{}^3$. Very near $\lambda_1 = 0$, the error is of course essentially proportional to $\lambda_1{}^2$ since $x/\sin x \to 1$ as $x \to 0$. This region is of little interest to the eigenvalue analysis, however. In view of the close relation between φ_1 and ψ equations, it is expected that the error behavior would also be the same for φ_1.

The presence of the singularities in the curve of ERROR versus reduced frequency is shown in figure 5 by the Δ-symbols. It would appear that the eigenvalues for the analytic system do not coincide exactly with the eigenvalues for the finite difference system, as noted by the distortions in the curves with which the points have been connected. The calculation was set up so that $E(\omega_K)$ would be evaluated at five points between each analytic eigenvalue. The singular behavior is the result of the evaluation of C_1 and C_2 from a set of simultaneous equations that are a function of the applied boundary conditions. This set of equations may be written in the form

$$[\alpha(\lambda_1)] \{C\} = \{\gamma\}$$

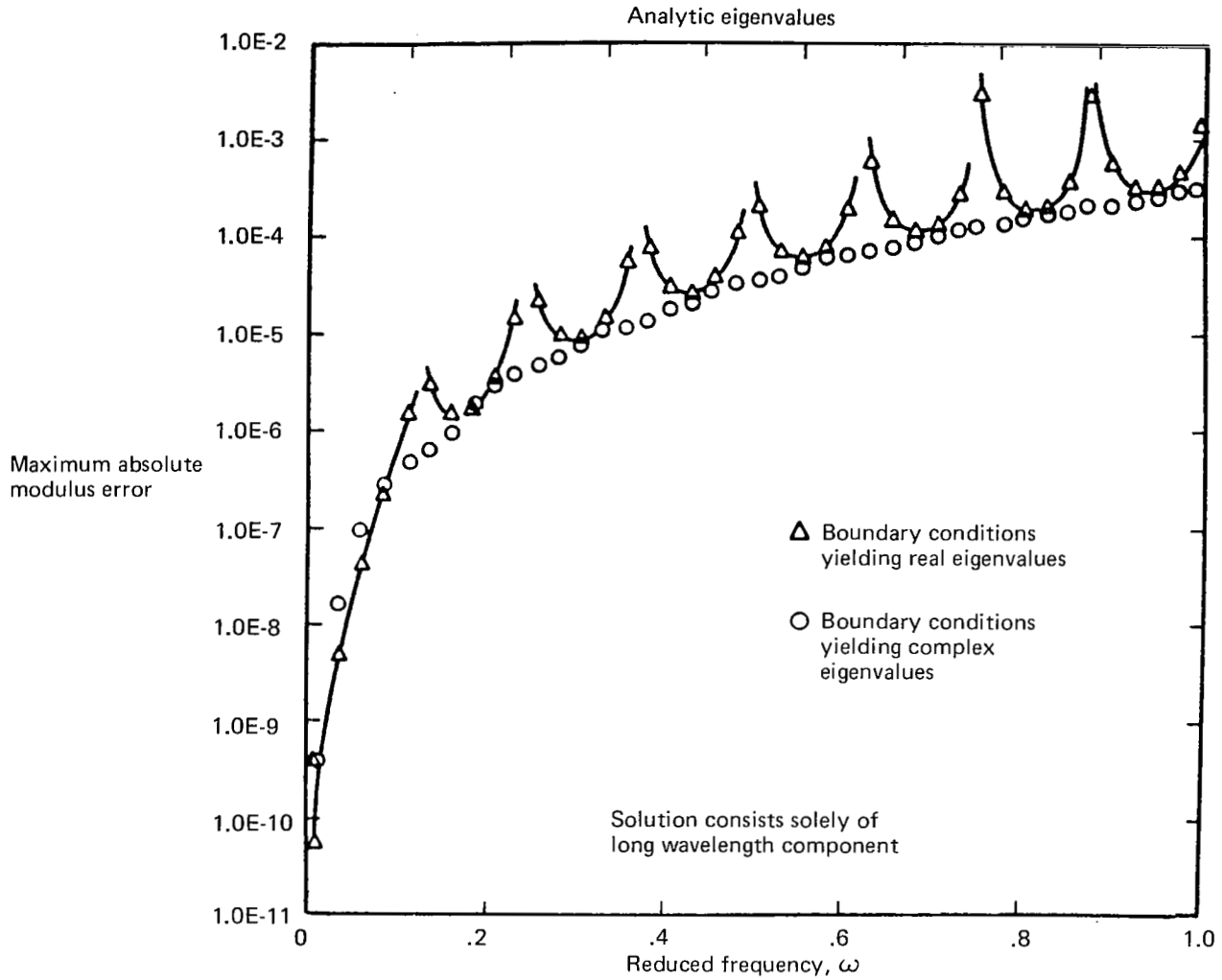

Figure 5.—Comparison of Error Curves for Boundary Conditions Yielding All-Real and Complex Eigenvalues

where α is a 2 x 2 matrix that is a function of λ_1 (or ω), C is the two-element column matrix made up of C_1 and C_2. The forms of α and γ are a function of the nature of the boundary (end) conditions; i.e., whether they are Dirichlet, Neumann, or Cauchy. Moreover, for certain values of λ_1, the determinant of α will be equal to zero. These certain values are eigenvalues. For values of λ_1 that correspond to eigenvalues, the solution for C_1 and C_2 is not unique; that is, for λ_1 equal to eigenvalues, there is no unique solution to equation (13).

It is interesting to note that the values of λ_1, which are eigenvalues of α, may be either all-real or complex depending on the nature of the boundary conditions. It is readily shown that Dirichlet conditions on both ends or Neumann conditions on both ends lead to all-real eigenvalues. However, for certain combinations, such as mixed conditions (Dirichlet on one end and Cauchy on the other), the eigenvalues may be made complex. Under these circumstances, we would not expect the violent peak and valley behavior of the error plots that result from the all-real eigenvalues. This is indeed confirmed with the results shown in figure 5 when the boundary conditions are such as to yield complex eigenvalues.

This problem was originally studied to see if it would shed light on the relaxation solution instability problem. In particular, it was of interest to see if relaxation solutions could be obtained for boundary (end) conditions for which the eigenvalues are complex. However, tests with a relaxation solution of the one-dimensional system have not converged and thus having complex eigenvalues does not seem to materially affect the convergence.

In addition it was noted that equation (18) implied that the error was essentially proportional to λ_1^3 or ω^3. An example of this is shown in figure 6 where an error curve for an example in which the singularity behavior has been suppressed is compared with a curve proportional to ω^3. The correlation between the two is very good. Also included is a curve that is proportional to ω^4, as predicted by a conventional truncation analysis of the finite difference equation.

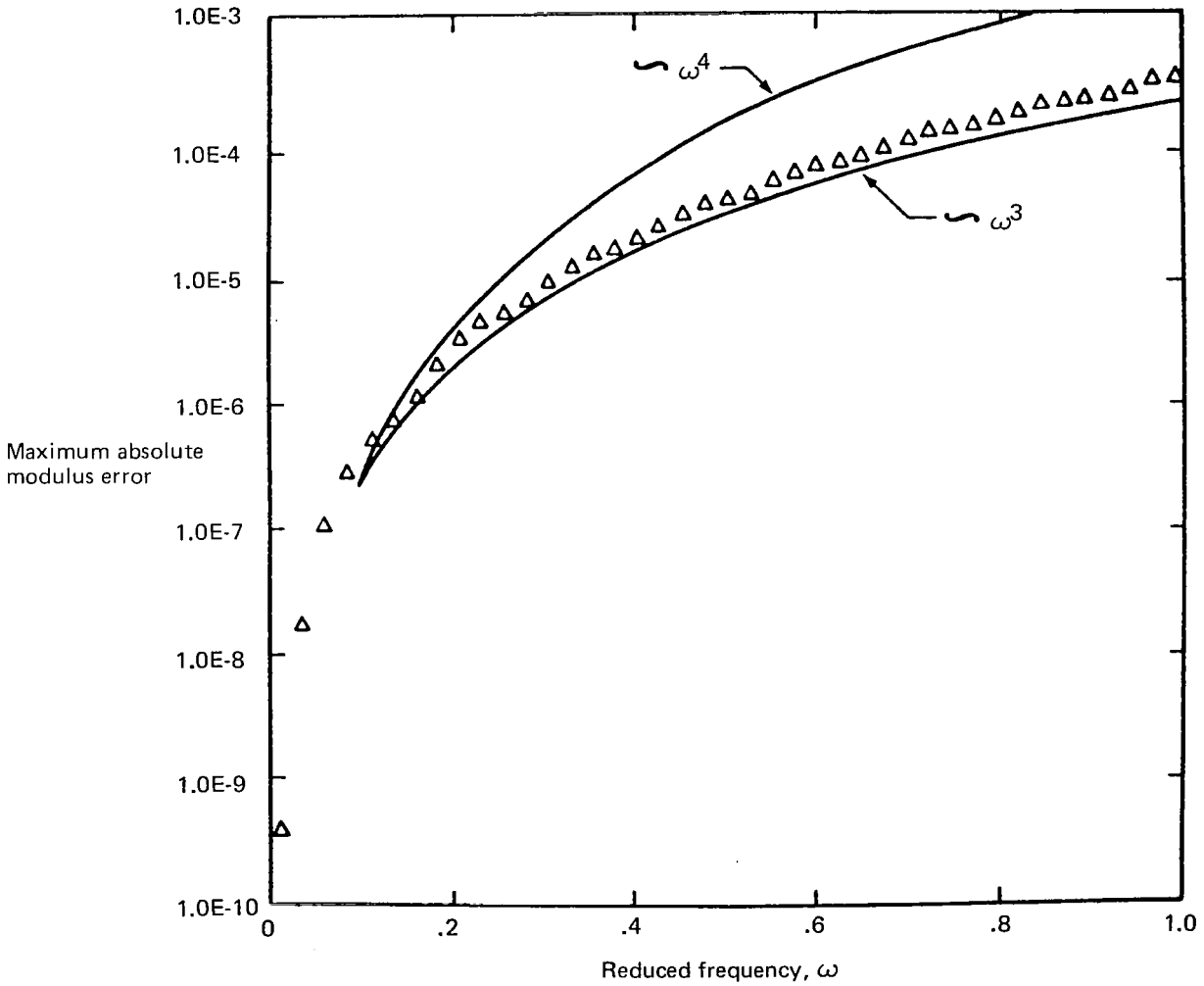

Figure 6.—Variation of Error Curve With Reduced Frequency

In summary, analysis and experiment of the one-dimensional equation show that the error from the finite difference solution is essentially proportional to $h^2\lambda_1^3$, and thus the number of points has to be expanded (or more specifically the mesh spacing reduced) in proportion to the 3/2 power of the frequency in order to retain accuracy. The level of the error is determined by the boundary conditions and, in turn, determines the relative contributions to the solution by the long and short wavelength components. The relatively larger part the long wavelength component plays, the smaller the level of error. Superposed on this general error curve can be a series of peaks and valleys with the peaks centered around the values of λ_1 (or ω) that correspond to the real eigenvalues of the system of finite difference equations and are dependent on the boundary conditions. If the eigenvalues are complex, the peak-valley behavior of error curve is suppressed.

These results would indicate that, for certain choices of boundary conditions and sufficiently fine mesh spacing, adequately accurate results may be obtained in the two-dimensional case using a full direct solution method.

6.2 TWO-DIMENSIONAL EXAMPLES

As noted in section 5.3, a complete direct solution using outgoing wave boundary conditions permits obtaining solutions at large values of reduced frequency, and solution stability no longer is a problem. However, for the mesh sizes used, the correlation between the finite difference solutions and linear theory becomes very poor. Results are presented here for a two-dimensional airfoil of vanishing thickness oscillating in pitch in a freestream of M = 0.9. Under these conditions, relaxation solutions would be expected to be unstable at reduced frequencies (based on the semichord) above approximately 0.12 according to equation (10). Results were obtained using both the linear theory program and the finite difference program. Very good correlation between the two theories was obtained at $\omega = 0.06$ (see fig. 2), and very poor correlation at $\omega = 0.3$ as shown in figure 7. The correlation was significantly degraded even at $\omega = 0.09$ as shown in figure 8. To test whether this phenomenon was a function of λ_1 rather than ω, the same problem was rerun at a Mach number of 0.4 with reduced frequencies so that the values of λ_1 were the same. Correlation between results from linear and finite difference calculations, as shown in figures 9 and 10, was good for $\omega = 0.6$ (corresponding to $\omega = 0.06$ at M = 0.9) and poor at $\omega = 0.9$ (corresponding to $\omega = 0.09$). The results at $\omega = 3$, which are not shown, were very bad. Thus, the results from the full two-dimensional transonic problem (although with nonmixed flow) appear to follow the same pattern as the results from the very simplified one-dimensional example. Indeed, the poor results appear to be due to the same cause as the peaks in the error curve shown in figure 5, but this requires further study. In particular, since the true eigenvalues of this problem are not known, it is difficult to assess whether the higher frequencies tried are near eigenvalues without further investigation of the sensitivity of accuracy as a function of frequency.

These results were checked using a direct solution routine incorporating partial pivoting with equilibration. The results were not changed, although it was possible to tell that the pivoting portion of the routine had been used. Thus, the errors encountered with the two-dimensional calculations do not seem to be due to numerical problems

resulting from ill-conditioned matrices. Increasing the number of mesh points in order to improve correlation was not feasible with available computer resources. Decreasing the number of mesh points would not have provided a realistic representation of the physical problem.

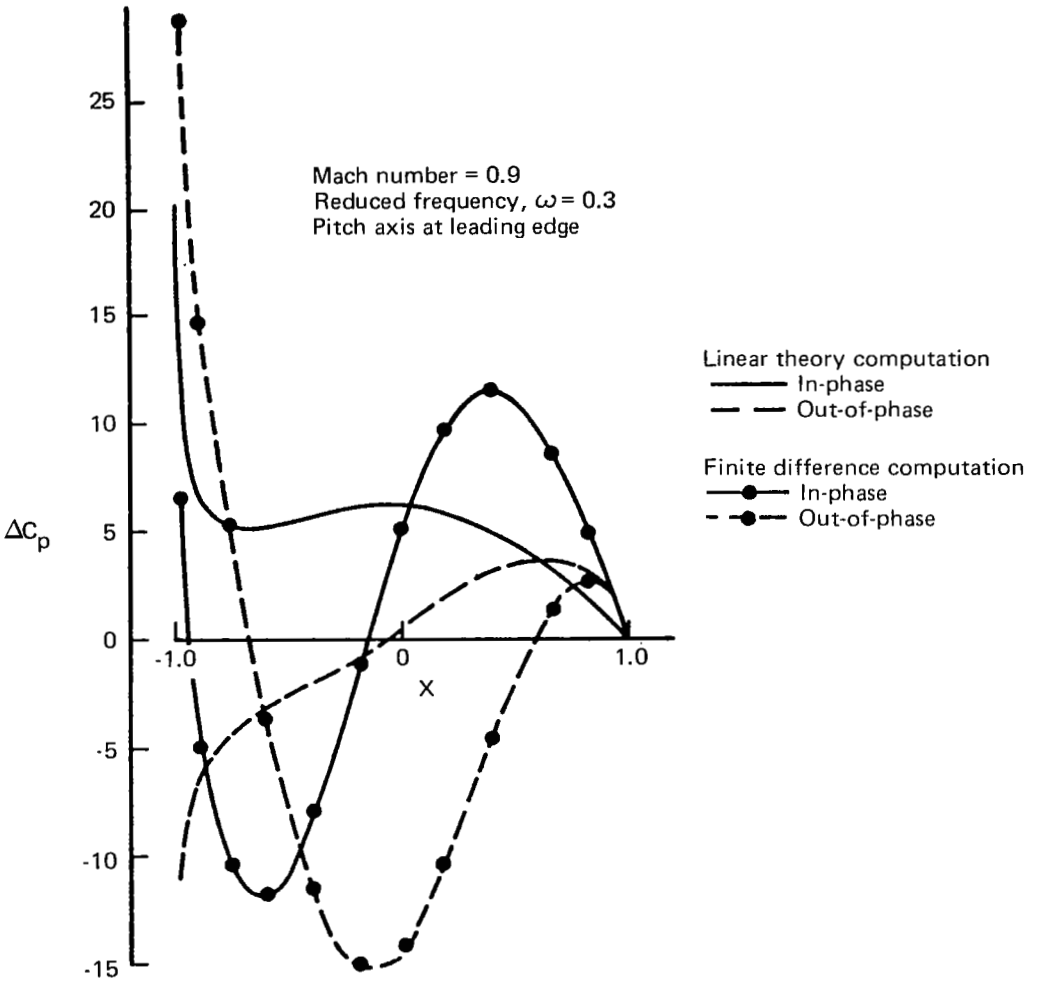

Figure 7.—Jump in Pressure Coefficient Across a Flat Plate Oscillating in Pitch, M = 0.9, ω = 0.3

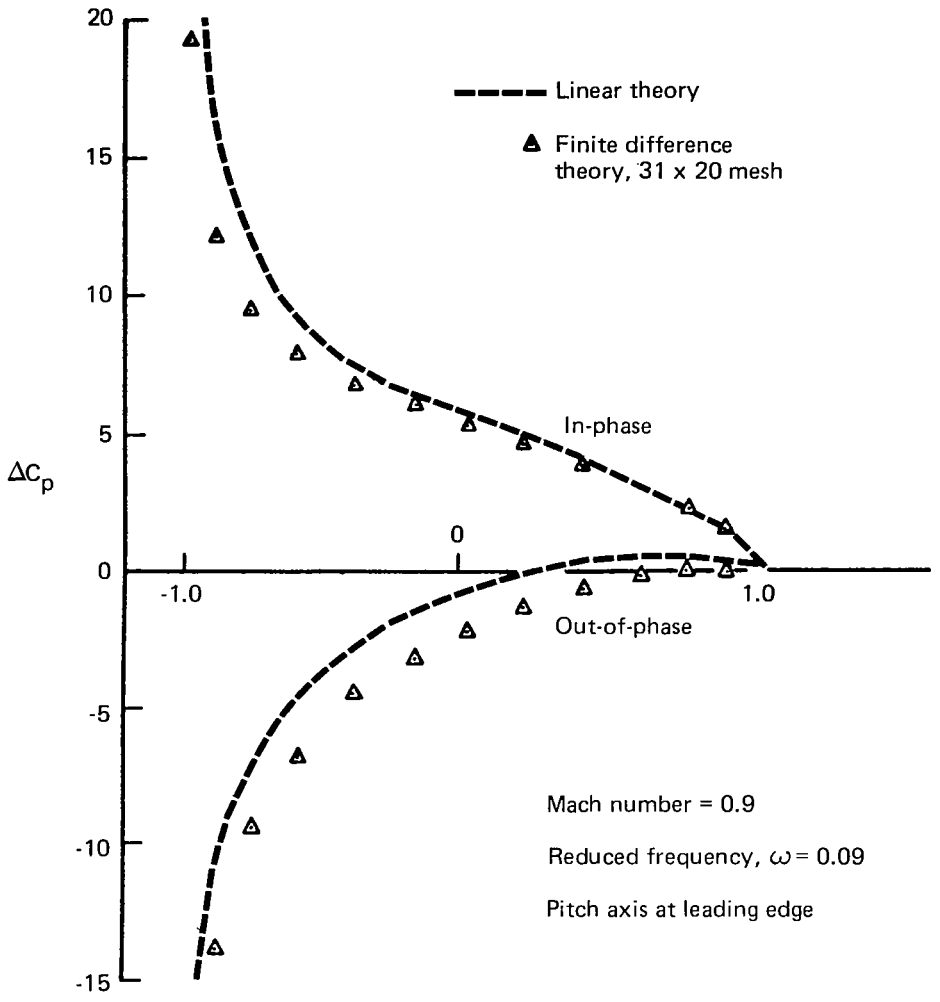

Figure 8.—Jump in Pressure Coefficient Across a Flat Plate Oscillating in Pitch, M = 0.9, ω = 0.09

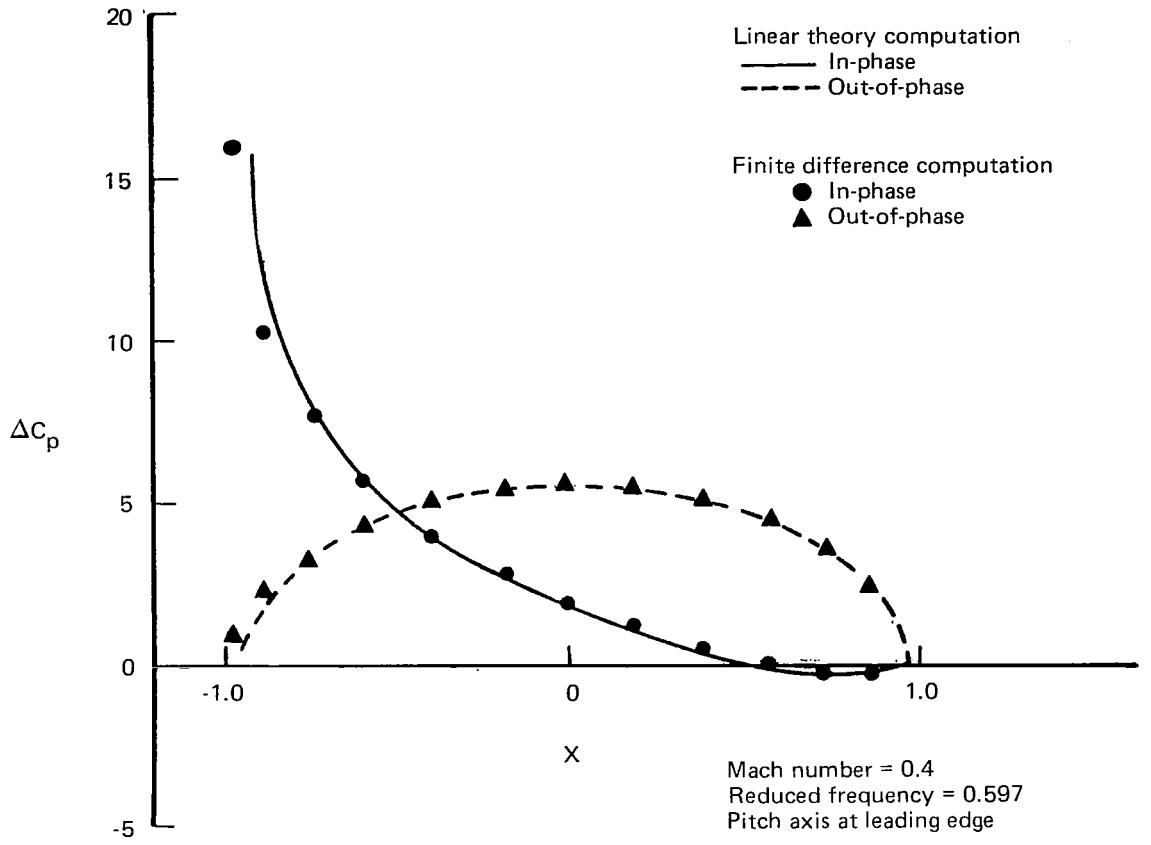

Figure 9.—Jump in Pressure Coefficient Across a Flat Plate Oscillating in Pitch, M = 0.4, ω = 0.597

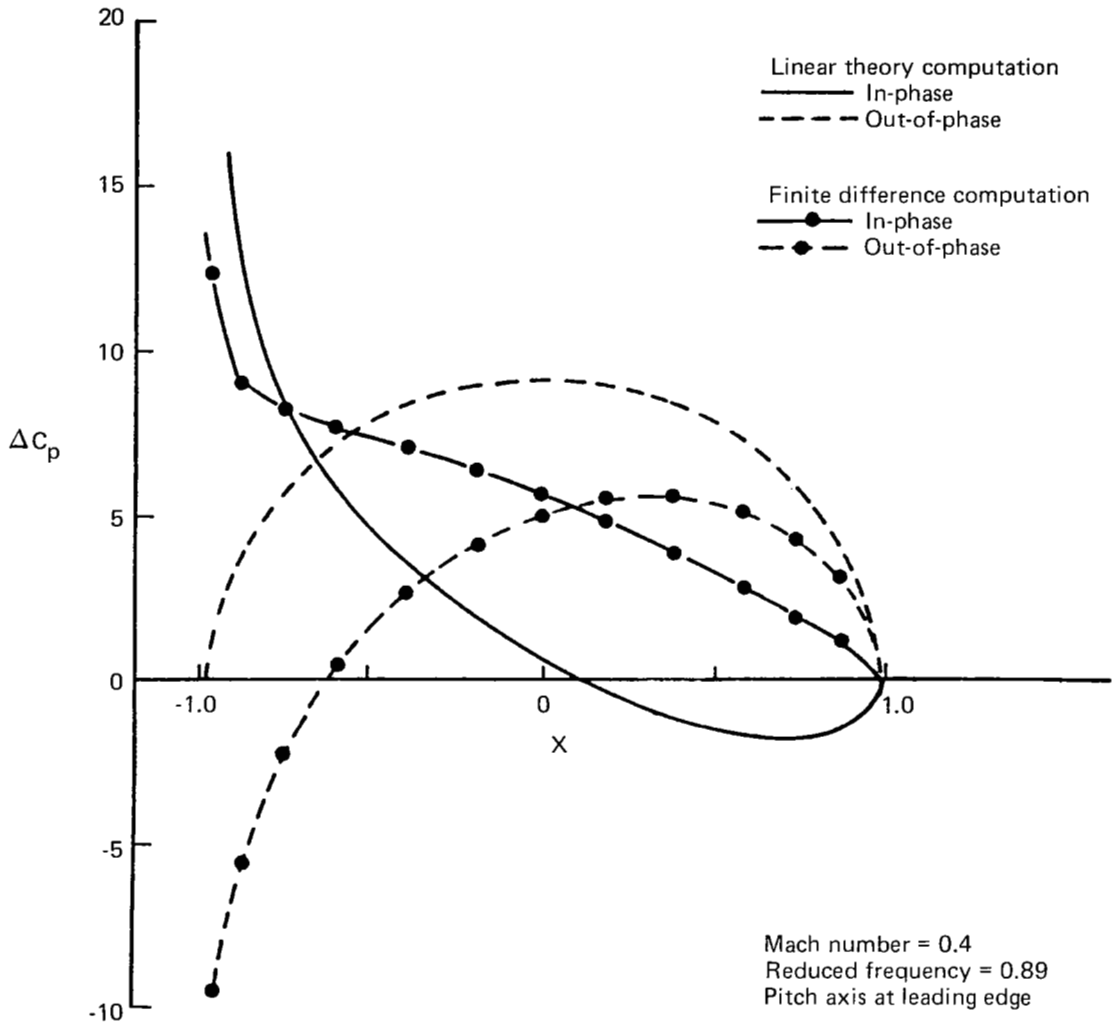

Figure 10.—Jump in Pressure Coefficient Across a Flat Plate Oscillating in Pitch, $M = 0.4$, $\omega = 0.89$

7.0 THREE-DIMENSIONAL PROGRAM STUDIES AND ANALYSES

Modifications to the three-dimensional program as described in reference 5 are described in section 7.1. The results of applying the resulting program to the NASA transonic unsteady pressure model of low-aspect ratio clipped delta planform are presented in section 7.2. Section 7.3 presents results for a moderate-aspect-ratio rectangular wing.

7.1 THE THREE-DIMENSIONAL PROGRAM

The pilot three-dimensional program as described in reference 5 was restricted to lifting surfaces with rectangular planforms. This program has been revised, and its design and usage documented in reference 19. The revised program is valid for wings with aft-swept leading and trailing edges. The leading edge may be curved (of arbitrary shape), but the trailing edge must be straight. This last limitation is due to the method of programming rather than being a restriction on the theory. In addition, the program has been revised to:

1. Include the capability for row relaxation as well as the original column relaxation

2. Make use of the anti-symmetry characteristics of the unsteady flow about symmetric wings so that only half the flow is actually calculated

Row relaxation proved much faster than column relaxation for the two-dimensional problem. The same appears to be true from the minimal number of three-dimensinoal examples we have run. However, it should also be noted that solution instabilities have again been encountered in the mixed flow case, and the results of the following section for the configurations with thickness were obtained using column relaxation. It was noted in reference 5 that, for the two-dimensional problem, row relaxation was much more efficient than column relaxation in terms of reaching a specified degree of convergence in a minimum number of iterations. It was determined that in using row relaxation for mixed flow, additional terms must be included in the finite difference equation for hyperbolic points to avoid solution instabilities. These additional terms have not proved enough to avoid instabilities in the three-dimensional row relaxation solution, and it is assumed that the two-dimensional analysis of reference 5 should be extended to the three-dimensional equations.

A derivation of the wake integral for a straight trailing edge perpendicular to the wing root was given in appendix B of reference 5. A general form, valid for wings with trailing edges, that may be described by a single valued function of the form

$$x_t(y) = 1 + f(y)$$

where f(y) ≥ 0, is derived in appendix B of this report. The resulting form again makes use of Gauss-Laguerre integration and is directly parallel to the form derived in reference 5 for the trailing edge of an unswept rectangular wing.

The three-dimensional program, which is considered to be a pilot program, has been provided to NASA-Langley and is documented in reference 19. The program has been modified and permits calculations including swept leading edges while using an unswept rectangular mesh point array.

7.2 RESULTS FOR A DELTA WING

This section presents the results of applying the pilot three-dimensional program to a wind tunnel model built by NASA-Langley for testing in the Langley Transonic Dynamics Tunnel. The model has a clipped delta planform with a 50.5° swept leading edge and a circular-arc profile with a thickness ratio of 6%. The model geometry is shown in figure 11. The model is designed to be oscillated in pitch and flapping, and every effort has been made to minimize the structural deflections resulting from these rigid body motions. The model is half-span and is mounted on the side of the tunnel through a splitter plate designed to remove the wall boundary layer.

The calculations were performed at M = 0.9 for the wing oscillating in pitch and flapping at a reduced frequency based on the root semichord of 0.06.

The steady-state pressure distribution for the wing is shown in figure 12. It was calculated using a program developed at NASA-Ames by Ballhaus and Bailey (ref. 20) and modified by The Boeing Company. It does not include a shock point operator. The ideas of Schmidt (ref. 21) were used to set up the mesh along the swept leading edge. The calculations were made for a mesh with 55 points in the flow direction, 32 points in the spanwise direction (half-span), and 36 points in the vertical direction. Convergence for the pitch mode and the flat plate configuration with ERROR $\leq 10^{-4}$ and using row relaxation was obtained in about 100 iterations. Starting with this solution and using column relaxation, about 50 iterations were needed to obtain the solution for the circular-arc airfoil shape. With solutions calculated assuming symmetry with respect to the x-y plane and using a CDC 6600 computer with an FTN compiler, the number of CPU seconds per iteration was about 7 and the number per far-field update was about 9.

The jump in pressure coefficient due to harmonic pitch and flapping is presented in figures 13 and 14. In each case, three different results are presented. The first result is from using the NASA subsonic unsteady three-dimensional airloads program (refs. 15 and 16). This should compare directly with the second set of results, which are the finite difference results for a flat plate. The third data set is from using the finite difference program for the wing with the coefficients of the differential equation obtained from the nonlinear steady-state solution from the transonic small perturbation theory.

Generally, linear results correlated very well with the corresponding finite difference results for a flat plate. This was particularly true for the pitch mode and only slightly less so for the flapping mode. Note that the scale used for the real part of the flapping mode is significantly larger than the scale used for the imaginary part. The failure of

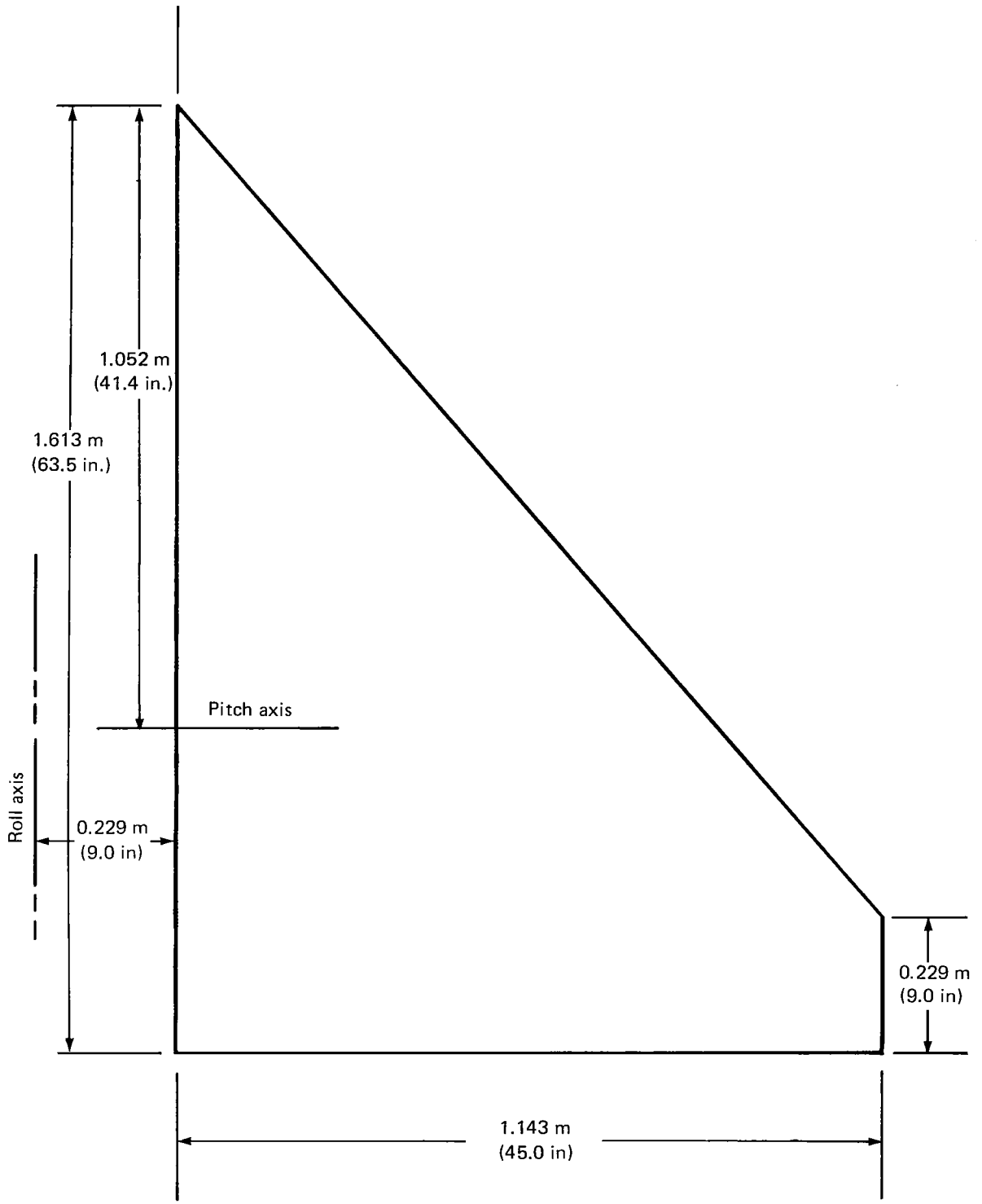

Figure 11.—Planform Geometry for NASA Transonic Pressure Model

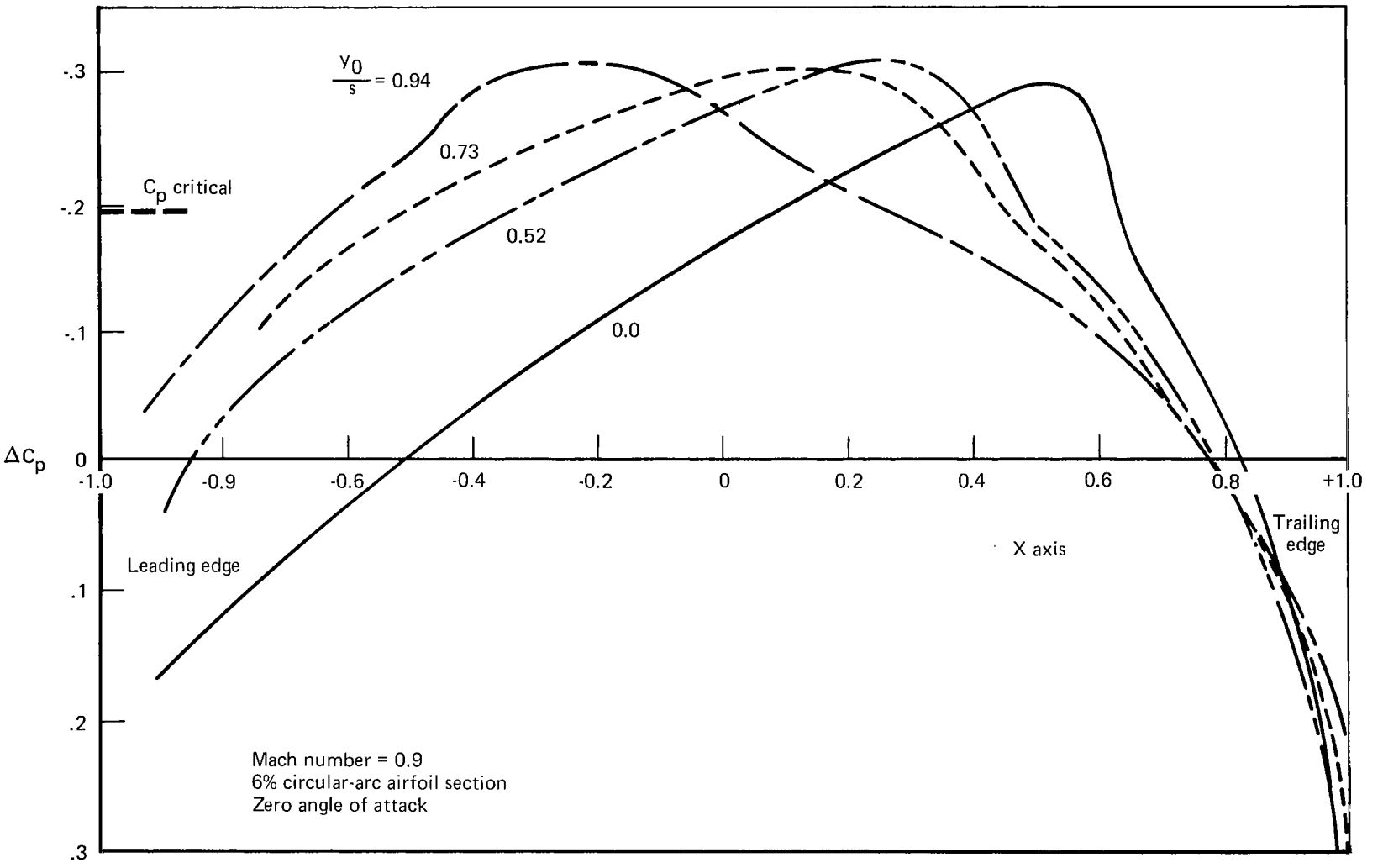

Figure 12.—Steady-State Pressure Coefficient Distributions for a Low-Aspect-Ratio, Clipped Delta Wing

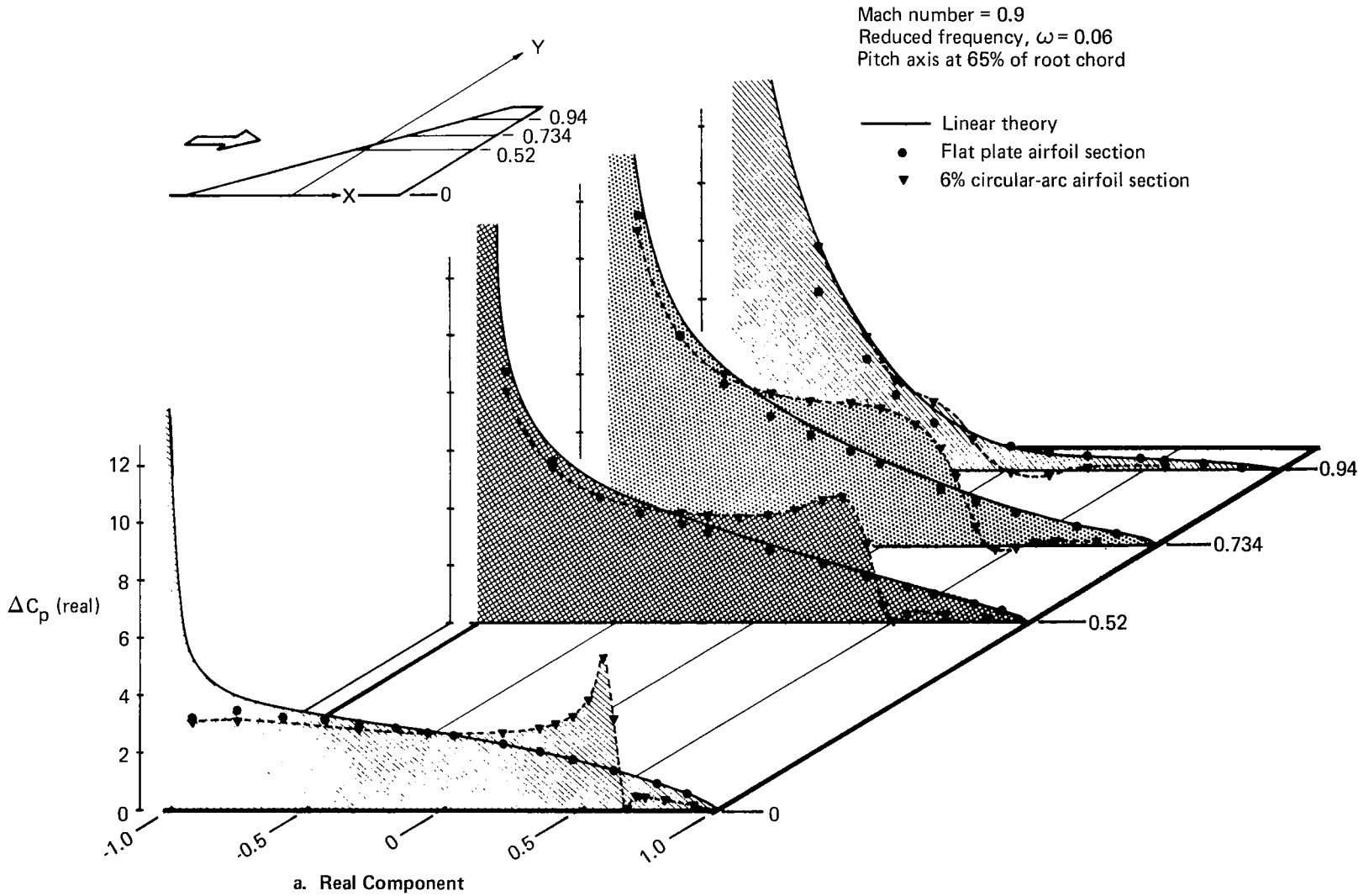

Figure 13.—Pressure Coefficient Distributions for a Low-Aspect-Ratio, Clipped Delta Wing Oscillating in Pitch

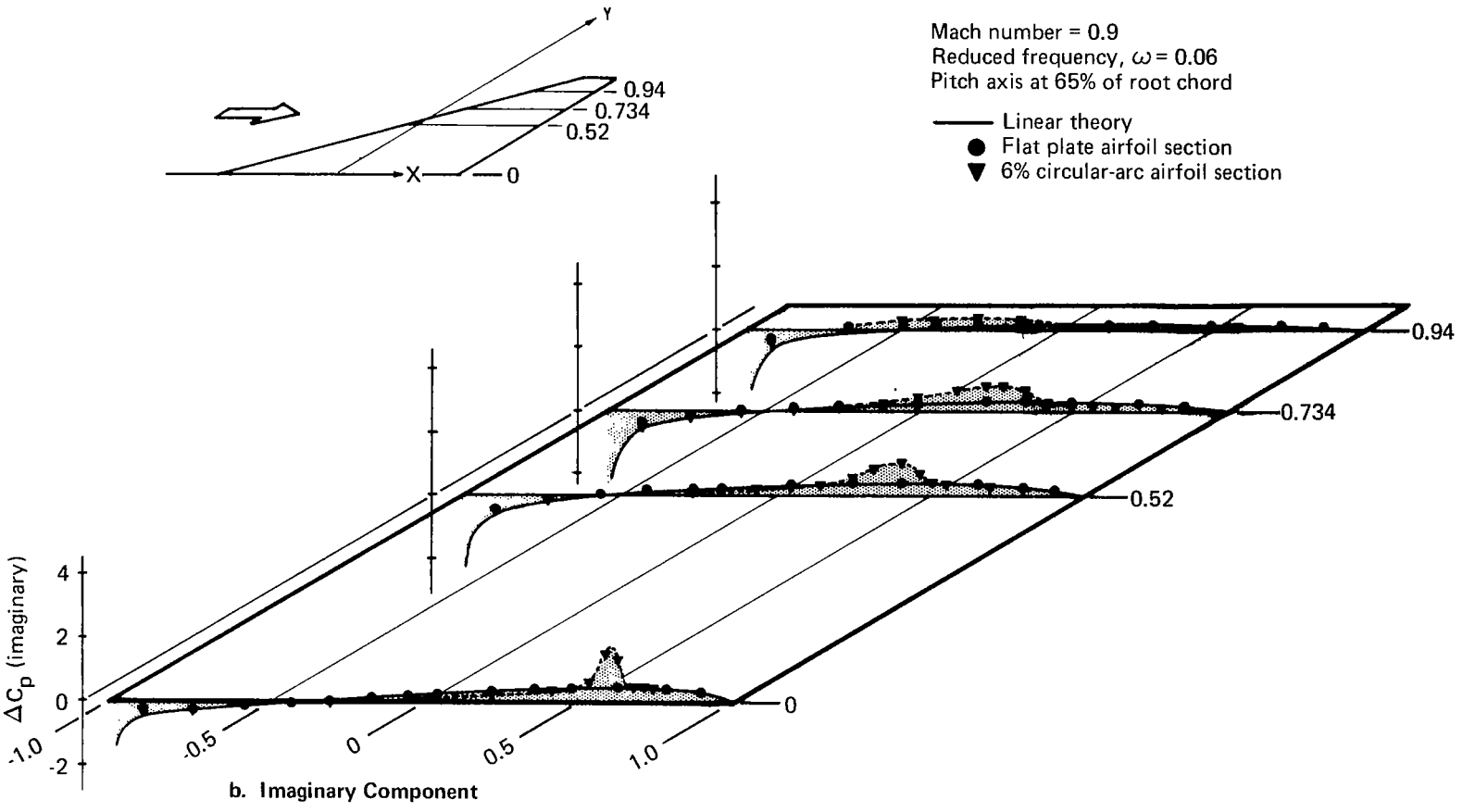

Figure 13.—(Concluded)

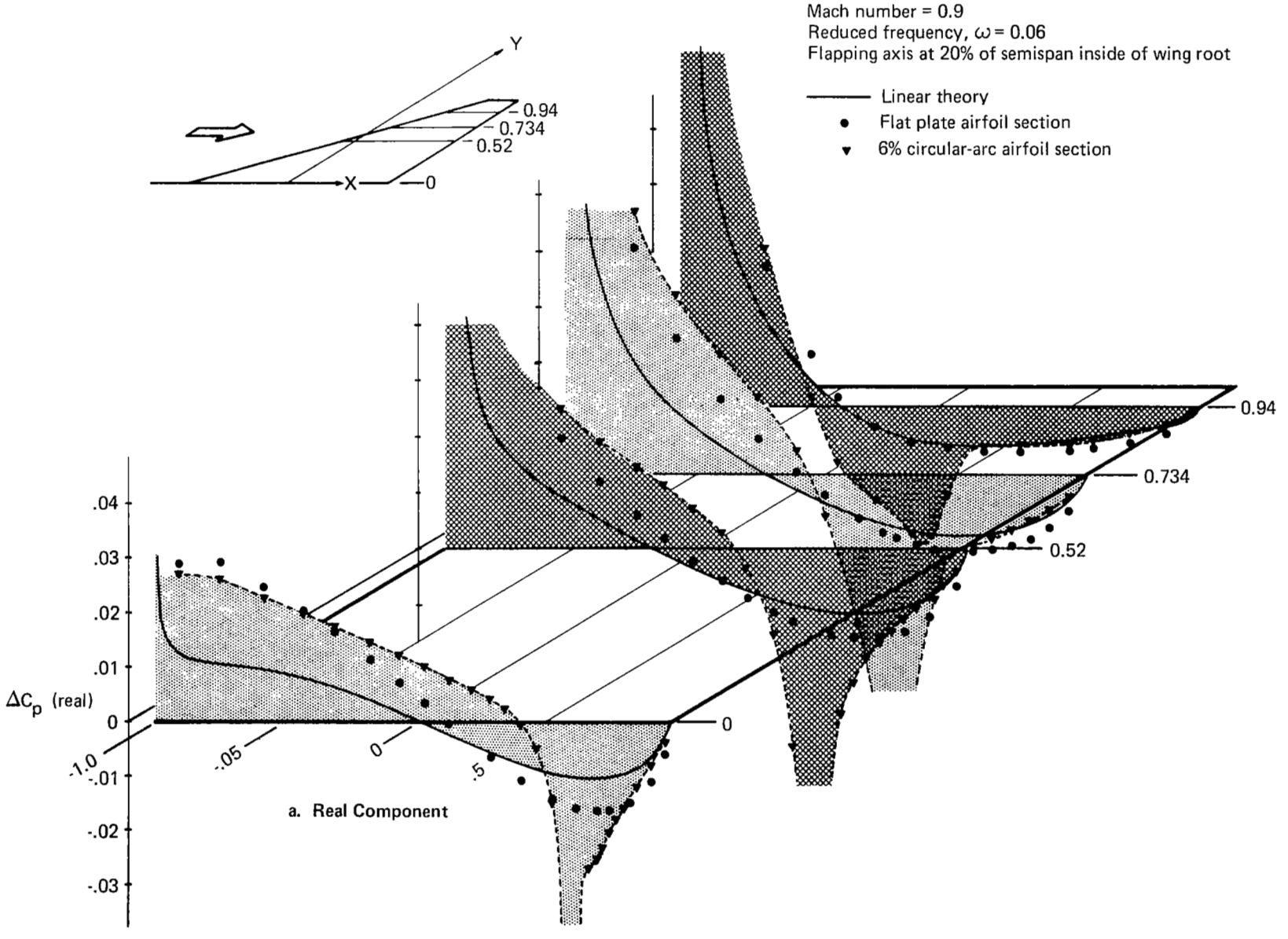

Figure 14.—Pressure Coefficient Distributions for a Low-Aspect-Ratio, Clipped Delta Wing Due to Flapping

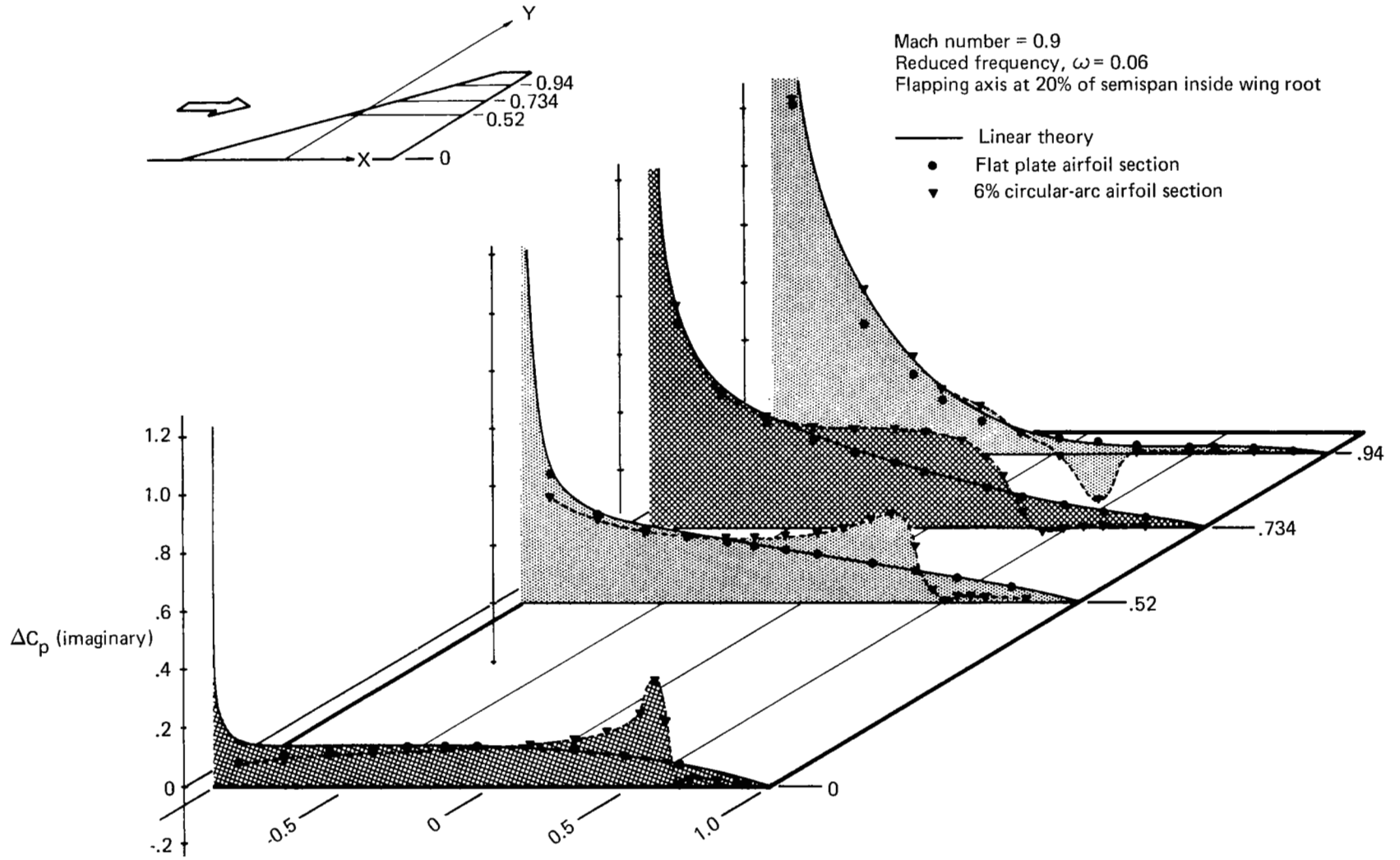

b. Imaginary Component

Figure 14.—(Concluded)

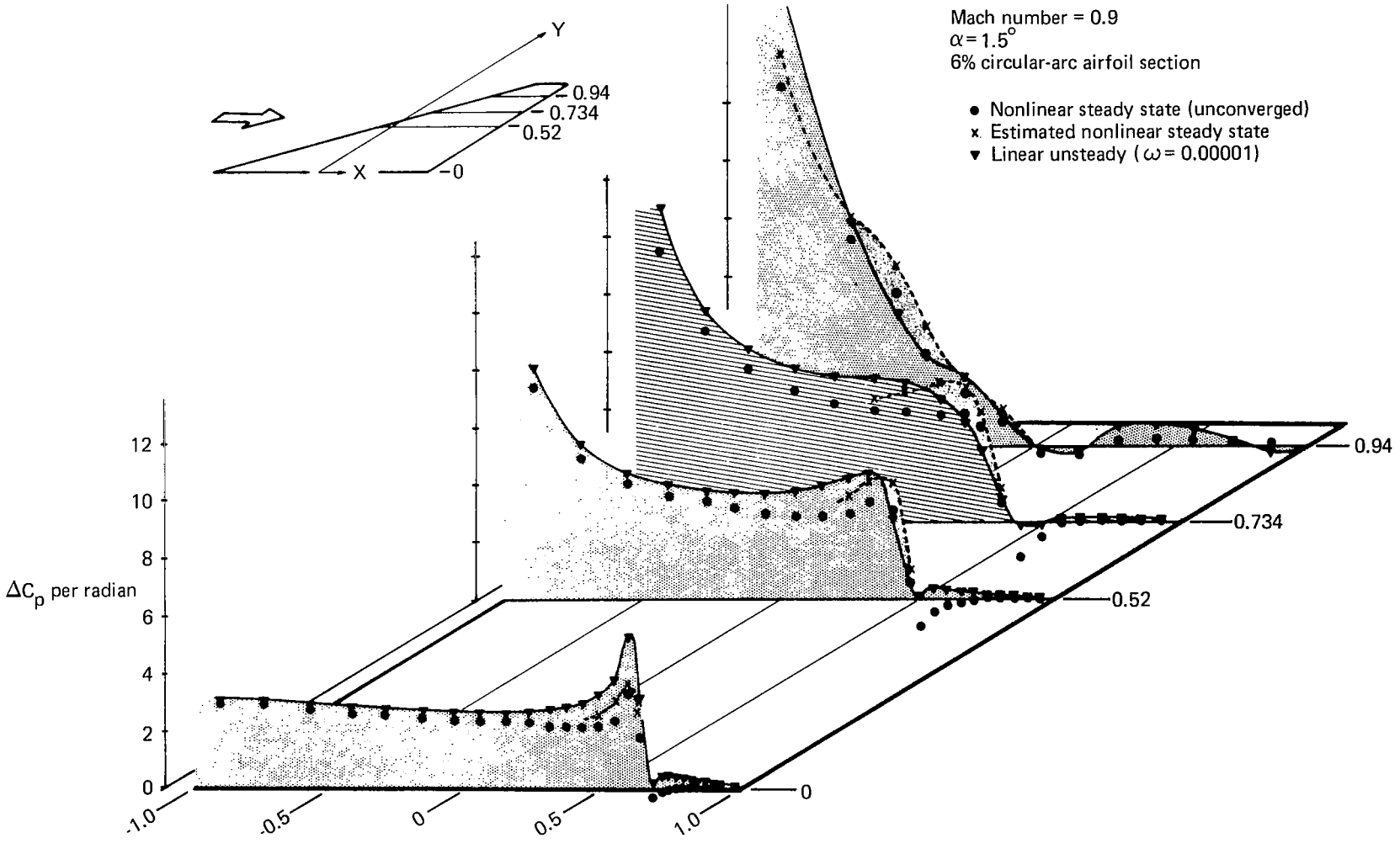

Figure 15.—Pressure Coefficient Distributions for a Low-Aspect-Ratio, Clipped Delta Wing at Angle Of Attack

the finite difference solution to provide a singularity at the wing leading edge at the root is attributed to the relative sparsity of points over the apex of the wing. In setting up the finite difference pattern, it was decided to emphasize the points on the aft portion of the wing and in the wake. From practical considerations, then, the planform apex was somewhat slighted in terms of points.

The finite difference solution with thickness showed the usual peaks in the unsteady pressure in the region of the shocks as calculated in the steady flow. No experimental data are available at this time for comparison purposes.

Results for the delta wing at an angle of attack are presented in figure 15. The first set of results was obtained using the nonlinear steady-state finite difference program for an angle of attack of 1.5^{o}. The results are presented as jump in pressure coefficient per unit radian. The results from the nonlinear steady-state program were not fully converged; however, estimated converged results were indicated in the neighborhood of the shock as obtained using the Aitken-Shanks nonlinear transformation (δ^2-process) of reference 22. The second set of results was from the unsteady program using a pitch mode and a very small reduced frequency of $\omega = 0.00001$. Only the real part of the resulting presure vector is plotted. The thickness effects in the unsteady program resulted from the steady velocity potential at zero angle of attack from the nonlinear program. The computer resources required to obtain the set of results from the linear unsteady program were significantly less than those required for the results from the nonlinear steady program.

The pressure coefficient distributions from the two solutions exhibited the same characteristics with greater amplitude in the shock region for the linear unsteady solution for a very small frequency than for the steady nonlinear solution. Both solutions were obtained without using a shock point operator.

7.3 RESULTS FOR A RECTANGULAR WING

The revised three-dimensional program was also used to recalculate the pressure distribution over an aspect ratio 5 rectangular wing oscillating in harmonic pitch. A Mach number of 0.875 was used with a reduced frequency based on the root semichord of 0.06. These results as presented in references 5 and 6 were calculated using an incorrect scale factor on the steady-state velocity potential distribution. The effect of correcting this scale factor is to provide a noticeably larger pressure rise due to the presence of the shock. There still remains, however, a significant attenuation of this rise in going from the two-dimensional to the three-dimensional configuration.

A mesh of 44 points in the flow direction, 32 points in the spanwise direction for the full span, and 26 points in the vertical direction was used. The finite difference region extended about one chord length in front of the leading edge and behind the trailing edge, about seven chord lengths above and below the wing surface, and slightly more than a semispan beyond the wingtip. The rerun has permitted a comparison of running times between the original program, using a KRONOS 2.1 operating system on the CDC 6600 using the RUN compiler and the current program using an FTN compiler. The average number of CPU seconds per iteration is now approximately 2 compared to about 8 before, and approximately 2½ CPU seconds per far-field update compared to 9 before.

For the case shown, the converged solution (in this case the ERROR of eq. (9) was to be less than 10^{-4}) was of the order of 180 iterations with the initial unsteady velocity potential distribution set to zeros.

Figure 16 shows the steady-state pressure distribution for a NACA 64A006 profile, which was obtained using a program developed by Ballhaus and Bailey (ref. 20). The jump in pressure coefficient due to harmonic pitch about the planform leading edge is shown in figure 17, with three different results presented. The first results are from the NASA subsonic unsteady three-dimensional airloads program using linear theory (refs. 15 and 16). These should compare directly with the second set of results calculated using the finite difference program and a flat plate airfoil section. The third data set is from using the finite difference program with the steady velocity potential distribution from the nonlinear steady-state solution for the wing with a NACA 64A006 profile. In addition, a two-dimensional result from finite difference theory for the same airfoil section is shown in the planform root plane.

Generally, the linear results correlate very well with the corresponding finite difference results for a flat plate. The results including thickness display the pressure rise in the neighborhood of the shock that has been characteristic of corresponding experimental measurements (for example, see ref. 10). The three-dimensional results show a significant softening of the pressure rise in comparison with the two-dimensional results. Of concern is the apparent intensifying of the shock effect at the midpoint of the semispan of the wing. The reason for this result, which is not expected physically, is currently attributed to the way the finite difference operators are handled. The program is written to use central differencing for subsonic points (as determined from steady flow) and backward differencing for supersonic points. An abrupt change in the pattern of subsonic and supersonic points occurs on the chord adjacent to the one with the sharpest shock effects.

In an attempt to smooth out the shock effects spanwise, a shock point operator in conservation form was introduced into the three-dimensional program. The derivation of the operator is given in appendix C. The result of using the shock point operator was to (1) significantly increase the effect of the shock on the unsteady pressure distribution and (2) smooth out the spanwise pressure distribution in the neighborhood of the shock. A comparison of distributions calculated with and without the shock point operator is shown in figure 18. Note the significant increase in the magnitude of the pressure rise due to the shock at the wing root, with a much smaller increment in the rise at midspan. No experimental data are available at this time for comparison purposes.

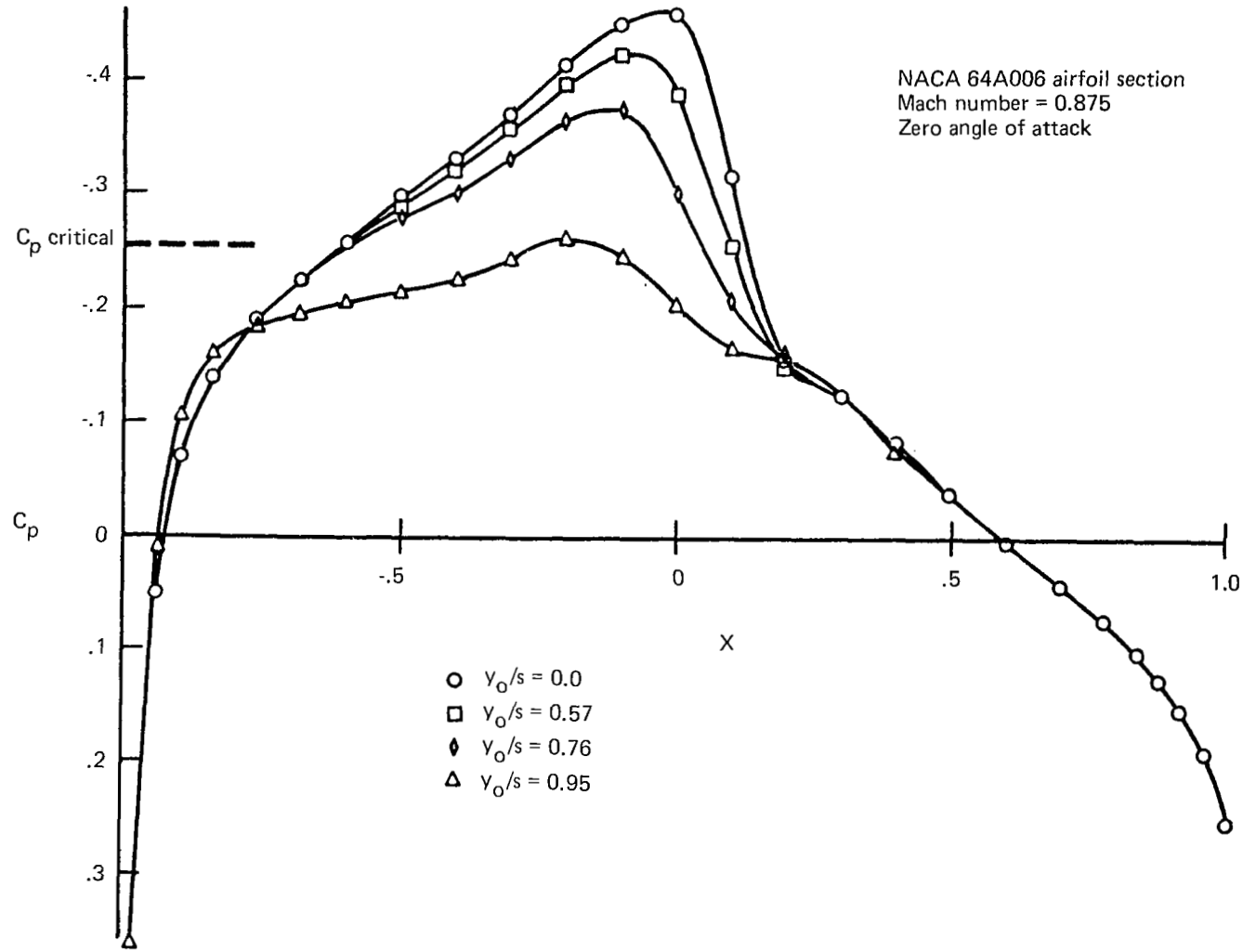

Figure 16.—Steady-State Pressure Coefficient Distributions for an Aspect Ratio 5 Rectangular Wing

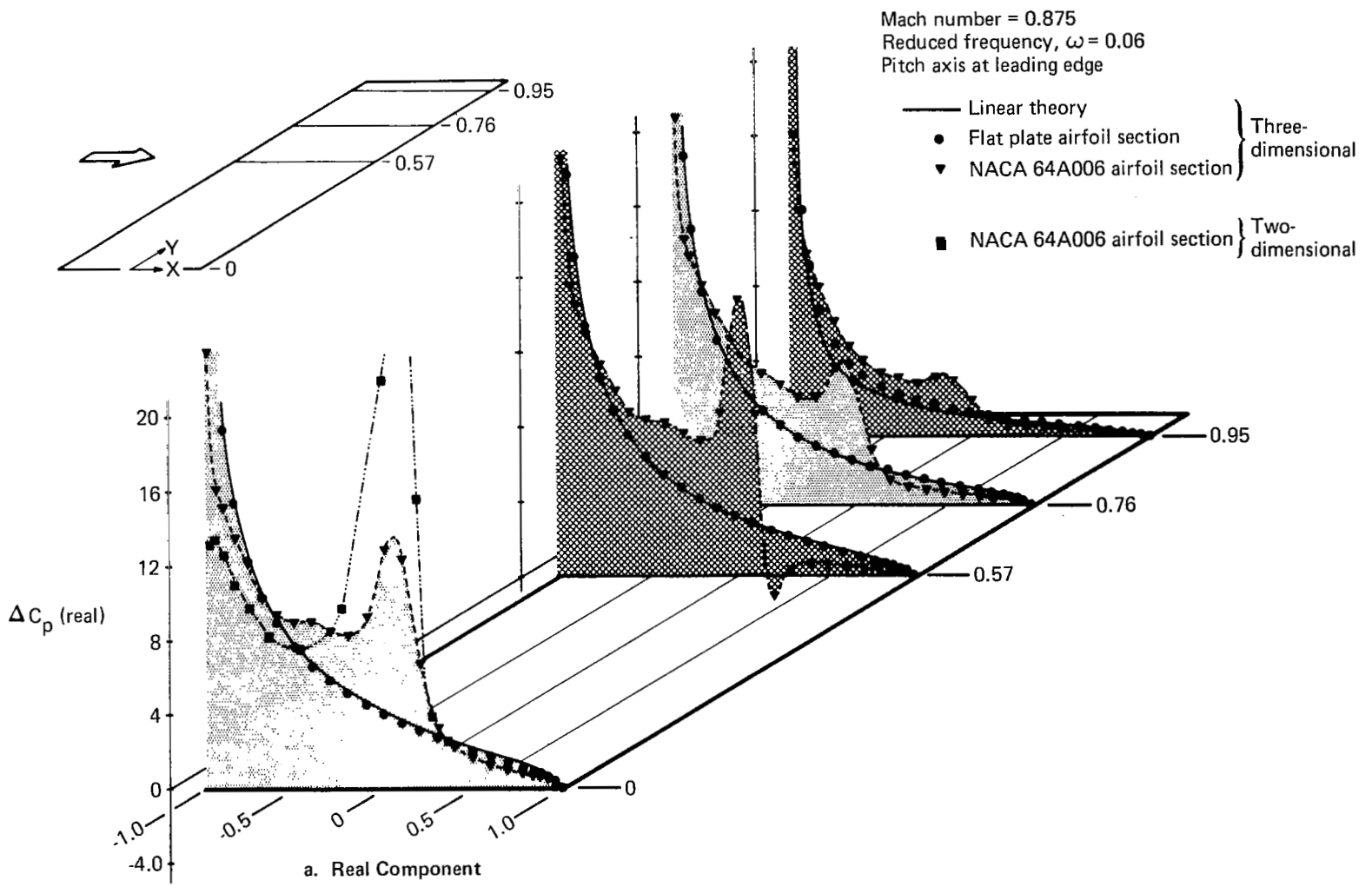

Figure 17.—Pressure Coefficient Distribution for an Aspect Ratio 5 Rectangular Wing Oscillating in Pitch

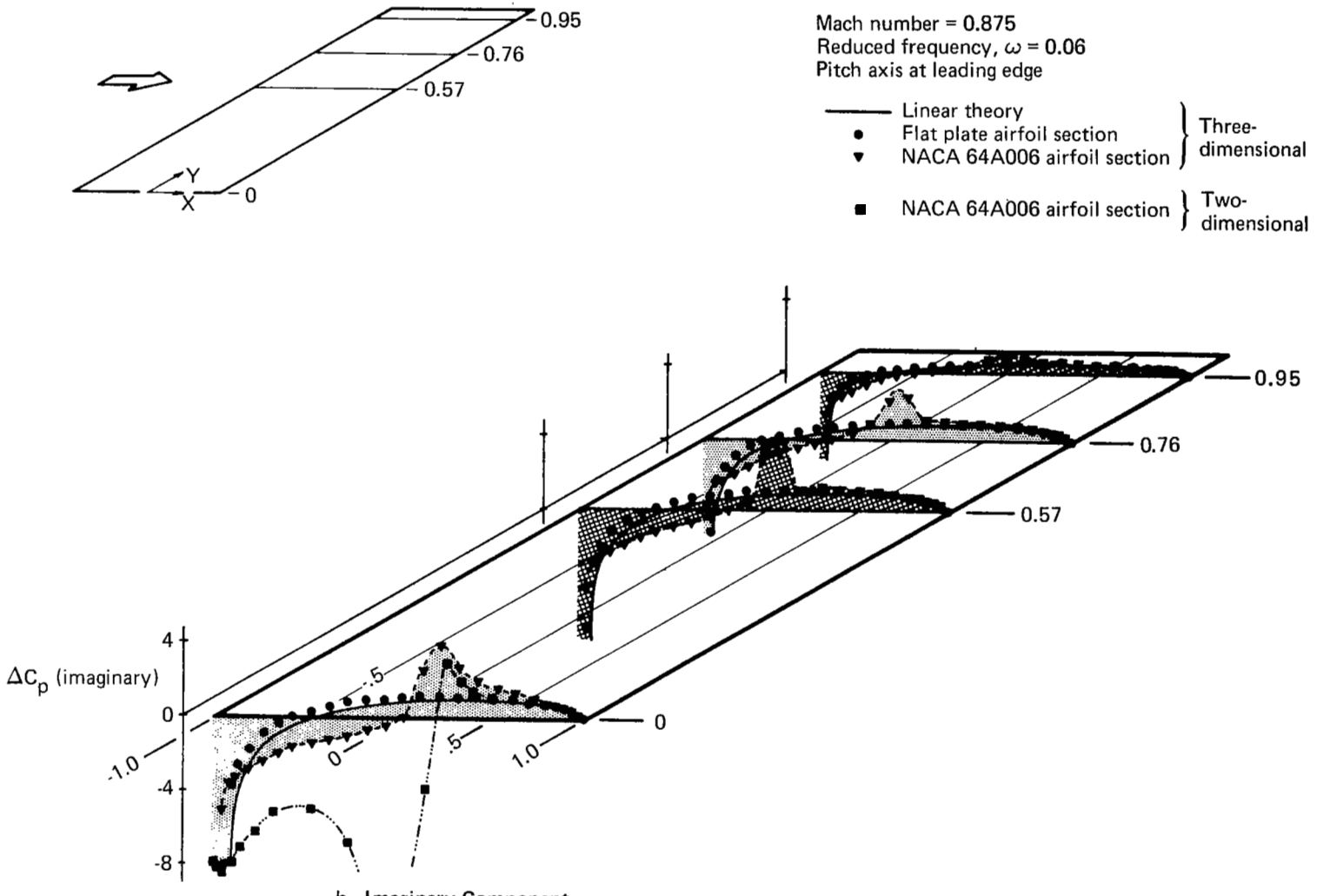

b. Imaginary Component

Figure 17.—(Concluded)

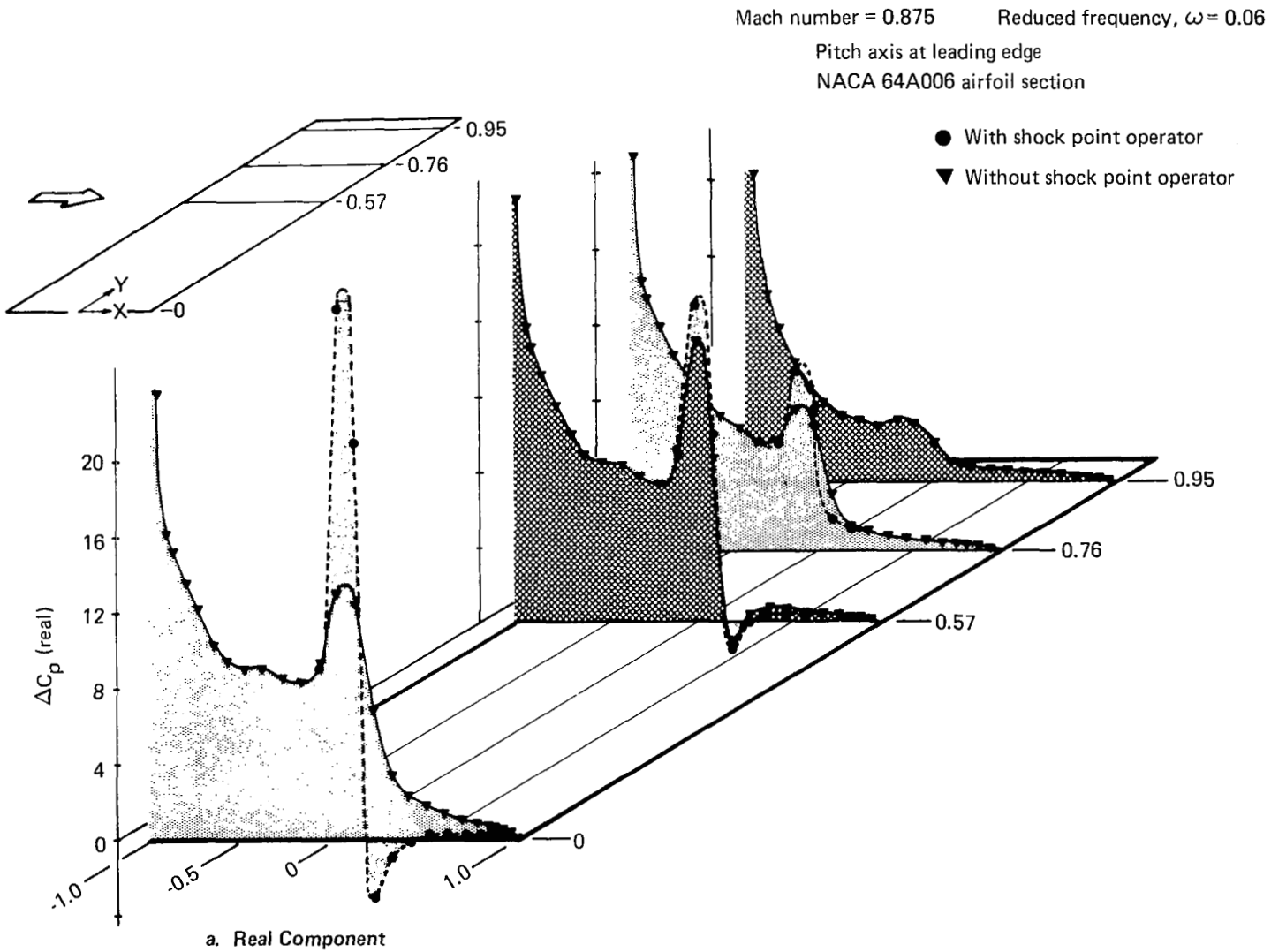

Figure 18.—Comparison of Pressure Distributions Calculated With and Without a Shock Point Operator

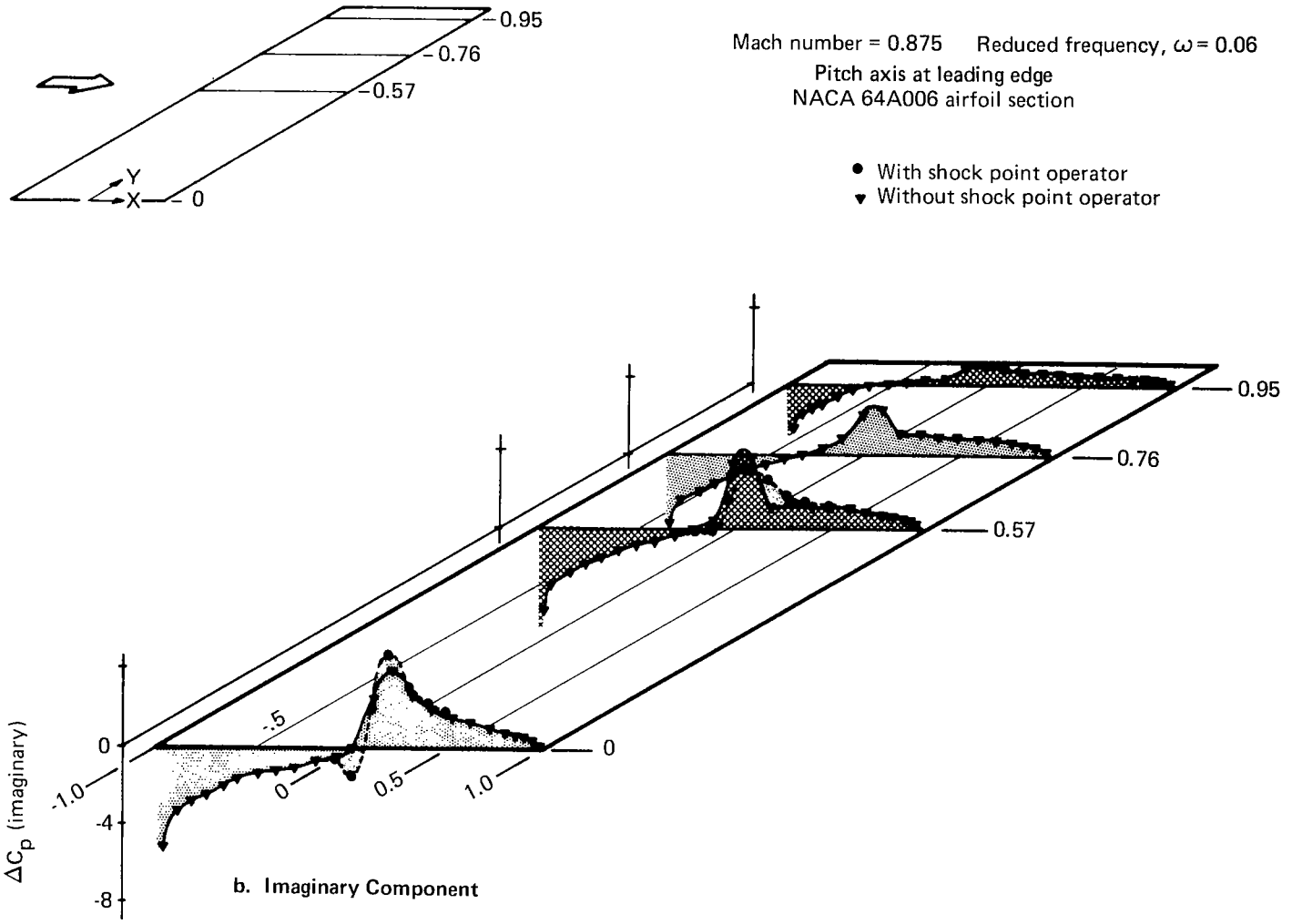

Figure 18.—(Concluded)

8.0 SUPERSONIC FREESTREAM

Of significant interest is the inclusion of transonic flow effects in the calculation of oscillating air forces where the freestream flow is slightly supersonic. Of particular interest to the current work is whether or not the relaxation solutions become unstable in the same fashion when the freestream is supersonic as when it is subsonic.

The differential and finite difference equations are the same for both the subsonic and supersonic freestream cases. The flow characteristics are sketched in figure 19, which shows the boundary conditions that were used in a pilot two-dimensional program. The unsteady velocity potential at the upstream boundary is set to zero. Since the flow is supersonic at the downstream boundary and backward differencing is used in the

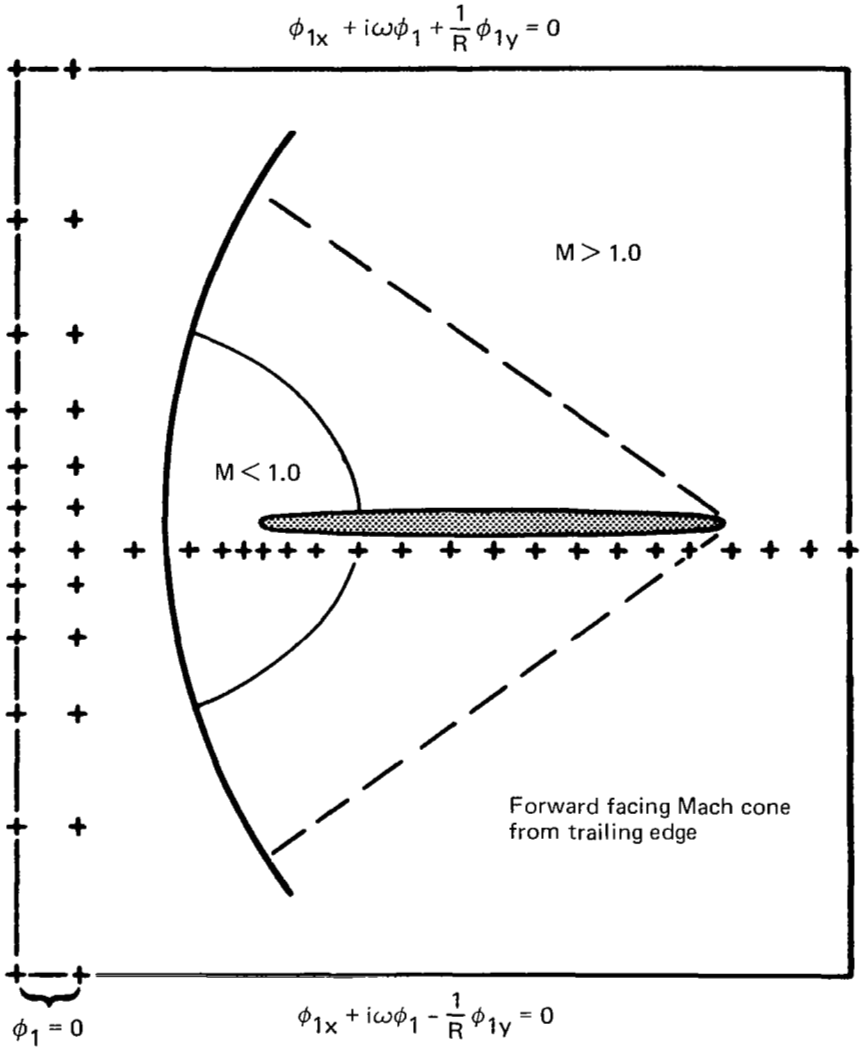

Figure 19.—Boundary Conditions for Problem With Supersonic Freestream

supersonic regions, boundary conditions need not be specified at the downstream boundary. Porous wall boundary conditions were convenient to use on the upper and lower boundaries. In practice, however, these boundaries should be set far enough out so that they do not affect the flow over the wing, and thus the pressure is independent of the porosity factor.

As discussed by Traci et al. (ref. 9), the flat plate problem in which the steady-state velocity potential is constant may be solved by a single downstream pass with the relaxation procedure since nowhere in the flow is any point affected by points in the downstream columns. The problem of mixed flow with the pocket of subsonic flow buried within the supersonic flow is quite a different matter. Traci et al. noted relaxation solution instabilities in the neighborhood of M = 1.0 and, for the supersonic case, obtained two-dimensional solutions at M = 1.10 but not at M = 1.05. A priori, one may suspect that the finite subsonic region will have properties similar to the finite mesh of the subsonic freestream case, which results in instabilities in the relaxation process.

In practice, numerical examples do not appear to admit such a simple explanation. A circular-arc airfoil was analyzed at two Mach numbers, M = 1.05 and 1.15. A simple pitching oscillation was studied. Some of our results have the characteristics of converging for a number of iterations and then diverging. Here the maximum difference between φ_1 for successive iterations was used as a measure of convergence. If the convergence criteria were met before the divergence started, one would assume that one had obtained a valid solution. Under these circumstances, the use of overrelaxation factors (ORF) and underrelaxation factors (URF) other than unity increased the tendency for divergence. Hence, the calculations were run with ORF = URF = 1.0. The net result was that M = 1.15, with a relatively small subsonic region, the convergence characteristics were improved by raising the reduced frequency. At M = 1.05 with the attendant large subsonic region about the airfoil leading edge, convergence was improved by decreasing the reduced frequency. This latter behavior is what would be expected from experience with the subsonic freestream problem.

These examples were rerun using the shock point operator of appendix C. Use of the operator noticeably improved the convergence characteristics at both Mach numbers but did not eliminate the relaxation solution instabilities.

A summary of convergence experience with the supersonic freestream is given in table 3. The table includes runs both with and without the shock point operator and includes a general description of where the maximum ERROR occurred for both converging and diverging examples. Since these calculations have been made with a limited number of variations in parameters such as the location of farfield boundaries, the number and spacing of mesh points, and the location of mesh points with respect to the sonic lines and subsonic regions, it is felt that firm conclusions are, as yet, unwarranted.

There appear to be stability problems with the relaxation process in the supersonic freestream problem as well as with the subsonic problem. We suspect both have the same origins; that is, the eigen characteristics of the problem. However, numerical examples with the supersonic freestream problem do not give consistent convergence divergence behavior at M = 1.05 and M = 1.15. It is assumed that a full direct solution as described previously would provide solutions, but this has not been tried.

Table 3.—Comparison of Convergence Characteristics of Supersonic Free-stream With and Without Shock Point Operator (SPO)

Reduced frequency, ω	M = 1.05		M = 1.15	
	With SPO	Without SPO	With SPO	Without SPO
0.015	Converges * Subsonic area ✡ 3.5E-4	Converges * In front of subsonic region off wing	—	—
0.03	Converges * Aft sonic line ✡ 3.4E-4	Diverges * Front sonic line	Diverges * Peak of subsonic region	Diverges * Peak of subsonic region
0.06	Diverges * Aft sonic line	Diverges * Aft sonic line	Converges * Aft of subsonic region on wing ✡ 2.0E-4	Diverges * In front of subsonic region off wing
0.12	—	—	Converges * Aft of subsonic region on wing ✡ 1.6E-4	Diverges after 35 iterations * In front of subsonic region off wing
0.24	—	—	Converges * Aft of subsonic region on wing ✡ 0.8E-4	Diverges after 40 iterations * Front sonic line

ORF = URF = 1.0

✡ Maximum error after 100 iterations

* Location of maximum error

9.0 PROPERTIES OF THE RESIDUAL

It is customary for both steady and unsteady transonic finite difference solutions to use ERROR rather than the residual as a criterion for relaxation solution convergence. ERROR is the maximum difference between successive potential distributions divided by the relaxation factor as defined in equation (9). The residual is the difference between the right-hand side and the system matrix times the current approximation when the set of equations is written $A\overline{\varphi_1}=\overline{R}$. This section summarizes a brief study of the characteristics of the residual with respect to the unsteady problem.

First, it is noted that numerical examples, which are presented in appendix D show that a residual of the same order of magnitude as ERROR may be obtained by scaling the residual value with an associated area. For the purposes of this report, the RESIDUAL at a point ij is defined as the product of the value of the difference equation by a term proportional to the local mesh area, viz.

$$\frac{(x_{i+1} - x_{i-1})(y_{j+1} - y_{j-1})}{4}$$

It is shown in appendix D that RESIDUAL may be interpreted as the excess (or deficit) of the mass flux within each mesh in the flow field. Since for an exact solution of the difference equation, this should be zero, it is also a measure of how close the relaxation solution is to being converged.

It can be shown that RESIDUAL and ERROR curves, when plotted on an iteration history curve, should be essentially parallel to each other. A mathematical explanation of this phenomenon is also presented in Appendix D along with numerical examples for illustration purposes.

Generally, it is not convenient to use the residual (or, for that matter, RESIDUAL) as a convergence test since evaluation requires a separate pass after all the velocity potentials have been updated.

10.0 AEROELASTIC ANALYSES

Calculating air forces for flutter analyses can become very expensive when using the more complex aerodynamic procedures such as the method of this report. This is due to forces being functions not only of Mach number (as for steady-state analyses) but also of reduced frequency and due to the need to calculate pressures for a set of modes (generalized coordinates), which may number from 10 to 20 or more for low-aspect-ratio configurations. Also, flutter analyses are often required for small perturbations in mass and/or stiffness distributions from the basic configuration and, in general, this means recalculation of the generalized air force matrix. The question arises as to how the recalculations of the air force matrix can be handled most efficiently with respect to the procedures of this report for unsteady transonic flow.

It is first noted that the basic differential equations are linear with spatial varying coefficients. The resulting air forces are thus superposable and may be directly used in conventional flutter analysis formulation.

Next, the two kinds of numerical solutions to the finite difference equations that have been discussed are the line relaxation procedure and full direct solution. The former, which permits the solution to be calculated in sequences, is preferred because of the large number of finite difference points (and thus the large number of equations) even for two-dimensional problems. Indeed, it may well represent the only practical solution method for three-dimensional analyses. However, line relaxation does have instability problems for larger values of λ_1. It was concluded in section 5 that for combinations of Mach number and reduced frequency where relaxation solutions are unstable, the most feasible method is the full direct solution. In matrix form, both of these procedures are written as

$$\underset{mxm}{[A\,(M,\,\omega)]}\ \underset{mx1}{\{\varphi_1\}} = \underset{mx1}{\{R\}} \tag{20}$$

It is assumed that outgoing wave boundary conditions are used on the far-field boundaries so that $\{R\}$ does not depend on φ_1's. Also, the matrix sizes have been indicated above the equation. Here, m is the total number of finite difference points interior to the outer boundaries. The matrix $\{R\}$ is a function of surface deformation (the mode shape) so that equation (20) may be rewritten as

$$\underset{mxm}{[A\,(M,\,\omega)]}\underset{mx1}{\left\{\varphi_1^{(s)}\right\}} = \underset{mxn}{[T_{DW}\,(\omega)]}\underset{nx1}{\left\{f^{(s)}\right\}} \tag{21}$$

The matrix $[T_{DW}(\omega)]$ calculates the boundary conditions on the right-hand side from the modal matrix $\left\{f_1^{(s)}\right\}$. Here, n is the number of aerodynamic control points on the airfoil or wing and the superscript s denotes the mode shape. The size of n is expected to be on the order of 40 for the two-dimensional problem and on the order of 300 for the three-dimensional problem.

With respect to the direct solution, it is easy to conceive of an influence coefficient matrix that would be independent of structural characteristics; that is, a matrix which when postmultiplied by a modal matrix and premultiplied by its transpose would provide a set of generalized air forces directly. For example, equation (21) may be rewritten as

$$\underset{mx1}{\left\{\varphi_1^{(s)}\right\}} = \underset{mxm}{[A\,(M,\,\omega]^{-1}}\ \underset{mxn}{[T_{DW}\,(\omega)]}\underset{nx1}{\left\{f^{(s)}\right\}} \tag{22}$$

The pressure is obtained by operating on the φ_1's,

$$\underset{nx1}{\left\{\Delta p^{(s)}\right\}} = \underset{nxm}{[T_p]}\ \underset{mxm}{[A\,(M,\,\omega]^{-1}}\ \underset{mxn}{[T_{DW}\,(\omega)]}\underset{nx1}{\left\{f^{(s)}\right\}} \tag{23}$$

The transformation matrix $[T_p]$ transforms the velocity potential to the pressure distribution, and the generalized air force Q_{rs} is found from

$$Q_{rs} = \underset{1xn}{\left[f^{(r)}\right]}\ \underset{nxn}{[T_I]}\underset{nx1}{\left\{\Delta p^{(s)}\right\}} \tag{24}$$

where the matrix $[T_I]$ performs the necessary integration of the product of the pressure due to mode s times the r^{th} mode shape. Substituting equation (23) in equation (24), we have

$$Q_{rs} = \underset{1xn}{\left[f^{(r)}\right]}\left(\underset{nxn}{[T_I]\ [T_p]\ [A\,(M,\,\omega)]^{-1}\ [T_{DW}\,(\omega)]}\right)\underset{nx1}{\left\{f^{(s)}\right\}} \tag{25}$$

and the matrix product enclosed by the parentheses is just what is desired and is a complex matrix of order nxn. This represents a very manageable matrix in terms of size and number of operations to obtain Q_{rs}.

However, the critical problem is the size and banding characteristics of the matrix $[A(M,\omega)]$. For example, for practical two-dimensional problems, m will be approximately 1000 to 2000 and for practical three-dimensional problems it will be approximately 25 000 to 50 000. Also, $[A(M,\omega)]$ is complex, which essentially doubles its storage requirements. Here significant advantage can often be taken of the special case of flow symmetry with respect to the plane of the wing. While this may result in a two-dimensional problem of manageable size, it does not appear to do the same for the three-dimensional problem. An important characteristic of $[A(M,\omega)]$ is that it is banded; therefore, both $[A(M,\omega)]$ and its LU decomposition form can be stored in significantly less space than the complete matrix. Thus, in practice, the inverse of $[A]$, which would be a dense matrix, is not calculated. The unknowns that are found are the φ_1's of equation (21) or (22), and the solution is found from the LU decomposition by back substitution.

The authors are not familiar with the capabilities of the current generation of STAR machines or plans for the next generation. It may be that the increased capability of these machines could solve the problem as posed. Also, the capabilities of sparse matrix routines have not been thoroughly investigated. It would appear feasible, however, to actually obtain the inverse of $[A(M,\omega)]$ for two-dimensional problems of practical size but not for three-dimensional problems.

The alternative would be to calculate the transonic air forces in terms of a limited set of reference modes. Then as the mass and/or stiffness distributions of the basic structure are changed, the new natural modes of the modified system would be found as a superposition of the reference modes. In the same fashion, the generalized air forces for the modified system would be obtained as a superposition of the air forces for the reference modes. These reference modes would usually be the natural modes of the basic configuration.

The generalized forces for the reference modes (or any other set of modes), if the inverse of $[A]$ is not available, would be calculated from a sequence starting with the solution for $\{\varphi_1\}$ in equation (21) using LU decomposition. It is noted that LU decomposition is done once and the results are stored so that obtaining $\{\varphi_1\}$ for new modes is relatively efficient. The column of generalized forces is then found from the matrix triple product

$$\underset{rx1}{\{Q_s\}} = \underset{rxn}{[f]^T} \left(\underset{nxn}{[T_I]} \; \underset{nx4n}{[T_p]} \right) \underset{4nx1}{\{\overline{\varphi}_1^{(s)}\}}$$

The $\{\varphi_1^{(s)}\}$ is a subset of the full $\{\varphi_1\}$ matrix from the solution of equation (21). The matrix product enclosed in the parentheses may be calculated once and stored for future use. The integer r is equal to the number of reference modes used, which would be expected to be approximately 20 or 30. Generally, it appears that obtaining the φ_1's for additional reference modes will take less time than was required to do the LU decomposition.

11.0 CONCLUSIONS

This report has further explored a particular finite difference formulation for analyzing unsteady transonic flow over harmonically oscillating wings. The preferred numerical solution process of line relaxation has proved unstable for ranges of Mach number (both subsonic and supersonic) and reduced frequency of direct interest in flutter analyses. Although no means were found for extending the range using relaxation procedures, a direct solution of the complete finite difference mesh was shown to produce solutions at subsonic Mach numbers outside the range of solution convergence for the relaxation process. It is surmised that the direct solution could also be applied to flows with a supersonic freestream Mach number as well.

Because of limited computer capacity, the direct solutions obtained were for a coarse mesh, and accuracy was observed to decrease with frequency. The means for improving the accuracy of the direct solution are indicated by a study of a similar one-dimensional problem for which exact, analytic solutions were readily obtainable for comparison with the solutions from the finite difference analysis. The accuracy of the finite difference procedure was found to be proportional to $h^2\lambda_1^3$ so that the mesh spacing must be varied inversely to the 3/2 power of frequency if accuracy is to be retained. For the higher values of reduced frequency at values of Mach number close to 1, this will mean working with very large sets of finite difference points. How the use of nonuniform mesh spacing will affect this conclusion has not been examined.

In addition to the general error level, large excursions in error are caused by the presence of real eigenvalues associated with the mesh region and the far-field boundary conditions. These excursions can be supressed in the one-dimensional examples by proper selection of boundary conditions that result in the replacement of the real eigenvalues by complex eigenvalues. Since these boundary conditions are in the nature of outgoing waves, it is assumed this can be done in the two- and three-dimensional analyses also.

The three-dimensional program developed in reference 5 was extended to analyze wings with swept leading and trailing edges, and solutions for both a moderate-aspect-ratio rectangular wing and a low-aspect-ratio, clipped delta wing are presented. The pressure distributions appear reasonable although, as yet, no experimental results are available for correlation.

A conservative shock point operator has been derived for use in two- and three-dimensional analyses. In the rectangular wing analyses, use of this operator significantly increases the effect of the shock on the unsteady pressure distributions and smooths the spanwise distribution of pressure. In relaxation calculations for a supersonic freestream, use of the shock point operator extends the range of convergence but does not remove the relaxation instabilities.

Boeing Commercial Airplane Company
P.O. Box 3707
Seattle, Washington 98124
November 1977

APPENDIX A

ONE-DIMENSIONAL PROBLEM

A.1 PROBLEM STATEMENT

To gain insight into the accuracy obtainable by using direct solution methods as well as the relaxation solution stability problem, a one-dimensional version of the flat-plate small perturbation equation was investigated. This equation, which is obtained simply by dropping the φ_{1yy} term from the two-dimensional equation, is

$$K\varphi_{1_{xx}} - \frac{2i\omega}{\epsilon}\varphi_{1_x} + \frac{\omega^2}{\epsilon}\varphi_1 = 0, \quad \omega > 0$$

or, dividing by K and using $\epsilon K = (1 - M^2)/M^2$

$$\varphi_{1_{xx}} - 2i\lambda_1 M\varphi_{1_x} + \lambda_1{}^2(1 - M^2)\varphi_1 = 0 \tag{A-1}$$

where $\lambda_1 = \omega M/(1 - M^2)$. The problem then was the solution of equation (A-1) for $\varphi_1(x)$ on an interval x = a to x = b with specified types of boundary conditions; i.e., a two-point boundary value problem.

The problem was numerically solved by discretizing the derivatives with second-order approximations on a uniform mesh, as the two-and three-dimensional cases in reference 5 were solved. The numerical problem thus becomes one of solving a linear system of the form $A\overline{\varphi_1} = B$, where A is a tridiagonal matrix and B depends on the boundary conditions. The solution was obtained with the tridiagonal solver used for each row of the two-dimensional row relaxation solution.

A.2 ANALYTICAL RESULTS

The advantage of experimentation on such a simplified problem is that analytic results are readily available for comparison with numerical calculations to obtain accuracy information.

To begin, we observe that the general solution of equation (A-1) is given by

$$\varphi_1(x) = C_1 e^{i\lambda_1(1+M)x} + C_2 e^{-i\lambda_1(1-M)x} \tag{A-2}$$

where C_1 and C_2 are independent of x and are to be determined by the boundary conditions. We note that in general φ_1 contains components of substantially different wavelengths, in fact in the ratio $(1 + M)/(1 - M) = 19/1$ for $M = 0.9$. Since approximation of the shorter wavelength component is less accurate for a given number

of mesh points than the longer wavelength component, we would expect the error to be larger when C_1 is such that this component is significant, regardless of the value of λ_1. This was indeed found. (See fig. 4.) Since C_1 and C_2 are determined by the boundary conditions, we turn next to consideration of these. In their most general form, these are

$$\begin{aligned} \alpha_1 \varphi_{1_x} + \beta_1 \varphi_1 &= \gamma_1 \quad \text{at} \quad x = a \\ \alpha_2 \varphi_{1_x} + \beta_2 \varphi_1 &= \gamma_2 \quad \text{at} \quad x = b \end{aligned} \tag{A-3}$$

where the α_i, β_i, and γ_i are independent of x. Special cases of these conditions include Dirichlet ($\alpha_1 = \alpha_2 = 0, \beta_1 = \beta_2 = 1$), Neumann ($\alpha_1 = \alpha_2 = 1, \beta_1 = \beta_2 = 0$), and the third kind ($\alpha_1 = \alpha_2 = 1, \beta_1 \neq 0, \beta_2 \neq 0$).

Since C_1 and C_2 are determined from the boundary conditions, the choice of the constants in equation (A-3) will clearly affect the accuracy of the solution. There is a less obvious way in which the choice of these constants affects the accuracy: certain choices will lead to nonuniqueness of the solution, which is reflected as large increases in the error for certain reduced frequencies. To be more precise, for certain choices of α_1, β_1, α_2, and β_2, there are values of λ_1 (eigenvalues) for which nonzero solutions (eigenfunctions) to equation (A-1) with $\gamma_1 = \gamma_2 = 0$ in equation (A-3) will exist. Information is easily obtained as to the values of the α and β constants in equation (A-3) for which real eigenvalues exist. Substitution of the general solution equation (A-2) into (A-3) with $\gamma_1 = \gamma_2 = 0$ yields a 2 by 2 linear system for C_1 and C_2. In order for this homogenous system to have a nontrivial solution (i.e., for eigenfunctions to exist), it is necessary that the coefficient matrix be singular (i.e., have a 0 determinant).

When the substitution is made and the determinant set equal to 0, one obtains, after some simplification, the relation:

$$\begin{aligned} &[\lambda_1 (\alpha_1\beta_2 - \alpha_2\beta_1)] \cos \lambda_1 (b - a) \\ &- \left\{ [\alpha_1\alpha_2\lambda_1{}^2 (1 - M^2) + \beta_1\beta_2] + i\lambda_1 M (\alpha_1\beta_2 + \alpha_2\beta_1) \right\} \sin \lambda_1 (b - a) = 0 \end{aligned} \tag{A-4}$$

Note that if either the coefficient of the cosine term or the sine term is 0, then real values of λ_1 exist for which equation (A-4) will be satisfied; for example,

$$\lambda_1 = \frac{m\pi}{b - a}, \quad m = 1,2, \ldots\ldots \tag{A-5}$$

This will clearly be the case for Dirichlet ($\alpha_1 = \alpha_2 = 0, \beta_1 = \beta_2 = 1$) and Neumann ($\alpha_1 = \alpha_2 = 1, \beta_1 = \beta_2 = 0$) boundary conditions, since the coefficient of the cosine term is then 0. The same is true for boundary conditions of the third kind ($\alpha_1 = \alpha_2 = 1$) when $\beta_1 = \beta_2$.)

There are other values of the α's and β's which lead to real eigenvalues; for example, values such that the coefficients of both the sine and cosine terms are real or pure

imaginary. Of more interest, however, are values such that equation (A-4) cannot be satisfied by real λ_1 . Such values can easily be obtained using *mixed* boundary conditions. For example, specifying φ_1 at x = a and $\varphi_{1x} + i\omega(1 - M)\varphi_1$ at x = b implies that in equation (A-3) $\alpha_1 = 0$, $\beta_1 = 1$, $\alpha_2 = 1$, and $\beta_2 = i\lambda_1(1 - M)$. Substituting these values into equation (A-4), we find that this equation becomes

$$-\lambda_1 e^{i\lambda_1(b-a)} \neq 0$$

which cannot be satisfied for real $\lambda_1 \neq 0$. Thus these boundary conditions do not permit real eigenvalues. Similarly specifying $\varphi_{1x} - i\lambda_1(1 + M)\varphi_1$ at x = a and φ_1 at x = b implies $\alpha_1 = 1$, $\beta_1 = -i\lambda_1(1 + M)$, $\alpha_2 = 0$, and $\beta_2 = 1$, which when substituted into equation (A-4) yields the equation

$$\lambda_1 e^{i\lambda_1(b-a)} = 0$$

which cannot be satisfied for real $\lambda_1 \neq 0$. Thus again the boundary conditions do not permit real eigenvalues. The difference in the behavior of the error for real and complex eigenvalues is illustrated in figure 5.

Some idea of the error introduced by discretization of the analytical problem may, at least in the case of Dirichlet boundary conditions, be gained from the literature. In ref. 18, Fischer and Usmani have shown that for the problem

$$\psi'' + \lambda_1^2 \psi = 0, \qquad x \in [a, b]$$

$$\psi(a) = \psi_a, \qquad \psi(b) = \psi_b$$

when ψ'' is replaced by the usual second-order finite difference approximation on a uniform grid of spacing h, the maximum absolute error, E_{max}, satisfied $E_{max} < E_1$, where

$$E_1 = h^4 m_4 N/[12 \sin\theta \cdot |\sin(N + 1)\theta|]$$

where

$$m_4 = \max_{x \in [a, b]} \left| \psi^{(IV)}(x) \right| , \qquad \cos\theta = 1 - \frac{1}{2} h^2 \lambda_1^2$$

$$h = \frac{b - a}{N + 1}$$

When $h\lambda_1$ is small, we have $\theta \sim h\lambda_1$, and

$$E_1 \sim h^2 m_4 (b - a)/[12\lambda_1 \sqrt{1 - \frac{1}{4} h^2 \lambda_1^2} \cdot |\sin \lambda_1 (b - a)|]$$

Since $\psi = D_1 \sin \lambda_1 x + D_2 \cos \lambda_1 x$, we have $m_4 = D\lambda_1^4$ for some constant D, so that E_1 behaves like $Eh^2\lambda_1^3/|\sin \lambda_1(b - a)|$, with E some constant.

Now since equation (A-1) for φ_1 may be transformed into $\psi'' + \lambda_1^2\psi = 0$ by the nonsingular transformation $\varphi_1 = \psi\epsilon^{i\lambda 1,^{mx}}$ it is not unreasonable to expect the error in the numerical solution of the discretized version of the φ_1 problem, and this in fact was found to be the case. (See fig. 6.)

The results and conclusions from this analysis are presented in section 5.1.

APPENDIX B

EVALUATION OF FAR-FIELD WAKE INTEGRAL FOR AN ARBITRARY WING

We consider the evaluation of the field wake integral given in equation (B-1) of reference 5, namely,

$$\varphi_{1_w}(x_1,y_1,z_1) = \frac{1}{4\pi} \int_{-y_t}^{+y_t} e^{i\omega x_t(y_1')} \Delta\varphi_{1_t}(y_1')dy_1' \cdot \int_{x_t(y_1')}^{\infty} e^{-i\omega x_1'} \frac{\partial\psi}{\partial z_1}(x_1 - x_1', y_1 - y_1', z_1 - z_1')dx_1' \qquad \text{(B-1)}$$

where the partial derivative is to be evaluated at

$$\psi = e^{-i\lambda_1[M(x_1 - x_1') - R]}$$

and

$$R = \sqrt{(x_1 - x_1')^2 + (y_1 - y_1')^2 + z_1^2}$$

As before, the evaluation will be carried out for $x_1 = 1.0$. The trailing-edge function will be assumed to be a single-valued function of the form

$$x_{te}(y_1') = 1 + f(y_1')$$

where $f(y_1') \geq 0$ for $-y_t \leq y_t' \leq y_t$, but is otherwise arbitrary. For the rectangular wing, for example, $f(y_1') \equiv 0$, while for the swept wing with straight trailing edge, $f(y_1') = a \cdot |y_1'|$, where a is the tangent of the sweep angle. A more general example is given in figure (B-1).

Equation (B-1), after taking $e^{i\omega \cdot 1.0}$ into the x_1'-integral, becomes

$$\varphi_{1_w}(1, y_1, z_1) = \frac{1}{4\pi} \int_{-y_t}^{+y_t} e^{i\omega f(y_1')} \Delta\varphi_{1_{te}}(y_1')dy_1' \cdot \int_{x_1'=1+f(y_1')}^{\infty} e^{-i\omega(x_1'-1)} \frac{\partial\psi}{\partial z_1}(1 - x_1', y_1 - y_1', z_1 - z_1')dx_1' \qquad \text{(B-2)}$$

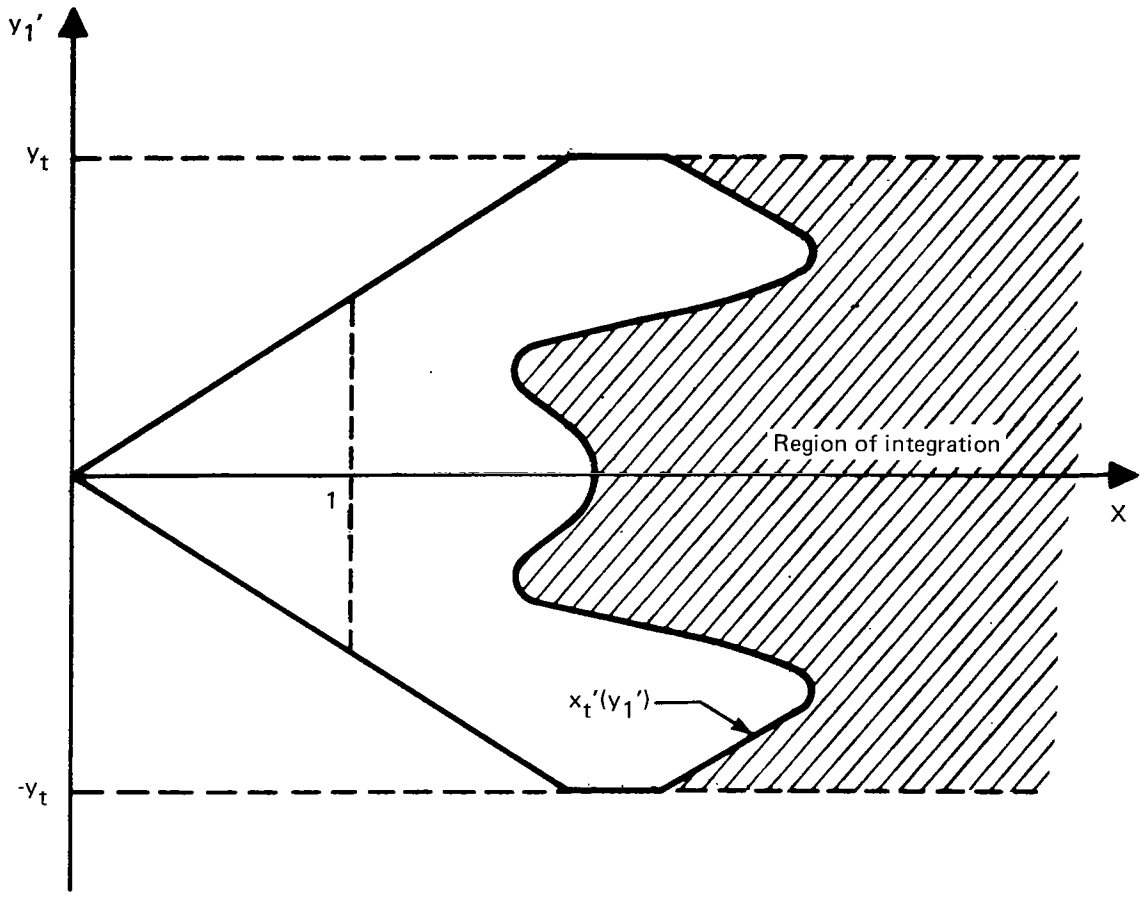

Figure B-1. — Geometry for Wake Integral Evaluation

Let I_w be the inner, x_1'-integral

$$I_w = \int_{x_1'=f(y_1')}^{\infty} e^{-i\omega(x_1'-1)} \frac{\partial \psi}{\partial z_1'}(1 - x_1', y_1 - y_1', z_1 - z_1')dx_1' \tag{B-3}$$

setting $\rho = x_1' - 1$ and inserting the expression for ψ yields

$$I_w = \int_{f(y_1')}^{\infty} e^{-i\omega\rho} \frac{\partial}{\partial z_1'} \frac{e^{-i\lambda_1(R_1+M\rho)}}{R_1} d\rho \tag{B-4}$$

with

$$R_1 = \sqrt{\rho^2 + R_0^2} \quad \text{and} \quad R_0^2 = (y_1 - y_1')^2 + (z_1 - z_1')^2$$

Taking the $\partial/\partial z_1'$ outside and combining the exponentials, we obtain

$$I_w = \frac{\partial}{\partial z_1'} \int_{f(y_1')}^{\infty} \frac{e^{-i\frac{\lambda_1}{M} MR_1 + \frac{M(\omega + \lambda_1 M)}{\lambda_1}\rho}}{R_1} d\rho \tag{B-5}$$

or since

$$\frac{M(\omega + \lambda_1 M)}{\lambda_1} = \frac{M\left(\omega + \frac{\omega M^2}{1-M^2}\right)}{\omega M/(1 - M^2)} = 1 \tag{B-6}$$

$$I_w = \frac{\partial}{\partial z_1} \int_{f(y_1')}^{\infty} \frac{e^{-i\frac{\lambda_1}{M}(MR_1 + \rho)}}{R_1} d\rho \tag{B-7}$$

Next, let

$$u = \frac{MR_1 + \rho}{\beta R_0} \tag{B-8}$$

When

$$\rho = f(y_1'), \quad u = \frac{M\sqrt{f^2(y_1') + R_0^2} + f(y_1')}{\beta R_0} \equiv u_1 \tag{B-9}$$

and as

$$\rho \to \infty \qquad u \to \infty$$

Further

$$\sqrt{1+u^2} = \frac{1}{\beta R_0}\left[\beta^2 R_0{}^2 + M^2(\rho^2 + R_0{}^2) + 2MR_1\rho + \rho^2\right]^{1/2} \tag{B-10}$$

which becomes, using $\beta^2 = 1\text{-}M^2$

$$\begin{aligned}\sqrt{1+u^2} &= \frac{1}{\beta R_0}\left[R_0{}^2 + \rho^2 + 2MR_1\rho + M^2\rho^2\right]^{1/2} \\ &= \frac{1}{\beta R_0}\left[R_1{}^2 + 2MR_1\rho + M^2\rho^2\right]^{1/2} = \frac{R_1 + M\rho}{\beta R_0}\end{aligned} \tag{B-11}$$

and

$$\frac{du}{d\rho} = \frac{1}{\beta R_0}\left[M\rho/R_1 + 1\right] = \frac{1}{R_1}\cdot\frac{R_1 + M\rho}{\beta R_0} = \frac{\sqrt{1+u^2}}{R_1} \tag{B-12}$$

so

$$I_w = \frac{\partial}{\partial z_1'}\int_{u_1}^{\infty} \frac{e^{-i\frac{\lambda_1\beta R_0}{M}u}}{\sqrt{1+u^2}}du \tag{B-13}$$

Now, let $u = \nu + u_1$ so that

$$I_w = \frac{\partial}{\partial z_1'}\int_0^{\infty} \frac{e^{-i\frac{\lambda_1\beta R_0}{M}(\nu+u_1)}}{\sqrt{1+(\nu+u_1)^2}}d\nu \tag{B-14}$$

The singularities of the integrand are where

$$1+(\nu+u_1)^2 = 0 \tag{B-15}$$

or

$$\nu = -u_1 \pm i$$

Now from equation (B-9) and the assumption that $f(y_1') \geq 0$, it follows that $u_1 > 0$, so the singularities are in the left half of the complex plane. Thus, applying Cauchy's theorem to the contour integral

$$I_{w_c} = \int_c \frac{e^{-i\frac{\lambda_1\beta R_0}{M}(\nu+u_1)}}{\sqrt{1+(\nu+u_1)^2}}d\nu \tag{B-16}$$

where the contour is shown in the following sketch

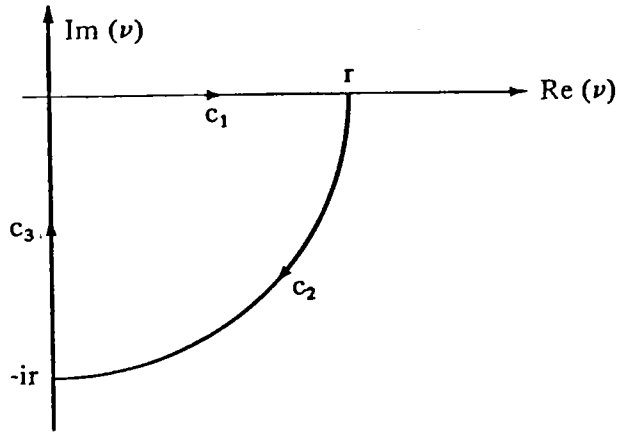

Then, $c = c_1 + c_2 + c_3$ and

$$I_{w_c} = I_{w_{c_1}} + I_{w_{c_2}} + I_{w_{c_3}} = 0 \tag{B-17}$$

and

$$I_w = \lim_{r\to\infty} \frac{\partial}{\partial z_1}, I_{c_1} = \lim_{r\to\infty} \left[-\frac{\partial}{\partial z_1}, I_{c_2} - \frac{\partial}{\partial z_1}, I_{c_3} \right] \tag{B-18}$$

As $r\to\infty$, then integral $I_{wc_2}\to 0$. On the contour C_2, $\nu = re^{-i\theta}$ $0\leq\theta\leq\pi/2$,

and $$I_{w_{c_2}} = -ire^{-i\lambda_1\beta R_0(u_1/M)} \int_0^{\pi/2} \frac{e^{-i\lambda_1\beta(R_0/M)r\exp(-i\theta)}\, e^{-i\theta}}{\sqrt{1+(r\exp(-i\theta)+u_1)^2}}\, d\theta$$

For r sufficiently large, the denominator of the integrand is $\geq r/2$.

$$|I_{w_{c_2}}| \leq 2\int_0^{\pi/2} e^{-\lambda_1\beta(R_0/M)r\sin\theta}\, d\theta$$

$$\leq 2\int_0^{\pi/2} e^{-(2/\pi)\lambda_1(R_0/M)-r\theta}\, d\theta$$

$$= \frac{\pi M}{\lambda_1\beta R_0 r}\left[1 - e^{-\lambda_1\beta R_0(r/M)}\right] \to 0 \text{ as } r\to\infty$$

Thus, we have

$$I_w = - \lim_{r \to \infty} \frac{\partial}{\partial z_1'} I_{w_{c_3}} \tag{B-19}$$

On $c_3, \nu = i\eta$ and $d\nu = id\eta$ so that

$$I_{w_{c_3}} = i \int_{-r}^{0} \frac{e^{-i\frac{\lambda_1 \beta R_0}{M}(i\eta + u_1)}}{\sqrt{1 + (i\eta + u_1)^2}} d\eta \tag{B-20}$$

or letting $\eta = -\eta$

$$I_{w_{c_3}} = i \int_{0}^{r} \frac{e^{-i\frac{\lambda_1 \beta R_0}{M}(u_1 - i\eta)}}{\sqrt{1 + (u_1 - i\eta)^2}} d\eta \tag{B-21}$$

The next step is to find the partial derivative in equation (B-19). We note from equation (B-9) that u_1 is a function of R_0 and therefore of z_1' and thus we must also differentiate u_1. It appears simplest to move the u_1 dependence to the limits before differentiating. Letting $\mu = u_1 - i\eta$, then $d\mu = id\eta$, or $d\mu = -id\eta$, and when $\eta = 0$, $\mu = u_1$; when $\eta = r$, $\mu = u_1 - ir$, so,

$$I_{w_{c_3}} = - \int_{u_1}^{u_1 - ir} \frac{e^{-i\lambda_1 \beta R_0 (\mu/M)}}{\sqrt{1 + \mu^2}} d\mu$$

$$\frac{d}{dz_1'} I_{w_{c_3}} = \left\{ - \left(\frac{\partial u_1}{\partial z_1'} \right) \left[\frac{e^{-i\lambda_1 \beta (u_1 - ir)/M}}{\sqrt{1 + (u_1 - ir)^2}} - \frac{e^{-i\lambda_1 \beta R_0 u_1/M}}{\sqrt{1 + u_1^2}} \right] \right.$$

$$\left. + \int_{u_1}^{u_1 - ir} \frac{\partial}{\partial z_1'} \frac{e^{-i\lambda_1 \beta R_0 \mu/M}}{\sqrt{1 + \mu^2}} d\mu \right\} \tag{B-22}$$

Performing the differentiation, the integral becomes

$$\int_{u_1}^{u_1 - ir} - i\lambda_1 \beta (\mu/M) \frac{e^{-i\lambda_1 \beta R_0 \mu/M}}{\sqrt{1 + \mu^2}} d\mu \cdot \frac{\partial R_0}{\partial z_1'}$$

or, transforming back to η

$$- i \int_{0}^{r} \frac{- i\lambda_1 \beta \left[(u_1 - i\eta)/M \right] e^{-i\lambda_1 \beta R_0 (u_1 - i\eta)/M}}{\sqrt{1 + (u_1 - i\eta)^2}} d\eta \cdot \frac{\partial R_0}{\partial z_1'}$$

or

$$-\frac{\lambda_1\beta}{M}\, e^{-i\lambda_1\beta R_0 u_1/M} \int_0^r \frac{u_1 - i\eta}{\sqrt{1+(u_1-i\eta)^2}}\, e^{-\lambda_1\beta R_0\eta/M}\, d\eta \cdot \frac{\partial R_0}{\partial z_1'} \qquad \text{(B-23)}$$

Substituting equation (B-23) into equation (B-22) and taking the limit as $r \to \infty$, we have

$$\frac{d}{dz_1'}\, I_{w_{c_3}} = e^{-i\lambda_1\beta R_0 u_1/M}\left[\frac{1}{\sqrt{1+u_1^2}}\left(\frac{du_1}{dz_1'}\right)\right.$$

$$\left. + \frac{\lambda_1\beta}{M}\int_0^\infty \frac{u_1 - i\eta}{\sqrt{1+(u_1-i\eta)^2}}\, e^{-\lambda_1\beta R_0\eta/M}\, d\eta \cdot \frac{dR_0}{dz_1'}\right] \qquad \text{(B-24)}$$

Let $\overset{\Delta}{I}_w$ be the integral in equation (B-24). Integrating by parts with

$$u = e^{-\lambda_1\beta R_0\eta/M} \qquad dv = \frac{u_1 - i\eta}{\sqrt{1+(u_1-i\eta)^2}}$$

then

$$du = -\lambda_1\beta(R_0/M)\, e^{-\lambda_1\beta R_0\eta/M}\, d\eta$$

and

$$v = i\sqrt{1+(u_1-i\eta)^2}$$

from which

$$\overset{\Delta}{I}_w = ie^{-\lambda_1\beta R_0\eta/M}\sqrt{1+(u_1-i\eta)^2}\,\Big|_{\eta=0}^{\eta=\infty} + \frac{i\lambda_1\beta R_0}{M}\int_0^\infty \sqrt{1+(u_1-i\eta)^2}\; e^{-\lambda_1\beta R_0\eta/M}\, d\eta$$

$$= -i\sqrt{1+u_1^2} + i\frac{\lambda_1\beta R_0}{M}\int_0^\infty \sqrt{1+(u_1-i\eta)^2}\; e^{-\lambda_1\beta R_0\eta/M}\, d\eta$$

Making the transformation $\tau = \lambda_1\beta R_0\eta/M$, we have

$$\overset{\Delta}{I}_w = -i\sqrt{1+u_1^2} + i\int_0^\infty \sqrt{1+\left[u_1 - i\frac{M}{\lambda_1\beta R_0}\tau\right]^2}\; e^{-\tau}\, d\tau$$

or

$$\overset{\Delta}{I}_w = \frac{i}{\beta}\left[-\beta\sqrt{1+u_1^2} + \int_0^\infty \sqrt{\beta^2+\left(\beta u_1 - i\frac{M}{\lambda_1 R_0}\tau\right)^2}\, e^{-\tau}\, d\tau\right] \qquad \text{(B-25)}$$

The final calculation required is that of $\partial\theta_1/\partial z_1'$. Since u_1 depends on z_1', only through R_0, $\partial u_1/\partial z_1' = (du_1/dR_0)\,(\partial R_0/\partial z_1')$.

From equation (B-9),

$$u_1 = \frac{M\sqrt{f^2(y_1') + R_0^2} + f(y_1')}{\beta R_0}$$

from which

$$\frac{du_1}{dR_0} = \frac{M}{\beta\sqrt{f(y_1')^2 + R_0^2}} - \frac{u_1}{R_0} \qquad \text{(B-26)}$$

Finally, substituting from equations (B-25) and (B-26) into equation (B-24), and using equation (B-19) and the fact that $\partial R_0/\partial z_1' = (z_1' - z_1)/R_0$, we have for $z_1' = 0$,

$$I_w = \frac{z_1 e^{-i\lambda_1 \beta \bar{R}_0 \bar{u}_1/M}}{\bar{R}_0}\left\{ \frac{1}{\sqrt{1+u_1^2}}\left(\frac{M}{\beta\sqrt{f^2(y_1') + \bar{R}_0^2}} - \frac{u_1}{R_0}\right)\right.$$

$$\left. + \frac{i\lambda_1}{M}\left[-\beta\sqrt{1+\bar{u}_1^2} + \int_0^\infty \sqrt{\beta^2 + \left(\beta\bar{u}_1 - \frac{iM}{\lambda_1 R_0}\tau\right)^2}\, e^{-\tau}\, d\tau\right]\right\} \qquad \text{(B-27)}$$

where the bars signify evaluation at $z_1' = 0$. That is,

$$\bar{R}_0 = \sqrt{(y_1 - y_1')^2 + z_1^2}$$

and

$$\bar{u}_1 = \frac{M\sqrt{f^2(y_1') + R_0^2} + f(y_1')}{\beta \bar{R}_0}$$

The integral in equation (B-27) differs only slightly from that given in reference 5 and may be evaluated by the same method, Gauss-Laguerre integration.

Thus evaluation of the far-field wake integral is reduced to using equation (B-27) in equation (B-2) with the appropriate expression for the trailing edge.

Specialization of equation (B-27) for the straight swept trailing edge is immediate, consisting only of taking $f(y_1') = a|y_1'|$ where a is the tangent of the sweep angle measured back from the y_1' axis.

A check is available by comparison with the rectangular wing case. Taking $f(y_1') = 0$, we have

$$u_1 = M/\beta \quad \text{and} \quad \sqrt{1+\bar{u}_1^2} = 1/\beta$$

so that equation (B-27) becomes

$$I_w = \frac{z_1}{\bar{R}_0} e^{-i\lambda_1 \bar{R}_0} \left\{ \frac{i\lambda_1}{M} \left[-1 + \int_0^\infty \sqrt{\beta^2 + \left(M - \frac{iM}{\lambda_1 \bar{R}_0} \tau \right)^2} \, e^{-\tau} \, d\tau \right] \right\}$$

as was previously obtained.

Acknowledgement. Calculations performed by R.W. Call toward extending the treatment in reference 5 to the case of the sweptwing with straight trailing edge have provided useful insights for the general treatment given here.

APPENDIX C

DERIVATION OF SHOCK POINT OPERATOR

When a rapidly decelerating flow is supersonic upstream of the point i, j ($u_{i-\frac{1}{2},j}<0$) and the flow becomes subsonic downstream of the point $u_{i+1/2,j}>0$), a shock wave then lies close to the point i, j. To satisfy the appropriate jump conditions across the shock, the difference operator for the point i, j must be conservative. To obtain such an operator, we apply the divergence theorem

$$\int_v \nabla \cdot \bar{F}\, dv = \int_s \bar{F} \cdot \bar{\eta}\, d_s \tag{C-1}$$

to the differential operator expressed in conservation form for the control volume consisting of lines drawn midway between consecutive columns and rows of mesh points as shown in figure C-1. Here n is the outward normal to the closed surface. We shall consider only two-dimensional flow, but the generalization to three-dimensional flow requires only the addition of the central difference operator for φ_{1zz} at the point i, j, k.

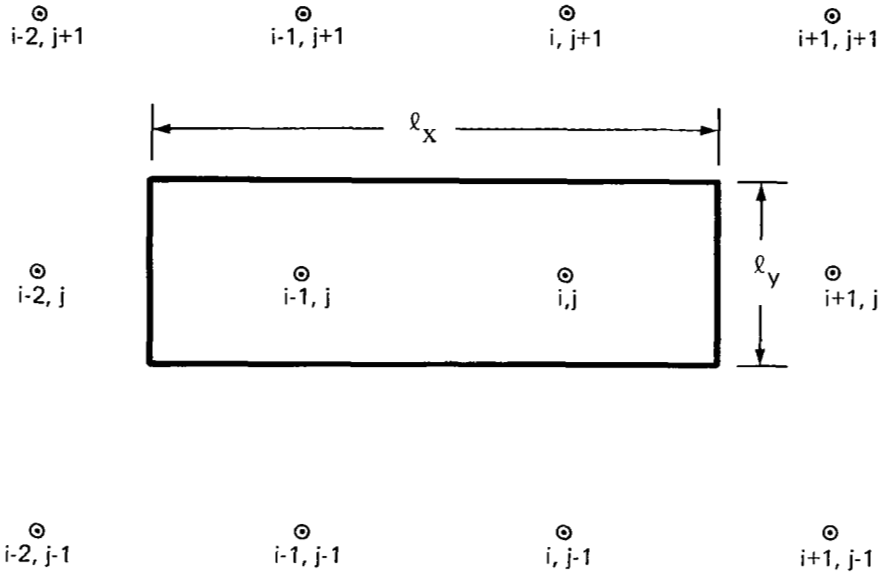

Figure C-1.—Control Volume for Shock Point Operator

The basic partial differential equation, equation (17) of Ehlers (ref. 1), has the form

$$\left(u\varphi_{1_x} - 2i\omega\varphi_1/\epsilon\right)_x + \varphi_{1_{yy}} + q\varphi_1 = 0$$

Hence, the vector $\bar{F}$ is

$$\bar{F} = u\varphi_{1_x} - 2i\omega\varphi_1/\epsilon, \qquad \varphi_{1_y}$$

and the approximate evaluation of the surface integral in equation (1) yields

$$\ell_y\left[u_{i+\frac{1}{2}j}\varphi_{x_{i+\frac{1}{2}j}} - u_{i-\frac{3}{2}j}\varphi_{x_{i-\frac{3}{2}j}} - 2i\omega\left(\varphi_{i+\frac{1}{2}j} - \varphi_{i-\frac{3}{2}j}\right)/\epsilon\right]$$

$$+ \ell_x\varphi_{y_{ij+\frac{1}{2}}} - \ell_x\varphi_{y_{ij-\frac{1}{2}}} + q_{ij}\ell_x\ell_y\varphi_{ij} = 0$$

where i+½ denotes the value of the quantity at the point midway between x_i and x_{i+1}; and similarly, for the other half integer subscripts. Dividing the equation by $\ell_x\ell_y$ puts the equation in difference form:

$$\left[u_{i+\frac{1}{2}j}\varphi_{x_{i+\frac{1}{2}j}} - u_{i-\frac{3}{2}j}\varphi_{x_{i-\frac{3}{2}j}}\right]/\ell_x - 2(i\omega/\epsilon)\left[\varphi_{i+\frac{1}{2}j} - \varphi_{i-\frac{3}{2}j}\right]/\ell_x$$

$$+\left[\varphi_{y_{ij+\frac{1}{2}}} - \varphi_{y_{ij-\frac{1}{2}}}\right]/\ell_y + q_{ij}\varphi_{ij} = 0 \qquad \text{(C-2)}$$

Now

$$\left(\varphi_{i+\frac{1}{2}j} - \varphi_{i-\frac{3}{2}j}\right)/\ell_x = \left(\varphi_{i+\frac{1}{2}j} - \varphi_{i-\frac{1}{2}j} + \varphi_{i-\frac{1}{2}j} - \varphi_{i-\frac{3}{2}j}\right)/\ell_x$$

$$= \left[\left(x_{i+\frac{1}{2}} - x_{i-\frac{1}{2}}\right)\varphi_{x_{ij}} + \left(x_{i-\frac{1}{2}} - x_{i-\frac{3}{2}}\right)\varphi_{x_{i-1j}}\right] / \left(x_{i+\frac{1}{2}} - x_{i-\frac{3}{2}}\right)$$

$$= \left[\left(x_{i+1} - x_{i-1}\right)\varphi_{x_{ij}} + \left(x_i - x_{i-2}\right)\varphi_{x_{i-1j}}\right] / \left[x_{i+1} + x_i - x_{i-1} - x_{i-2}\right]$$

We substitute the central difference operator for $\varphi_{x_{ij}}$ and upwind difference operator for $\varphi_{x_{ij}}$ and obtain

$$= DX_1\left[c_{2j}(\varphi_{ij} - \varphi_{i-1j}) - d_{1i-1}(\varphi_{i-1j} - \varphi_{i-2j})\right]/(DX_1 + DX_2)$$

$$+ DX_2\left[c_{1i}(\varphi_{i+1j} - \varphi_{ij}) + d_{1i}(\varphi_{ij} - \varphi_{i-1j})\right]/(DX_1 + DX_2) \qquad \text{(C-3)}$$

where $DX_1 = x_i - x_{i-2}$, $DX_2 = x_{i+1} - x_{i-1}$, and c_{1i}, d_{1i}, and c_{2i} are given in equations (19), (20), and (26) of reference 1.

$$\left(u_{i+\frac{1}{2}j}\varphi_{x_{i+\frac{1}{2}j}} - u_{i-\frac{3}{2}j}\varphi_{x_{i-\frac{3}{2}j}}\right)/\ell_x$$

$$= D_1\left[2c_{i-1}\,u_{i-\frac{1}{2}j}(\varphi_{ij} - \varphi_{i-1j}) - 2d_{i-1}\,u_{i-\frac{3}{2}j}(\varphi_{i-1j} - \varphi_{i-2j})\right]$$

$$+ D_2\left[2c_i u_{i+\frac{1}{2}j}(\varphi_{i+1j} - \varphi_{ij}) - 2d_i\,u_{i-\frac{1}{2}j}(\varphi_{ij} - \varphi_{i-1j})\right] \qquad \text{(C-4)}$$

with $D_1 = DX_1/(DX_1 + DX_2)$ and $D_2 \times DX_2/(DX_1 + DX_2)$. The y derivative becomes

$$\varphi_{yy_{ij}} = \left(\varphi_{y_{ij+\frac{1}{2}}} - \varphi_{y_{ij-\frac{1}{2}}}\right)/\ell_y = 2a_j\varphi_{ij-1} - 2(a_j + b_j)\,\varphi_{ij} + 2b_j\,\varphi_{ij+1} \qquad \text{(C-5)}$$

where a_j and b_j are given in equation (23) of reference 1.

Finally the difference equation at the shock point ij is obtained by substituting equations (C-3), and (C-4), and (C-5) into equation (C-2). After some simplification, we obtain

$$a_j\varphi_{ij-1} - (a_j + b_j + D_2\,E_1 + D_2E_2 - D_1E_3 - q_{ij}/2)\,\varphi_{ij} + b_j\,\varphi_{ij+1} =$$

$$(D_1E_3 + D_1E_4 - D_2E_2)\,\varphi_{i-1j} - D_1E_4\,\varphi_{i-2_j} - D_2E_1\,\varphi_{i+1j} \qquad \text{(C-6)}$$

where

$$E_1 = c_i\,u_{i+\frac{1}{2}j} - i\omega c_{1i}/\epsilon$$

$$E_2 = d_i\,u_{i-\frac{1}{2}j} + i\omega d_{1i}/\epsilon$$

$$E_3 = c_{i-1}\,u_{i-\frac{1}{2}j} - i\omega c_{2i}/\epsilon$$

$$E_4 = d_{i-1}\,u_{i-\frac{3}{2}j} - i\omega d_{1i-1}/\epsilon$$

When $D_1 = 1$ and $D_2 = 0$, the difference equation (C-6) reduces to the hyperbolic upwind difference equation; and when $D_2 = 1$ and $D_1 = 0$, it reduces to the conventional elliptic central difference equation. For equally spaced points, $D_1 = D_2 = ½$. With this value for D_1 and D_2, equation (C-6) becomes the shock point operator used by Traci, Albano, and Farr (ref. 9). When $D_1 = D_2 = 1$, we obtain the shock point operator as used by Murman (ref. 23). The present formulation as well as that of reference 9 yields a form of the differential equation consistent with that at adjacent points, whereas Murman's does not.

APPENDIX D

RESIDUAL ANALYSES

This appendix derives an interpretation of RESIDUAL as a mass flux and a mathematical explanation of the reason why the RESIDUAL and ERROR curves as plotted in a convergence history are essentially parallel. It also includes numerical examples illustrating these concepts. The differential equation that we solve for the unsteady flow potential is basically the equation for the conservation of mass at a point in the flow. This is easily seen since it results from separating the continuity equation

$$\rho_t/\rho + \nabla \cdot \nabla\varphi_1 + \nabla\varphi_1 \cdot \nabla\rho/\rho = 0$$

into steady flow and unsteady flow equations after $\nabla\rho/\rho$ is eliminated by using Bernoulli's equation (see page 35 of Ehlers, ref. 1). The differential equation for the unsteady complex potential can be expressed in the form (eq. (75) of ref. 1):

$$\nabla \cdot \bar{F} + Q\varphi_1 = 0$$

where Q does not depend upon the unsteady potential φ_1, and the factor $F = (F_1, F_2, F_3)$.

Consider now a rectangular parallelepiped of sides Δx, Δy, Δz centered about the point x,y,z. The mass produced inside the region is found by integrating the differential equation over the volume. Applying the divergence theorem to the first term of equation (19) gives us

$$\Delta y \Delta z \, [F_1(x + \Delta x/2, y, z) - F_1(x - \Delta x/2, y, z)]$$

$$+ \Delta x \Delta z \, [F_2(x, y + \Delta y/2, z) - F_2(x, y - \Delta y/2, z)]$$

$$+ \Delta y \Delta x \, [F_3(x, y, z + \Delta z/2) - F_3(x, y, z - \Delta z/2)]$$

$$+ \Delta x \Delta y \Delta z \, Q(x, y, z) \varphi_1 = 0$$

Factoring out $\Delta x \Delta y \Delta z$ yields

$$\Delta x \Delta y \Delta z \Big\{ [F_1(x + \Delta x/2, y, z) - F_1(x - \Delta x/2, y, z)]/\Delta x$$

$$+ [F_2(x, y + \Delta y/2, z) - F_2(x, y - \Delta y/2, z)]/\Delta y$$

$$+ [F_3(x, y, z + \Delta z/2) - F_3(x, y, z - \Delta z/2]/\Delta z$$

$$+ Q\varphi_1 \Big\} = 0$$

The quantity in brackets can be recognized as the difference equation which we are solving for the unsteady potential. The complete left-hand side of the previous equation, which may not be necessarily zero, is the residual as used in this report and is a measure of the excess (or deficit) of the mass flux within each mesh in the flow field. Since for an exact solution of the difference equation this residual should be zero, it is a measure of how close the relaxation solution is to being converged.

A mathematical explanation of the reason why ERROR and RESIDUAL curves should be essentially parallel is also readily available. Block (i.e., row or column) successive overrelaxation for the solution of $A\bar{\varphi}_1 = \bar{R}$ may be written in matrix notation as

$$\bar{\varphi}_1^{(m+1)} = (D + rL)^{-1} \left(-rU + (1 - r)D\right)\bar{\varphi}^{(m)} + r\,(D + rL)^{-1}\,\bar{R}$$

where D consists of the blocks on the diagonal of A; L and U consist of the blocks below and above the diagonal, respectively; and r is the relaxation factor. (The special case where A is Hermitian was discussed in ref. 5.) Replacement of U by A-D-L followed by some matrix algebra yields the equivalent form

$$\bar{\varphi}_1^{(m+1)} = \bar{\varphi}_1^{(m)} + r\,(I + rD^{-1}L)^{-1}\,D^{-1}\,(\bar{R} - A\bar{\varphi}_1^{(m)})$$

Here the last factor on the right is immediately recognizable as the vector of (unscaled) residuals. Multiplication of the residual vector by D^{-1} effectively scales the residuals by an area, similar to the scaling used in the program, since the primary components of the elements of D have the dimensions of $(\text{area})^{-1}$. Moving the first term on the right-hand side to the left, dividing by r, and taking the maximum norm of each side, we have

$$\frac{1}{r}\| \bar{\varphi}^{(m+1)} - \bar{\varphi}_1^{(m)} \| \leq \| (I + rD^{-1}L)^{-1} \| \cdot \| D^{-1}\,(\bar{R} - A\bar{\varphi}_1^{(m)}) \|$$

Now, the left-hand side is just ERROR, as previously defined, while the right-hand side is just a constant times the maximum scaled residual. When this inequality is viewed as providing an estimate of ERROR in terms of the scaled residual, it is clear that these two quantities are roughly proportional. The essentially parallel nature of the ERROR and RESIDUAL error curves on a semi-log plot in both convergent and divergent cases is thus natural and expected.

Examples of the behavior of the maximum RESIDUAL with iteration for a two-dimensional configuration are given in figures D-1 through D-7. Two different maximum RESIDUALS are shown. The first, called an "INTERMEDIATE RESIDUAL" is calculated after each line relaxation is completed. The INTERMEDIATE RESIDUAL is computed using both old and new values of the velocity potential and, if the relaxation factor is set to 1.0, it should be zero. In our calculations it is of approximately 10^{-15} for an ORF of 1. It is of interest mainly because it can be calculated with the coefficients and velocity potentials available at the end of each line relaxation calculation and thus may be obtained very efficiently. The second line shows the true maximum RESIDUAL, which is calculated in a separate pass after all velocity potentials have been updated. It includes the relaxation factor and thus reflects how well the calculated velocity potential as scaled with the relaxation factor satisfies the finite difference equation.

In figure D-1, results are presented for a flat plate example (no mixed flow) solved with row relaxation using an ORF of 1.85. As would be expected from the preceding discussion, the true RESIDUAL curve runs parallel to the ERROR curve, and in this particular case the true RESIDUAL curve lies on top of the ERROR curve. The INTERMEDIATE RESIDUAL curve lies above the other two. Figure D-2 presents the

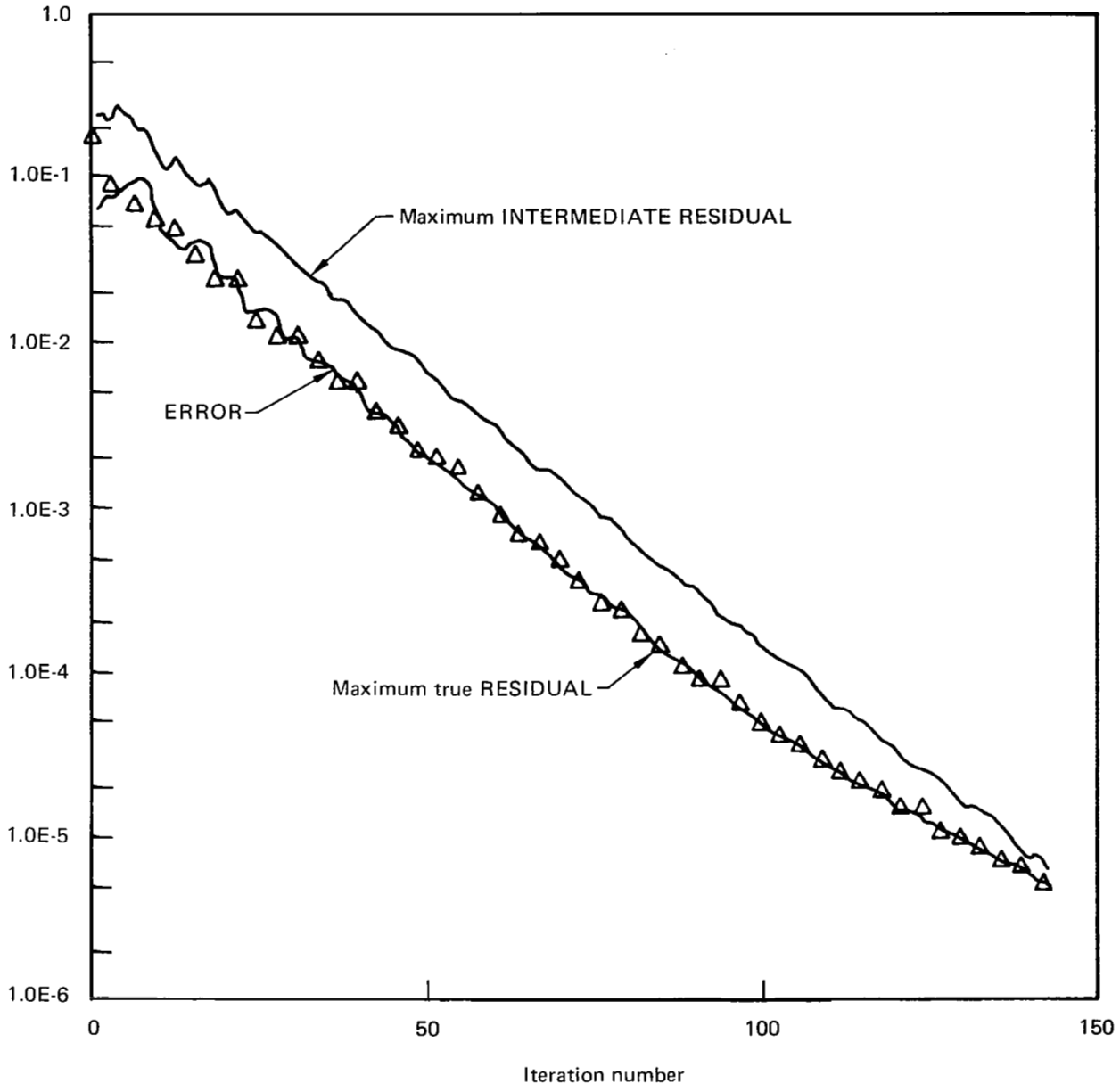

Figure D-1.—Sample ERROR and RESIDUAL Curves Versus Iteration for Row Relaxation, ORF = 1.85, M = 0.9, ω = 0.06, Flat Plate

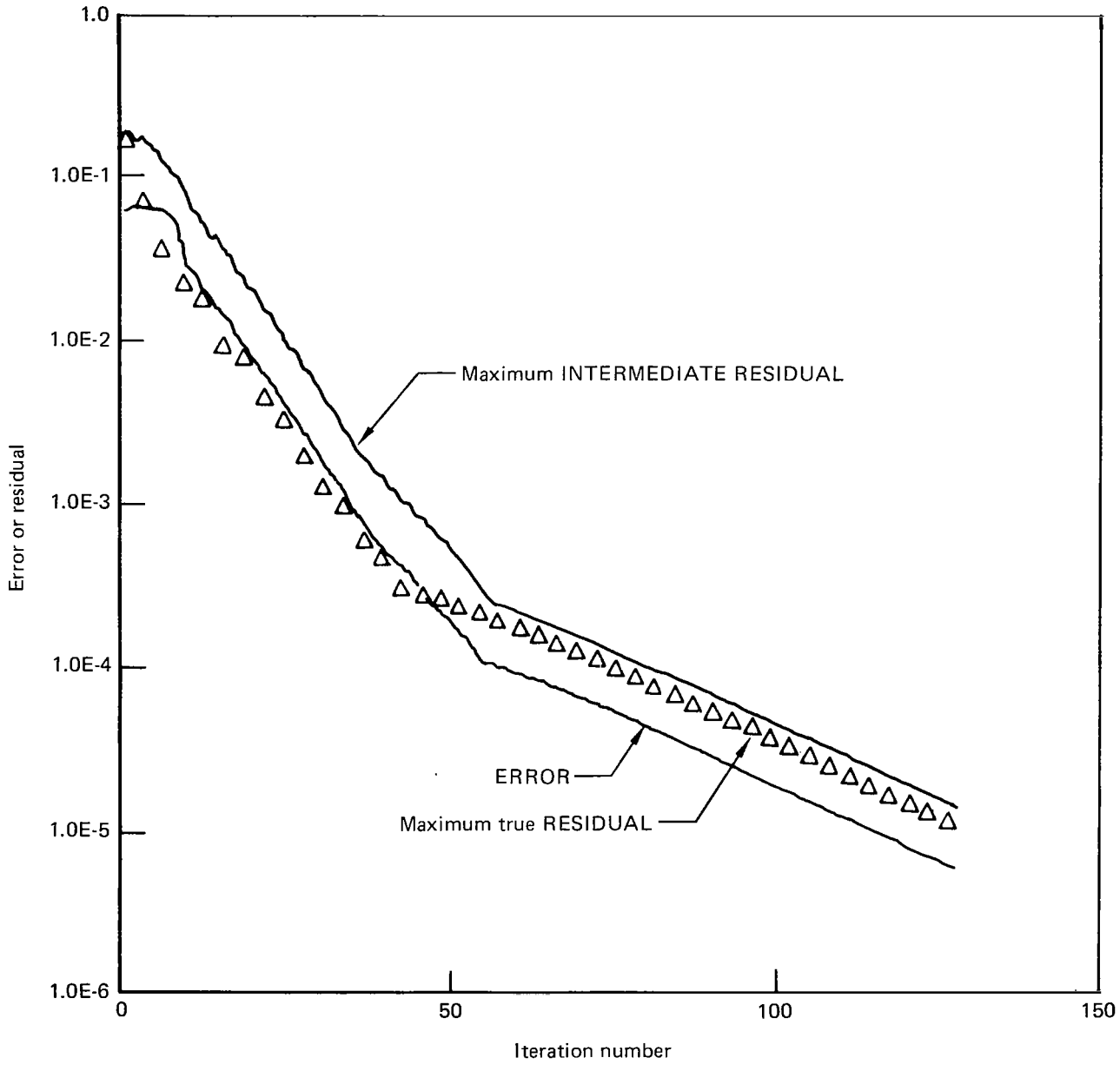

Figure D-2.—Sample ERROR and RESIDUAL Curves Versus Iteration for Row Relaxation, ORF = 1.7, M = 0.9, ω = 0.06, Flat Plate

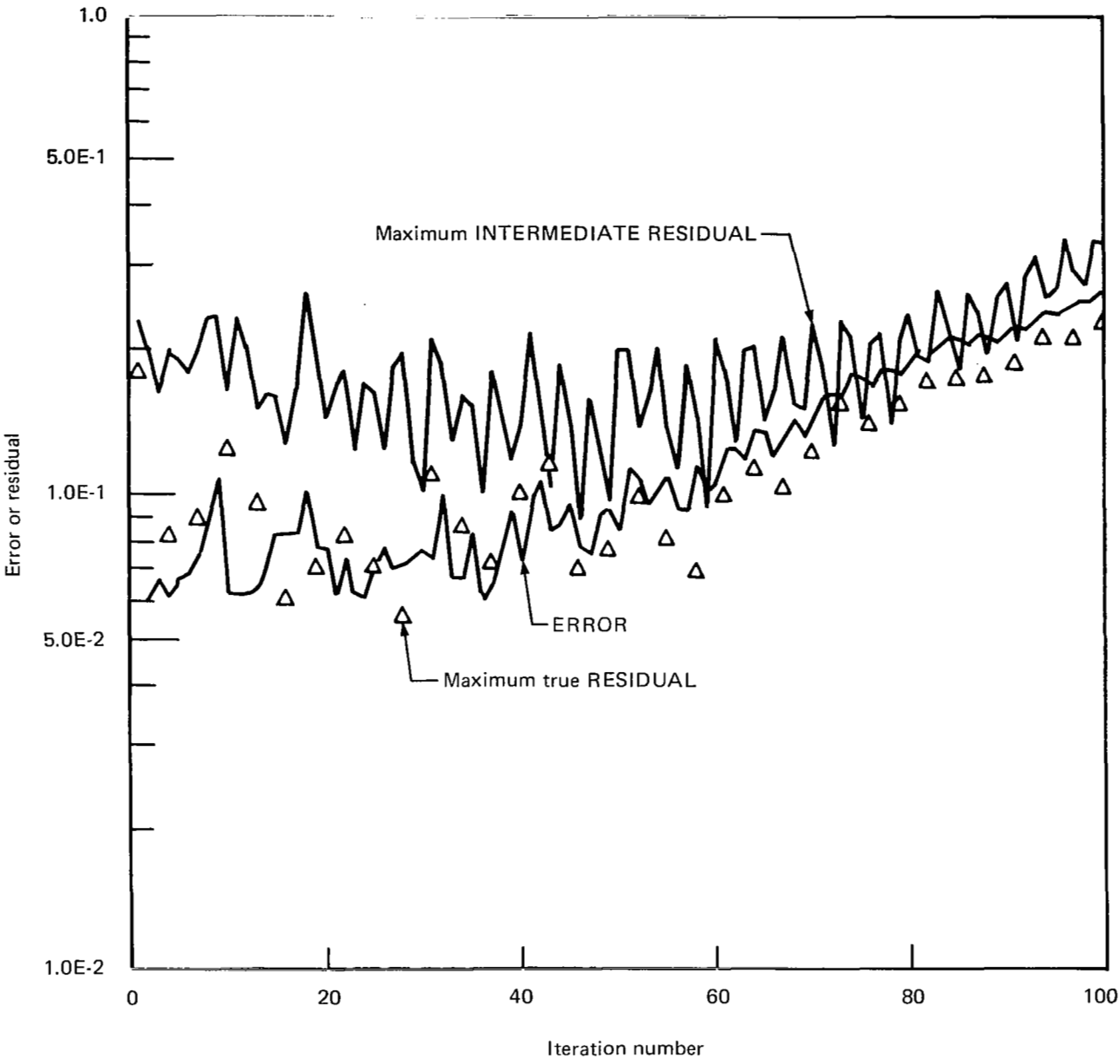

Figure D-3.—Sample ERROR and RESIDUAL Curves Versus Iteration for Row Relaxation, ORF = 1.85, M = 0.9, $\omega = 0.12$, Flat Plate

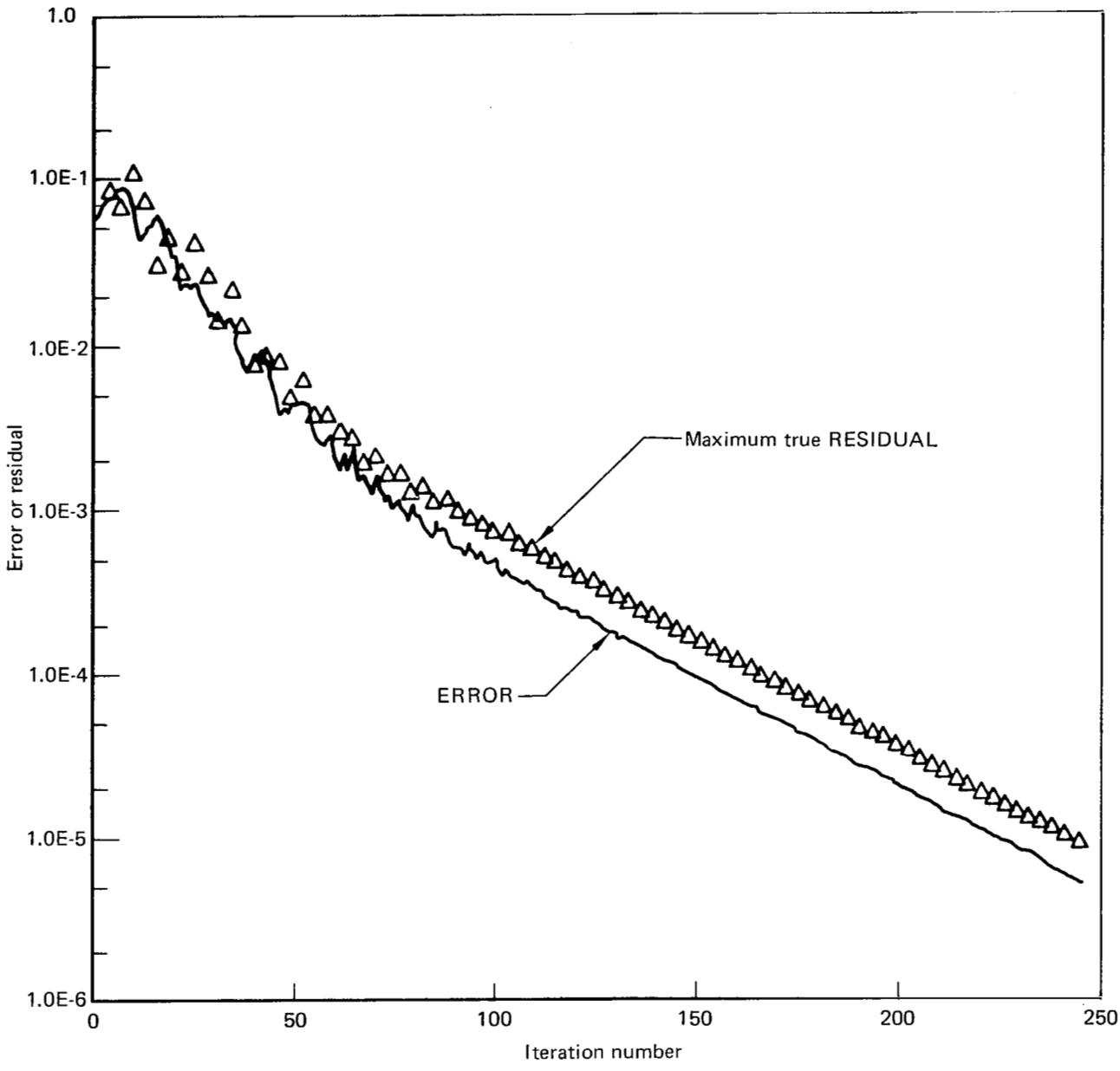

Figure D-4.—Sample ERROR and RESIDUAL Curves Versus Iteration for Row Relaxation, ORF = 1.85, M = 0.9, ω = 0.06, Circular-Arc Airfoil

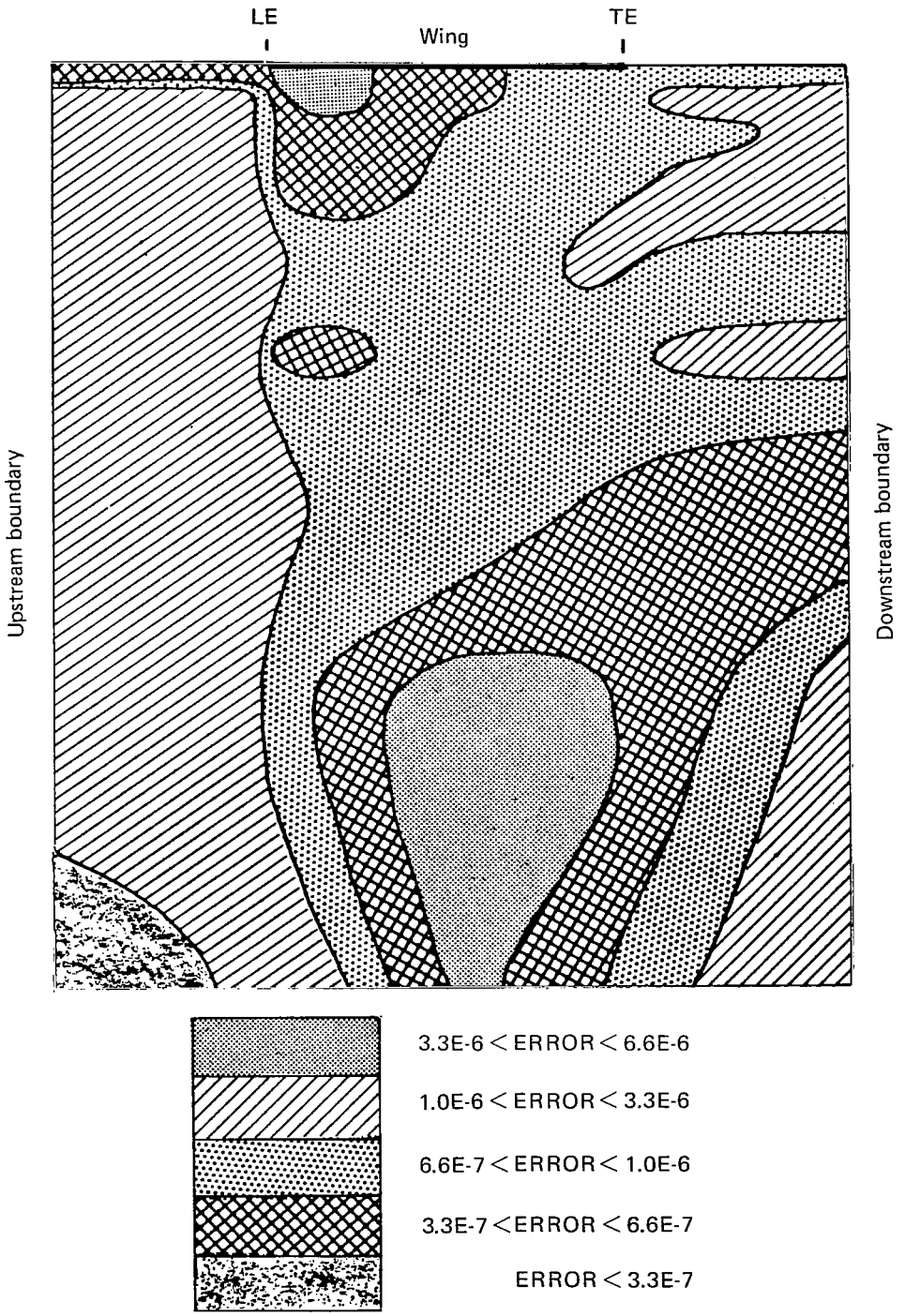

Figure D-5.—Areas of Matching ERROR Values for a Converged Solution, Row Relaxation, ORF = 1.85, M = 0.9, ω = 0.06

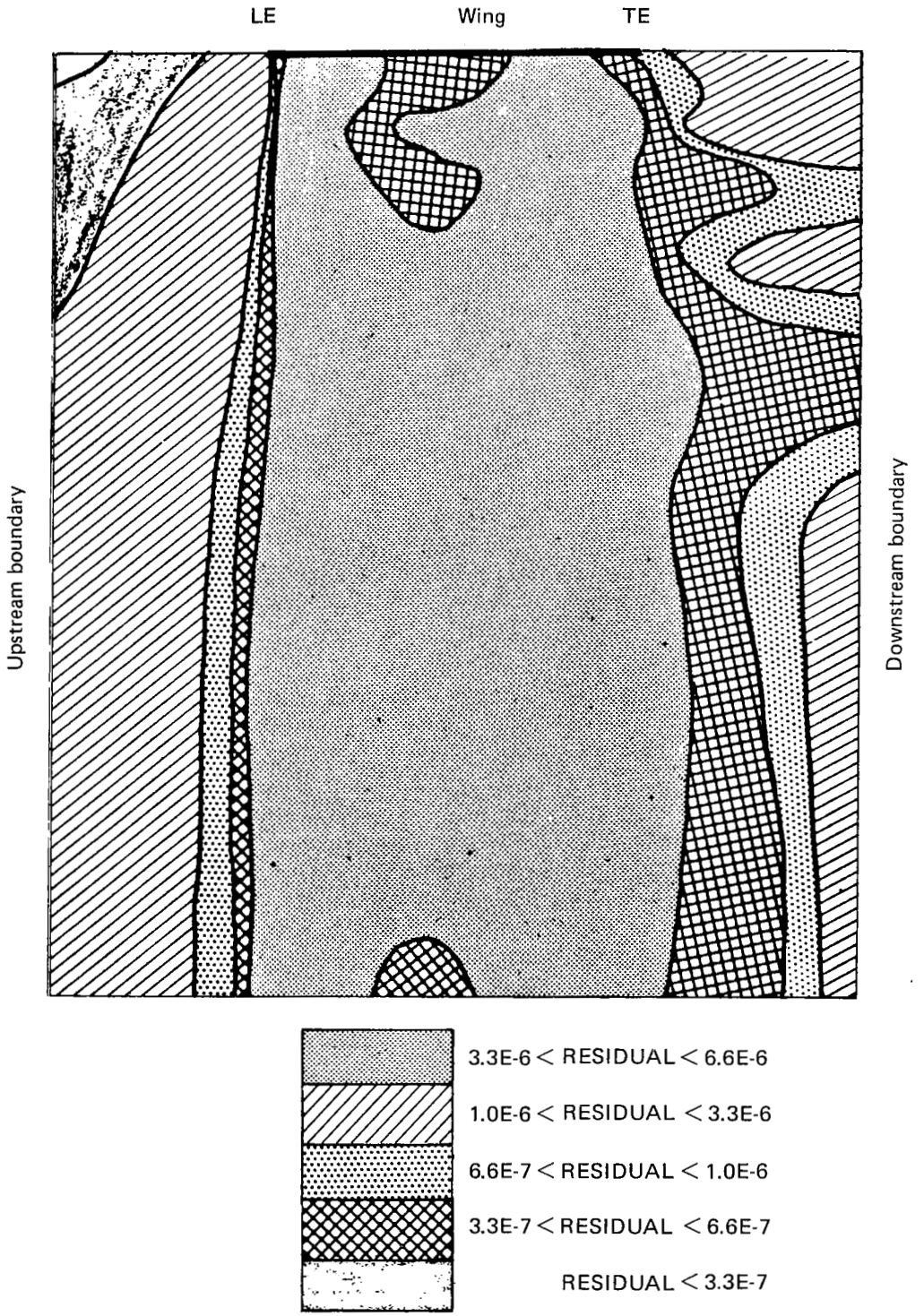

Figure D-6.—Areas of Matching RESIDUAL Values for a Converged Solution, Row Relaxation, ORF = 1.85, M = 0.9, $\omega = 0.06$

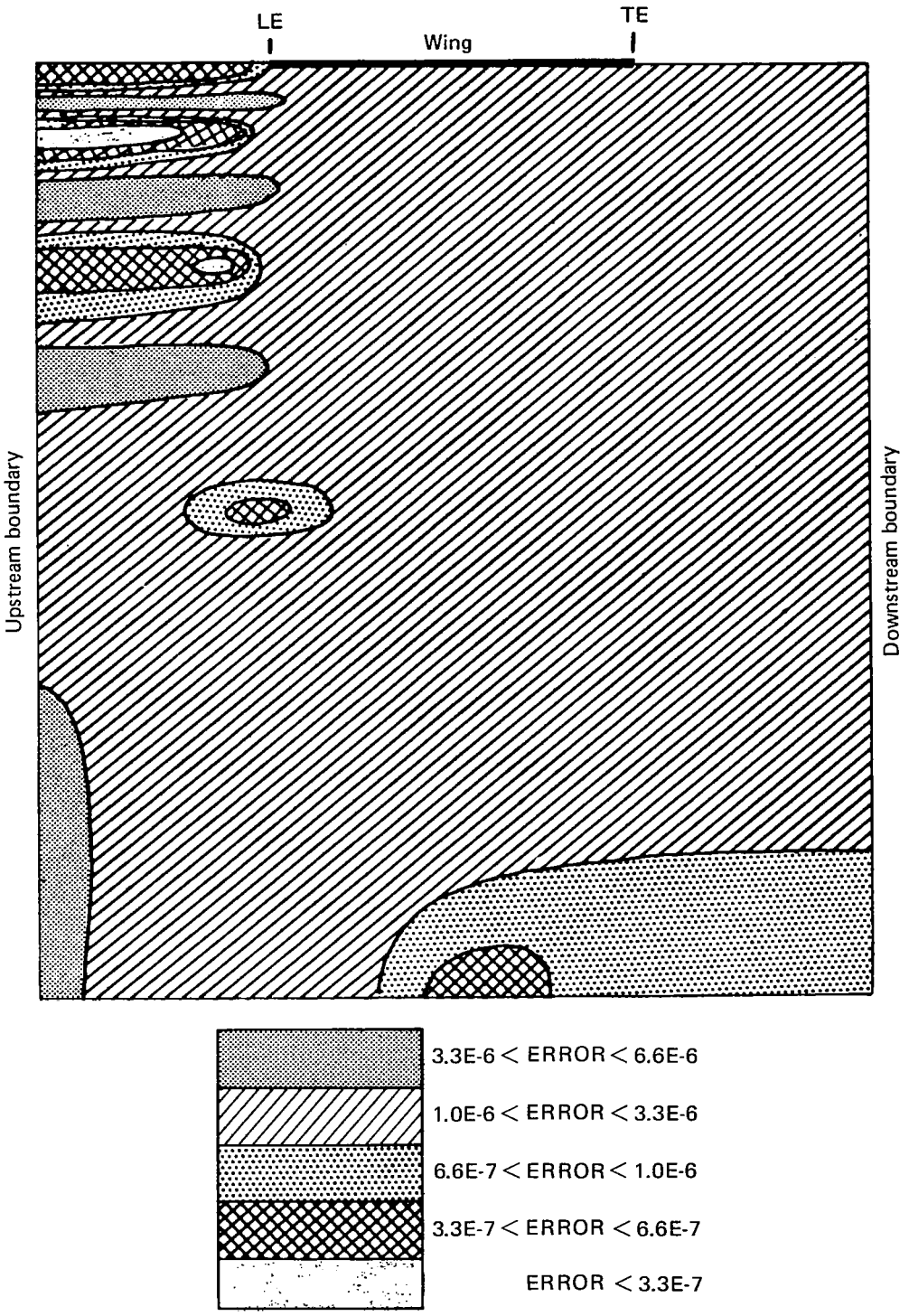

Figure D-7.—Areas of Matching ERROR Values for a Converged Solution Row Relaxation, ORF = 1.70, M = 0.9, ω = 0.06

results for the same solution but with ORF = 1.70. This time there is a distinct knee in the curves at about 50 iterations. After the knee in the curve, the true RESIDUAL lies between the INTERMEDIATE RESIDUAL and ERROR. For this particular case and with the level of convergence set at 10^{-5}, an ORF of 1.7 would be better than an ORF of 1.85. However, if the convergence criterion were set lower, then the ORF of 1.85 would be preferred.

For figure D-3 the problem has been changed by raising the frequency so that the solution diverges. Again all three curves move together but in a far from smooth manner. Both the ERROR and the INTERMEDIATE RESIDUAL provide a good indication of what is happening to the solution. Figure D-4 presents ERROR and the true RESIDUAL for a case with thickness, and again the two curves are essentially parallel to each other.

Figure D-5 shows the ERROR distribution for a converged (maximum error less than 10^{-5}) solution. The finite difference area below the wing is divided into levels of ERROR. For example, the most converged points in the field according to the ERROR criterion are in the uniformly shaded areas adjacent to the wing leading edge and near the lower boundary beneath the wing. Figure D-6 shows the same type of plot for the RESIDUAL. Here, the most converged portion of solution according to the RESIDUAL criterion lies nearly uniformly under the wing extending from wing surface to lower boundary. Figure D-7 shows the ERROR distribution for a different overrelaxation factor (1.7 rather than 1.85) with the distribution quite different from that of figure D-5.

REFERENCES

1. Ehlers, F. Edward: *A Finite Difference Method for the Solution of the Transonic Flow Around Harmonically Oscillating Wings.* NASA CR-2257, January 1974.

2. Murman, E.M.; and Cole, J.D.: "Calculation of Plane Steady Transonic Flows." *AIAA J.,* Vol. 24, 1971, pp 841-851.

3. Krupp, J.A.; and Murman, E.M.: "Computation of Transonic Flows Past Lifting Airfoils and Slender Bodies." *AIAA J.,* Vol. 10, No. 7 July 1972, pp 880-887.

4. Krupp, J.A.: *The Numerical Calculation of Plane Steady Transonic Flows Past Thin Lifting Airfoils.* Doctor of Philosophy Thesis, University of Washington, 1971; also Boeing Scientific Research Laboratories, document D180-12958-1, June 1971.

5. Weatherill, W.H.; Ehlers, F.E.; and Sebastian, J.D.: *Computation of the Transonic Perturbation Flow Fields Around Two- and Three-Dimensional Oscillating Wings.* NASA CR-2599, December 1975.

6. Weatherill, W.H.; Ehlers, F.E.; and Sebastian, J.D.: *On the Computations of the Transonic Perturbation Flow Field Around Two- and Three-Dimensional Oscillating Wings.* AIAA paper No. 76-99, January 1976.

7. Traci, R.M.; Albano, E.D.; Farr, J.L., Jr.; and Cheng, H.K.: *Small Distrubance Transonic Flows About Oscillating Airfoils.* AFFDL-TR-74-37, June 1974.

8. Traci, R.M.; Farr, J.L.; and Albano, E.: *Perturbation Method for Transonic Flows About Oscillating Airfoils.* AIAA paper 75-877, presented at the AIAA 8th Fluid and Plasma Dynamics Conference, Hartford, Connecticut, June 16-18, 1975.

9. Traci, R.M.; Albano, E.D.; and Farr, J.L., Jr.: *Small Disturbance Transonic Flows About Oscillating Airfoils and Planar Wings.* AFFDL-TR-75-100, August 1975.

10. Tijdeman, H.; and Schippers, P.: *Results of Pressure Measurements on an airfoil With Oscillating Flap in Two-Dimensional High Subsonic and Transonic Flow (Zero Incidence and Zero Mean Flap Positions).* NLR report TR 73078 U, July 1973.

11. Klunker, E.B.: *Contributions to Methods for Calculating the Flow About Thin Lifting Wings at Transonic Speeds.* NASA TN D-6530, November 1971.

12. South, J.C.; and Brandt, A.: "The Multigrid Method: Fast Relaxation for Transonic Flows." Paper presented at the 13th Annual Meeting, Society of Engineering Science, Hampton, Virginia, Nov. 1-3, 1976. *Advances in Engineering Science,* Vol. 4, pp 1359 - 1369, NASA CP-2001, 1976.

13. Hafez, M.M.; Rizk, M.H.; and Murman, E.M.: "Numerical Solution of the Unsteady Transonic Small-Disturbance Equations." Presented at the 44th Meeting of the AGARD Structures and Materials Panel, Lisbon, Portugal, April 17-22, 1977.

14. Carlson, Leland A.: *Transonic Airfoil Flowfield Analysis Using Cartesian Coordinates.* NASA CR-2577, August 1975.

15. Rowe, W.S.; Winther, B.A.; and Redman, M.C.: *Prediction of Unsteady Aerodynamic Loadings Caused by Trailing Edge Control Surface Motions in Subsonic Compressible Flow-Analysis and Results.* NASA CR-2003, March 1972.

16. Redman, M.C.; Rowe, W.S.; and Winther, B.A.: *Prediction of Unsteady Aerodynamic Loadings Caused by Trailing Edge Control Surface Motions in Subsonic Compressible Flow-Computer Program Description.*NASA CR-112015, March 1972.

17. Magnus, R.J.; and Yoshihara, H.: *Calculations of Transonic Flow Over an Oscillating Airfoil.* AIAA paper 75-98, January 1975.

18. Fischer, C.F.; and Usmani, R.A.: "Properties of Some Tridiagonal Matrices and Their Application to Boundary Value Problems". *SIAM Journal on Numerical Analysis,* Vol. 6, No. 1, March 1969.

19. Butler, T.D.; Weatherill, W.H.; Sebastian, J.D.; and Ehlers, F.E.: V174, "A Computer Program Using Finite Difference Methods for Analyzing Three-dimensional Transonic Flow Over Oscillating Wings", NASA CR-145214, 1977.

20. Ballhaus, W.F.; and Bailey, F.R.: *Numerical Calculation of Transonic Flow About Swept Wings.* AIAA paper No. 72-677, presented at the AIAA 5th Fluid and Plasma Dynamics Conference, Boston, Massachusetts, June 26-28, 1972.

21. Schmidt, W.; Rohlfs, R.; and Vanino, R.: *Some Results Using Relaxation Methods for Two-and Three-Dimensional Transonic Flows.* Presented at the Fourth International Conference on Numerical Methods in Fluid Dynamics, Boulder, Colorado, June 24-28, 1974.

22. Shanks, D: "Non-Linear Transformations of Divergent and Slowly Convergent Sequences." *Journal of Math. and Phys.,* vol. 34, 1955, pp 1-42.

23. Murman, E.M.: "Analysis of Embedded Shock Waves Calculated by Relaxation Methods," *AIAA Journal,* vol 12, no. 5, pp 626-633.